PhD Thesis

Charge and spin dynamics in low dimensional systems

Szabolcs Vajna

Supervisor: Dr. Balázs Dóra
Professor
Department of Physics
BME

Budapest University of Technology and Economics

2017

Contents

1 Introduction **7**
- 1.1 Equilibration of quantum systems . . . 9
- 1.2 Floquet theory . . . 12
- 1.3 Cold atom experiments . . . 14
- 1.4 Topological insulators . . . 15
  - 1.4.1 Topological numbers . . . 18
  - 1.4.2 Topological semimetals . . . 19

2 Dynamical phase transitions **21**
- 2.1 Theoretical background . . . 22
  - 2.1.1 The setup and the Loschmidt amplitude . . . 22
  - 2.1.2 Relation to the stationary state following the quench . . . 24
  - 2.1.3 Fisher zeros in thermal phase transitions . . . 24
  - 2.1.4 Fisher zeros in dynamical phase transitions . . . 26
  - 2.1.5 Simple example: a direct mapping to statistical physics . . . 27
  - 2.1.6 Relation between dynamical phase transitions and equilibrium phase transitions . . . 28
- 2.2 Quantum XY spin chain in magnetic field . . . 28
  - 2.2.1 Dynamical free energy . . . 30
  - 2.2.2 Fisher zeros . . . 31
  - 2.2.3 Examples . . . 32
  - 2.2.4 Longitudinal magnetization . . . 34
  - 2.2.5 Stationary states . . . 35
  - 2.2.6 Polarized initial states . . . 36
- 2.3 Dynamical phase transition and topology . . . 37
  - 2.3.1 One dimensional case . . . 39
  - 2.3.2 Two dimensions . . . 41
  - 2.3.3 Relation to entanglement dynamics . . . 42
  - 2.3.4 Example: Generalized SSH model . . . 42
  - 2.3.5 Example: The Haldane model . . . 44
  - 2.3.6 Effect of disorder . . . 46

2.4 Summary and outlook . . . 48

3 Schwinger pair creation in Weyl semimetals 49
3.1 Electric field switch-on in a Weyl semimetal . . . 50
3.1.1 Landau-Zener problem and the Kibble-Zurek mechanism . . . 51
3.1.2 Landau-Zener dynamics and the induced current . . . 53
3.2 Evolution of the current . . . 55
3.3 Steady state picture from Drude theory . . . 58
3.4 Statistics of pair creation . . . 59
3.5 Probability of no current and the vacuum persistence probability . . . 61
3.6 Finite temperature . . . 62
3.7 Conclusion . . . 63

4 Floquet topological phases coupled to environments 65
4.1 Quantum spin Hall edge states irradiated by circularly polarized light . . . 67
4.1.1 Chiral edge current in the average energy concept . . . 69
4.1.2 Coupling the system to a heat bath . . . 70
4.2 The non-secular Lindblad equation . . . 71
4.3 Applying the Lindblad equation to the edge state . . . 73
4.3.1 Steady states in the secular Lindblad equation . . . 74
4.3.2 Beyond the secular approximation . . . 76
4.3.3 Dominant frequency approximation (DFA) . . . 78
4.4 Photocurrent along the edge . . . 82
4.5 Conclusion . . . 85

5 Conclusion and thesis statements 87

6 Acknowledgements 91

A Appendix 93
A.1 Jordan-Wigner transformation . . . 93
A.2 Non-Markovian equation . . . 94
A.3 Expectation values in the rotated interaction picture . . . 94
A.4 Matrix elements (dominant frequency approximation) . . . 96

B Bibliography 99

List of Abbreviations

Abbreviation	Explanation
AC	Alternating current
BCS	Bardeen-Cooper-Schrieffer
BHZ	Bernevig-Hughes-Zhang
BZ	Brillouin zone
CGF	Cumulant generating function
CLT	Central limit theorem
DC	Direct current
DFA	Dominant frequency approximation
DPT	Dynamical phase transition
EPT	Equilibrium phase transition
ETH	Eigenstate thermalization hypothesis
GETH	Generalized eigenstate thermalization hypothesis
GGE	Generalized Gibbs ensemble
LA	Loschmidt amplitude
LZ	Landau-Zener
KZ	Kibble-Zurek
MBL	Many-body localization
PHS	Particle-hole symmetry
QHE	Quantum Hall effect
QSH	Quantum spin Hall
SSH	Su-Schrieffer-Heeger
TI	Topological insulator
TRS	Time reversal symmetry
WSM	Weyl semimetal

1 Introduction

Conventional statistical physics and thermodynamics are extremely successful in describing macroscopic systems near equilibrium conditions. A good understanding of the equilibrium properties also gives insight to the dynamical response of these systems, as, for instance, the fluctuation-dissipation theorem relates the equilibrium fluctuations to the response for small perturbations. These linear response functions, transport coefficients, Onsager relations, etc. form the main subject of the *traditional non-equilibrium statistical mechanics*, which, in contrast to its name, describes near-equilibrium physics. In many electronic devices, studying linear response gives satisfactory results, and the properties of highly excited states are usually irrelevant. Counterexamples are laser devices, which are inherently far from equilibrium, nevertheless they are widely used in academy, in the industry and also in the everyday life.

In the recent decades remarkable attention has focused on studying systems which are far away from equilibrium [1, 2], and are beyond the validity of traditional non-equilibrium statistical mechanics and linear response theory. The academic interest in out-of-equilibrium physics has a long history, it goes back to the birth of quantum mechanics, by studying how the equilibrium states can be approached from microscopic dynamics [3]. The renaissance of the topic was initiated by the experimental advances achieved with ultracold atomic gases, which made possible to prepare and detect non-equilibrium states with previously unexpected controllability and stability [4, 5]. These experiments have also triggered huge progress in theoretical physics. A brief introduction to ultracold atoms is given in section 1.3.

The out-of-equilibrium world is still largely unexplored and is presumably full of surprises and treasures. A comprehensive understanding similar to statistical mechanics of equilibrium systems is still lacking, but some unifying concepts have been developed, for example non-equilibrium fluctuation theorems [6–8]. There are several perspectives of out-of-equilibrium physics. One is to look for non-equilibrium analogies or generalization of equilibrium notions, such as adiabatic theorem, phase transitions, etc. A second one is engineering some properties of matter to obtain desired behaviour by bringing them out of equilibrium. A third direction is to find completely new phenomena, which do not have any equilibrium counterparts. The main goal of the field is to find universal features of the dynamics from the analysis of specific systems.

Non-equilibrium systems can be classified based on the way they are pushed away from equilibrium. These are called non-equilibrium protocols or driving. The most widely

analyzed protocol is the (sudden) quench, when the system is brought out of equilibrium by a sudden change in the coupling parameters, e.g. in the magnitude or direction of some external fields, or in the interaction strength among particles. Another popular protocol is called ramp, when the parameters describing the Hamiltonian are changed gradually, usually as a linear function (linear ramps), or as a smooth function to suppress excitations. Finally, periodic driving and the corresponding Floquet theory constitutes a separate branch of out-of-equilibrium physics. A cartoon of the protocols are illustrated on Figure 1.1.

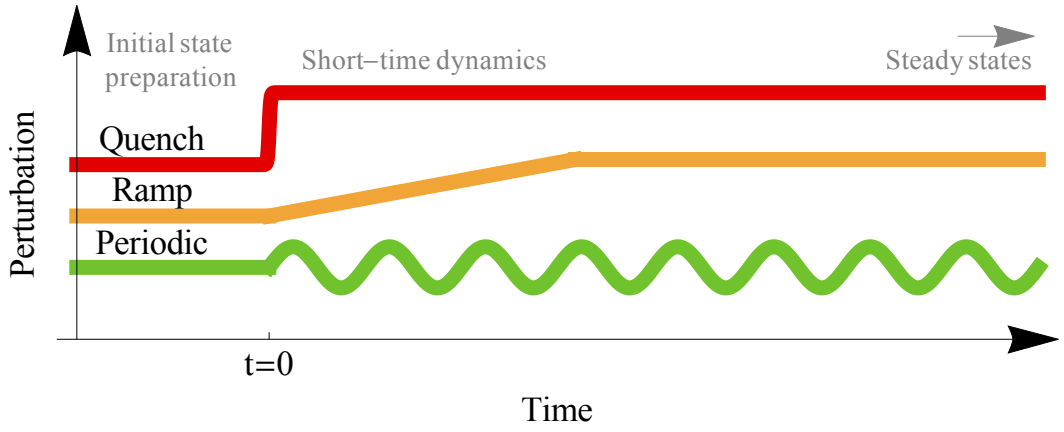

Figure 1.1: Illustration of the most popular non-equilibrium protocols, which are also studied in this thesis.

The wide range of timescales involved in the dynamics contributes to the complexity of non-equilibrium physics. Some important questions in the short time dynamics are how defects are generated under the driving, and how they relax after the driving is turned off. Either with or without external driving, we expect that the systems after a long time evolution reach some steady or stationary states. The description of these states, whether they are thermal [9] or can be described by a more complicated Gibbs ensemble [10], are also fundamental questions of out-of-equilibrium physics.

A promising application of non-equilibrium physics is quantum computation. Though large scale quantum computers have not been realized yet, understanding coherent dynamics and state manipulation by various protocols will presumably be crucial for future applications in quantum information processing and quantum technology [11]. A promising branch of quantum computation, applied for example in the controversial first commercial device which was claimed to be a quantum computer [12], is based on the quantum adiabatic theorem. The main idea of adiabtic quantum computation is to adiabatically evolve the ground state of a Hamiltonian which is easy to prepare, to the ground state of another Hamiltonian which encodes the solution of an optimization problem [13]. However, practical applications require fast computation, which necessarily creates excitations, studied usually in the context of out-of-equilibrium physics. A related goal of the field is to find optimal driving protocols [14–16], or shortcuts to adiabaticity [17], which minimize excitations above a target state we intend to prepare, while keeping the protocol fast.

Non-equilibrium behaviour has been studied in various systems, starting from classical fluids, biological and eco-systems through to condensed matter. In this thesis, I study

simple fermionic and spin models of condensed matter systems to analyze their out-of-equilibrium behaviour from various aspects. Chapter 1 provides a general introduction to various topics, which serve as either a motivation or a background to the studies included in the thesis. In section 1.1 we review the recent theoretical progress achieved in thermalization of closed quantum systems, which is one of the most important questions of non-equilibrium physics. Next, in section 1.2, we introduce periodically driven systems from the point of view of Floquet engineering, which is a method to design Hamiltonians with tunable parameters. Then we give a short introduction to cold atom experiments in section 1.3, which are uniquely suitable to study out-of-equilibrium physics. Finally, in section 1.4 we introduce topological insulators and topological semimetals, which, under non-equilibrium circumstances, are the main subjects of investigation in the following chapters. In addition, because of the large variety of questions, protocols and systems appearing in the thesis, all chapters start with an introduction.

The thesis is organized as follows. In chapter 2, we study the properties of dynamical phase transitions, which are characterized by non-analyticities appearing in the time evolution following a *sudden quench* protocol. In particular, we investigate the relation between the occurrence of dynamical phase transitions and equilibrium quantum phase transitions for various models [18, 19], such as spin chains, topological insulators and superconductors. In chapter 3, we present our analysis about Schwinger's mechanism in topological semimetals [20], which describes the creation of electron-hole pairs following a sudden quench in the electric field, or equivalently, under a *linear ramp* in the vector-potential. We determine the full statistics of charge carriers generated by the perturbation and we discuss the time evolution of the electric current as well. In chapter 4, we analyze the occupation of the Floquet quasienergy bands in a quantum spin Hall insulator irradiated by circularly polarized light, which acts as a *periodic perturbation*, and we study the induced photocurrent in the presence of dissipation [21]. Finally, chapter 5 is devoted to summarizing the content of the thesis.

1.1 Equilibration of quantum systems

One of the key questions in non-equilibrium physics is how quantum systems reach thermal equilibrium, when they encounter a change in the environment, e.g. when an external magnetic or electric field is suddenly switched on or off. In classical physics even closed systems can thermalize under their intrinsic dynamics [22]. In chaotic systems the trajectories in phase space are exponentially sensitive to small perturbations, a tiny ambiguity in the initial conditions leads to a totally different time evolution. Moreover, almost all trajectories explore the entire phase space restricted only by the conservation of energy, which behaviour is called ergodicity, and long time averages of observables become independent of the initial conditions. These time averages can be calculated as statistical (phase-space or microcanonical) averages, which form the basics of statistical mechanics.

The picture is slightly different in quantum systems. The concept of exponentially diverging trajectories and the exploration of the phase space cannot be directly translated to the Hilbert space, because the unitary time evolution does not change the distance between states: $\langle\psi_1(t)|\psi_2(t)\rangle = \langle\psi_1(0)|\psi_2(0)\rangle$. The Schrödinger equation never transforms a pure state into a mixed state, which would be necessary for a statistical description, so equilibration cannot occur in the level of wavefunctions. However, in most of the cases,

expectation values of observables tend to approach stationary values after long time evolution. The principle behind this phenomena is dephasing. A simple illustration is a non-equilibrium initial state with well defined order, which is not supported by the Hamiltonian governing the time evolution, e.g. a density wave in a translation-invariant environment. This structure appears as a coherent superposition of the eigenstates from a wide energy interval, which collapses quickly as the individual eigenstates obtain different phases under time evolution, and in infinite systems revivals might never occur. Dephasing has similar effect to averaging: if the time evolution supports stationary expectation values, then the infinite time limit coincides with the time average:

$$\lim_{t\to\infty} \langle \mathcal{O}(t) \rangle = \lim_{T\to\infty} \frac{1}{T} \int_0^T \langle \mathcal{O}(t) \rangle \, \mathrm{d}t \equiv \overline{\langle \mathcal{O}(t) \rangle} \tag{1.1}$$

Calculating time averaged expectation values is formally simple in the eigenbasis of the Hamiltonian. If the initial state is expanded as $\psi_0 = \sum_n c_n |n\rangle$, then

$$\langle \mathcal{O}(t) \rangle = \mathrm{Tr}\{\rho(t)\mathcal{O}\} = \sum_{n,m} c_m^* c_n e^{-i(E_n - E_m)t} \langle m|\mathcal{O}|n\rangle \ , \tag{1.2}$$

and assuming no degeneracies in the spectrum

$$\overline{\langle \mathcal{O}(t) \rangle} = \mathrm{Tr}\{\rho_{DE}\mathcal{O}\} = \sum_{n,m} |c_n|^2 \langle n|\mathcal{O}|n\rangle \ . \tag{1.3}$$

The diagonal part of the density matrix ρ_{DE} is called *diagonal ensemble*, because assuming no degeneracies in the spectrum, it gives the stationary expectation values of observables from a statistical description. ρ_{DE} describes a mixed state, which contains less information than the pure $\rho(t)$, but it still requires an exponential number of parameters in system size. It arises as a further question whether the stationary states could be described by a much simpler Gibbs ensemble, e.g. with only a single parameter, the effective temperature,

$$\lim_{t\to\infty} \rho(t) \overset{?}{\sim} \rho_{Gibbs} \tag{1.4}$$

which we would call thermalization. The answer is positive for generic interacting quantum systems: they act as a heat bath for their own subsystems, and *local expectation values* are well captured by a Gibbs ensemble, with temperature set by the energy of the initial state, that is

$$\lim_{t\to\infty} \langle \mathcal{O}(t) \rangle = \mathrm{Tr}\{e^{-\beta H}\mathcal{O}\} \tag{1.5}$$

for any local $\mathcal{O}$, where β is the inverse temperature.

This result is motivated by the eigenstate thermalization hypothesis [9, 23, 24] (ETH), which can be thought of as the quantum counterpart of classical ergodicity. It does not study trajectories in the Hilbert space, instead, it states that ergodicity is encrypted in the eigenstates of the Hamiltonian. The eigenstate thermalization hypothesis assumes that the eigenstates of ergodic Hamiltonians are thermal in the sense that different eigenstates from a small energy interval look identical from the point of view of local observables,

and they provide the same expectation values. In other words, the expectation values in any eigenstates are approximately equal to the microcanonical average:

$$\langle\psi_n|\mathcal{O}|\psi_n\rangle \approx \mathrm{Tr}\{\rho_{MC}(E_n)\mathcal{O}\}\,, \tag{1.6}$$

where $\rho_{MC}(E_n)$ is the microcanonical density matrix at energy E_n. This hypothesis has not been proved, but it has been demonstrated numerically to hold for various systems. In the thermodynamic limit from the equivalence of ensembles, we get equally good description with a canonical ensemble, with a temperature fixed by the initial energy. The theory of ETH has many further implications e.g. constraints for off-diagonal matrix elements, and fluctuations of observables, etc. The observation that ergodicity is hidden in the eigenstate properties of the *Hamiltonian*, gives a hint where to look for chaos in quantum systems. Though tiny difference in initial states remain tiny under time evolution, states may show large difference if, instead, the perturbation acts on the Hamiltonian. Indeed, the Loschmidt echo [25],

$$L(t) = |\left\langle\psi_0|e^{i(H+\delta H)t}e^{-iHt}|\psi_0\right\rangle|^2 \tag{1.7}$$

measuring the overlap of wavefunctions undergoing two slightly different time evolution, displays exponential sensitivity of perturbations of the Hamiltonian, and is used to characterize quantum chaos [26, 27]. Although from a different perspective, the Loschmidt echo, or its variant, the Loschmidt amplitude will be a central object of chapter 2.

There are two branches of counterexamples, which do not satisfy ETH: integrable and many-body localized (MBL) systems. Integrable systems are characterized by an infinite number of mutually commuting local integrals of motion, which are conserved under time evolution, displaying memory of the initial conditions. The canonical Gibbs distribution is the most random distribution, i.e the one maximizing the entropy, which respects energy conservation. This latter appears as a Lagrange multiplier in the density matrix: $\rho_{Gibbs} \sim e^{-\beta H}$. A naive generalization of this method to infinite conserved quantities $\{Q_i\}_{i=1}^{\infty}$ leads to the generalized Gibbs ensemble [10] (GGE), where $\rho_{GGE} \sim e^{-\lambda_i Q_i}$ and the Lagrange multipliers λ_i are determined from the initial expectation values of the charges Q_i. GGE can be further motivated by the generalized eigenstate thermalization hypothesis [28] (GETH), which states that eigenstates with the same set of conserved quantities are locally indistinguishable. GGE was proved for free fermion systems, and the validity of GGE in interacting integrable models was the subject of many recent studies [29–32].

Many-body localization [33] is a localization transition of interacting systems, a generalization of the Anderson localization. Below a critical disorder strength, these interacting systems are in a thermalizing (ergodic) phase, that is, the whole system acts as heat bath for the subsystems, and even closed systems can effectively thermalize by their own dynamics. By increasing the disorder one arrives to the many-body localized phases exhibiting nonergodic behavior. They fail to thermalize, and the memory of initial conditions persist for infinite times. In contrast to usual quantum phase transitions, MBL is not a low-energy transition, but it describes changes of the high-energy eigenstates of the Hamiltonian. Hence sometimes it is referred to as an infinite temperature phase transition. It is also characterized by robust integrability, as conservation laws emerge from the disorder, without any need of fine-tuning the parameters. Heat and charge transport are completely suppressed in MBL systems.

We have briefly summarized the mechanism of equilibration in closed quantum systems in constant environment. The same questions can be asked when changing environments as well, for example, in periodically driven systems. In this case we also expect that, following a transient dynamics, the observables at late times become invariant under time translations, that are multiples of the driving period. We may refer to this as a steady state in driven systems. This phenomena was found in free fermionic systems, where the long time expectation values are described by a Periodic Gibbs Ensemble [34], which, similar to the GGE, is constructed from an extensive number of conservation laws. In contrast, several studies have indicated that globally driven *interacting systems* do not support any conservation laws, and they thermalize to a structureless, infinite-temperature stationary state [35–37].

Understanding thermalization of closed systems is not only fundamental from the theoretical point of view, but it is also the relevant scenario in cold atom experiments, because cold atom systems are very well isolated from the environment. On the other hand, perfect isolation is never achievable, especially in condensed matter physics, which then requires the analysis of open quantum systems. The dynamics of open systems largely depend on the way they are coupled to the environment, and on the properties of the environment as well. However, if the coupling between the system and the environment is small, statistical mechanics is expected to work, leading to undriven systems approaching the Gibbs distribution with the temperature given by the environment. The question is much more intricate in driven systems, where an interesting competition arises between the energy absorbed from the drive and the heat passed to the environment. In chapter 4, we study the stationary state of a simple periodically driven system, and we find that equilibration to time-periodic stationary states occur, but the occupation of these states is generally not thermal.

1.2 Floquet theory

In this section we briefly introduce the Floquet theory of periodically driven systems, which stands behind numerous cold atom experiments and it also serves as the background for chapter 4. The Hamiltonian of periodically driven systems is invariant under discrete time translations that are multiples of the period: $H(t+T) = H(t)$. The Floquet theory exploits this discrete time translational symmetry to classify the time evolution, similarly to the Bloch theorem, which classifies the eigenstates of the Hamiltonians with discrete spatial translational symmetry. The solutions of the time-dependent Schrödinger equation can be written in the following form [38, 39]:

$$i\hbar\partial_t \Psi_n(t) = H(t)\Psi_n(t) \tag{1.8}$$

$$\Psi_n(t) = e^{-i\epsilon_n t}\Phi_n(t) \tag{1.9}$$

where $\Phi_n(t) = \Phi_n(t+T)$ is time-periodic, and the phase factor ϵ_n is the quasienergy, which plays similar role to the energy in static systems. Because of the violation of continuous time-translation symmetry, the quasienergy is defined only modulo $\omega = \frac{2\pi}{T}$. Similarly to the wavenumbers lying outside the Brillouin-zone, all quasienergy values can be folded into the $[0, \omega)$ interval.

One can also define a *Floquet Hamilton operator* as the generator of discrete time translations, whose eigenvalues are the quasi-energies. From the operator point of view, the

Floquet theorem states, that the time evolution operator $U(t_1, t_0) = \mathcal{T} \exp\{-i \int_{t_0}^{t_1} H(t)\mathrm{d}t\}$ can be written in the following form [40]:

$$U(t_1, t_0) = P(t_1) e^{-i\tilde{H}_F(t_1 - t_0)} P(t_0)\,, \tag{1.10}$$

where $P(t) = P(t+T)$ is the time-periodic unitary micro-motion operator, which describes motion within a single period, and $\tilde{H}_F$ is the time-independent Floquet Hamiltonian. We can think of the P operator as a transformation to an abstract moving frame, in which the Hamiltonian looks static. That is, combining the differential equation evolving U, $i\partial_t U(t, t_0) = H(t)U(t, t_0)$, with Eq. (1.10), we get

$$\tilde{H}_F = P^+(t)H(t)P(t) - iP^+(t)\partial_t P(t)\,. \tag{1.11}$$

In many applications one is not interested in the complete time evolution, but only in stroboscopic times $t_0 + nT$. In this case the micro-motion (i.e. the motion within a single period) can be incorporated in the stroboscopic Floquet Hamiltonian H_F,

$$U(t_0 + nT, t_0) = e^{-iH_F nT}\,, \tag{1.12}$$

where $H_F = P(t_0)\tilde{H}_F P^+(t_0)$ depends explicitly on t_0, but its spectrum and the quasi-energies do not. That is, the stroboscopic time evolutions with different choices of the initial time t_0, which correspond to different initial phases of the drive, are unitary equivalent.

In general, determining the Floquet Hamiltionian is a very difficult problem, analytical solutions are only available for some very simple systems. If the driving frequency is so large that the system cannot follow the external perturbation, the system sees only the time average of the perturbation. From this consideration, an expansion perturbative in the inverse frequency can be constructed, $H_F = \sum_r H_{F,r}$, where $H_{F,r}$ is in the order of ω^r. The most widespread expansion was developed by Magnus [41, 42], for which the leading order terms are expressed as

$$H_{F,0} = \frac{1}{T}\int_0^T \mathrm{d}t H(t) \tag{1.13}$$

$$H_{F,1} = \frac{1}{2iT}\int_0^T \mathrm{d}t_2 \int_0^{t_2} \mathrm{d}t_2 [H(t_2), H(t_1)]\mathrm{d}t\,. \tag{1.14}$$

The main perspective of the Floquet theorem is that periodical driving protocols applied to a static system lead to an effective time-independent Hamiltonian time evolution at stroboscopic times, and the properties of this Floquet Hamiltonian are easily tunable by the driving protocol, for illustration see Figure 1.2. This idea is exploited in cold atom experiments, where periodic driving has been used to generate artificial magnetic fields [43–45] for nonmagnetic atoms, and to achieve topological phases [46]. Floquet physics was used for example to realize the topological Haldane model (see sections 1.4 and 2.3.5 for details) not only in cold atoms [46], but in photonic waveguides [47] as well. In the latter experiment, the role of the time is replaced by the distance in the propagation direction of the light, and the effect of periodic driving is simulated by the usage of helical waveguides instead of the usual cylindrical shape. The application of periodic driving is not limited to the previously mentioned artificial matter, there are numerous proposals to change the topological properties of condensed matter systems by irradiating them with electromagnetic fields [48, 49].

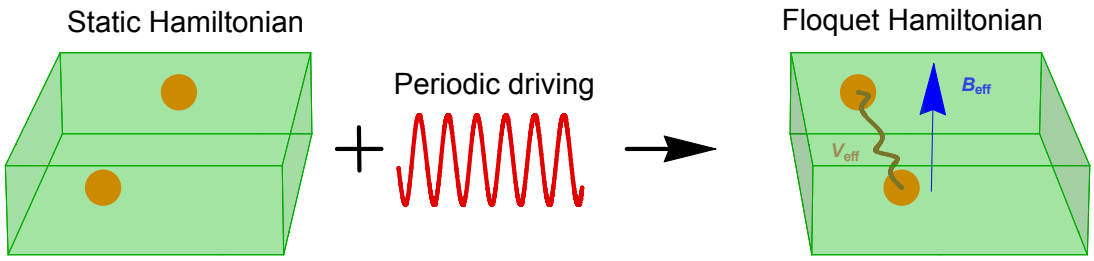

Figure 1.2: The main idea of the Floquet engineering is that a high frequency periodic driving can be used to change the properties of the initial system. For example artificial gauge fields or new interactions among the particles can be induced this way.

1.3 Cold atom experiments

Although cold atoms are not in the main focus of this thesis, they provide a unique platform to measure out-of-equilibrium dynamics. Furthermore, as we have discussed in the previous section, many of these experiments extensively use Floquet physics to achieve the desired Hamiltonian, which is another connection to the non-equlibrium dynamics. Throughout the thesis we often refer to cold atom experiments, here we give a rather brief introduction to the field.

State-of-the-art technology allows experimentalists to study the dynamics of neutral atoms loaded into optical lattices (Figure 1.3), simulating quantum many-body physics of condensed matter on highly enlarged time and length-scales. The optical lattices are based on the conservative dipolar interaction between the electric field and the atoms. The electric field of non-resonant light polarizes the atoms, which hence feel the electric field as a potential proportional to the field intensity. The sign of the potential shift depends on the detuning [50], which is the difference between the frequency of the laser and the nearest atomic transitions. The atoms are hence either trapped in regions of high or low intensity. There is another interaction between the electric field and the atoms, that is, the dissipative absorption and emission of photons, which, however, becomes suppressed for non-resonant frequencies. This latter effect is applied in laser-cooling settings, but is avoided in the construction of optical lattices. Optical lattices are formed by producing standing waves from counter-propagating laser beams, which act as periodic potential for neutral atoms with the lattice constant being proportional to the wavelength of the laser. Both the dimensionality and the geometry of the lattice are easily tunable by choosing a proper number of laser beams and by changing their relative angles and intensities. The atoms can tunnel between neighboring potential minima, with a rate exponentially suppressed by the potential barrier between the lattice sites, similarly to the electrons hopping in a crystal. Because of their convenient properties, alkali atoms are used in the majority of cold atom experiments. Depending on the number of neutrons in the atoms, they follow either fermionic (e.g. ^{6}Li, ^{40}K) or bosonic (e.g. ^{87}Rb) statistics. To probe the same physics as in condensed matter, these systems are cooled down to the order of nanokelvins.

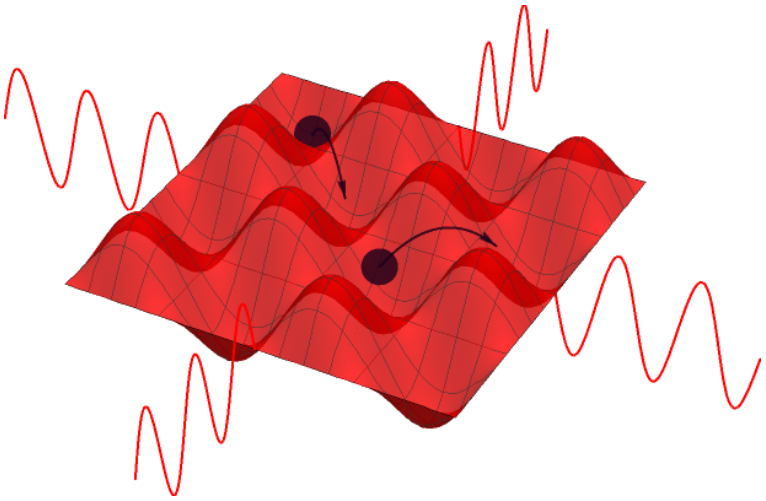

Figure 1.3: Optical lattices are created by counter-propagating laser beams, which act as a harmonic potential for the ultracold neutral atoms loaded into the lattice. These atoms can hop between the potential minima, similarly to the electrons in a metal.

In addition to the capability of these experiments to simulate Hamiltonian dynamics with highly tunable Hamiltonians, they allow for preparation of various initial states with high fidelity. The set of easily measurable parameters in cold atom systems are different from those in condensed matter. For instance, measuring conductivity is one of the simplest probes in experimental solid state physics, but is it rather difficult to measure it directly in cold atoms. On the other hand, the momentum distribution of the particles, which could only be inferred in condensed matter systems e.g. from ARPES measurements, is easily accessible in cold atoms by time-of-flight techniques, which detect the free evolution of the particles after the optical lattice is turned off. The limits of the experimental techniques can be pushed incredibly far, a fascinating example is the quantum gas microscope, which allows for the detection of even single atoms in optical lattices [51, 52].

1.4 Topological insulators

Traditionally, solid materials had been classified as being metals or insulators based on the band theory. Materials with partially filled bands are good conductors, because there are plenty of charge carriers available to conduct heat or electricity near the Fermi energy. Band insulators on the other hand are characterized by completely filled bands, with exponentially suppressed number of charge carriers, which implies the insulating behaviour. Semiconductors are considered as insulators with a small band gap in this classification. Topological insulators (TIs) consist of a new, previously unnoticed class in the band theory [53]. They are insulating in their bulk, but they exhibit robust conducting states on their surfaces or edges, which lie in the band gap of the bulk system. Although normal band insulators can also support surface or edge states, they are easily destroyed by changing the surface geometry or by disorder. In contrast, the surface states of topological insulators are *protected* by a global property, the *topology* of system, which cannot be altered by local perturbation, as long as the bulk band gap stays open. Similar to mag-

nets, which cannot be cut into a positive and a negative pole, the surface states cannot be removed by cutting off the surface layer of a topological insulator, as they reappear at the new surface. Historically the first example of topologically protected edge states was found in 1980-82 in the form of the quantum Hall effect (QHE) [54, 55], but the concept of topological insulators was only developed a quarter of century later. Besides the robustness of the surface states, topological insulators have other remarkable properties, which initiated the extraordinary attention to this field. First of all, these boundary states conduct very well, because of the suppression of backscattering. In the quantum Hall effect, it is a consequence of the chiral character of the edge states: current can only flow in one direction along the edge, counterpropagating states to scatter in are completely absent. In 1988, Haldane proposed a model for the quantum Hall Effect with a staggered magnetic field, but with zero total flux [56], which serves as the simplest example of the quantum Hall insulators. We introduce the Haldane model in section 2.3.5, where we use this example for illustrating our results on the dynamics of generic topological insulators.

Another type of TIs is the quantum spin Hall insulator (QSH insulator, proposed by Kane and Mele in 2005 [57]), which exhibits similar behavior to the QHE without breaking the time reversal symmetry. In this case the intrinsic spin-orbit coupling substitutes the role of the magnetic field, and for simplicity we can imagine this effect as two spin-dependent copies of the QHE, with spin up fermions moving clockwise and spin down fermions moving counterclockwise around the edges, illustrated on the middle panel of Figure 1.4. As scattering on non-magnetic impurities does not change the direction of the spin, backscattering vanishes in this case as well [1]. In chapter 4 we study the edge current arising in QSHIs when they are subject to an additional periodic driving.

Though complete back-scattering is suppressed also in the surface states of 3D topological insulators, they are not perfectly conducting because in 2D scattering can not only occur in 180°, but in arbitrary directions. Further interest in the surface states of TIs is that similarly to the electrons in graphene, they are described by the relativistic Dirac equation. In contrast to graphene's 4 Dirac cones (corresponding to valley and spin degrees of freedom), there is only a single Dirac cone at the surface of 3D TIs. In arbitrary 2D systems the Dirac cones have to appear in pairs, and the boundary of the topological insulators is exotic in the sense that it cannot appear as an effective theory for a purely 2D system, which is not a boundary of a higher dimensional system. The three types of topological insulators mentioned so far, and the dispersion relation of their boundary states are illustrated on Figure 1.4. TIs also exist in 1D, which support non-dispersing mid-gap states localized at the two ends of the system.

Experiments followed soon the theoretical advance of the field, the first experimental realization of the QSH insulator was in 2007 in HgTe-CdTe heterostructures [58]. As a function of the thickness of the HgTe layer, a topological phase transition occurs from a normal insulator to a TI phase, which was identified by transport measurements. When the thickness of the middle layer is smaller than a critical value, a regular insulating behaviour is observed, while a HgTe layer exceeding the critical thickness shows a quantized conductivity due to the perfectly conducting edge states. The cartoon of the system and the experimental signatures of the topological edge states are depicted on Figure 1.5.

[1] In contrast to the simplified picture we provided here, the absence of backscattering does not require the conservation of the z component of the spin, only the presence of time reversal symmetry, which is broken e.g. by a magnetic impurity.

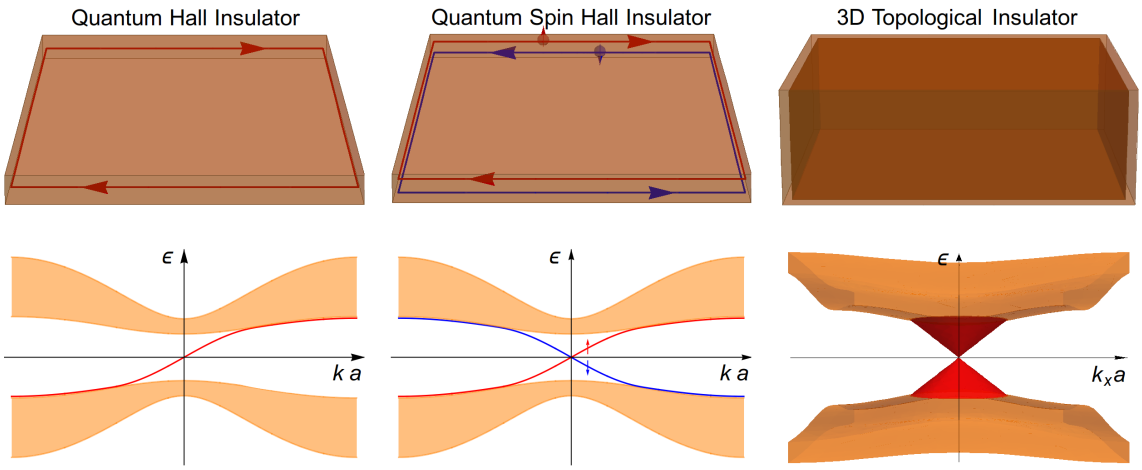

Figure 1.4: Topological insulators are characterized by linearly dispersing robust edge and surface states, whose energy lie in the bulk band gap.

The first 3D topological insulator material $Bi_{1-x}Sb_x$ was found in 2008, which has been followed by many other examples.

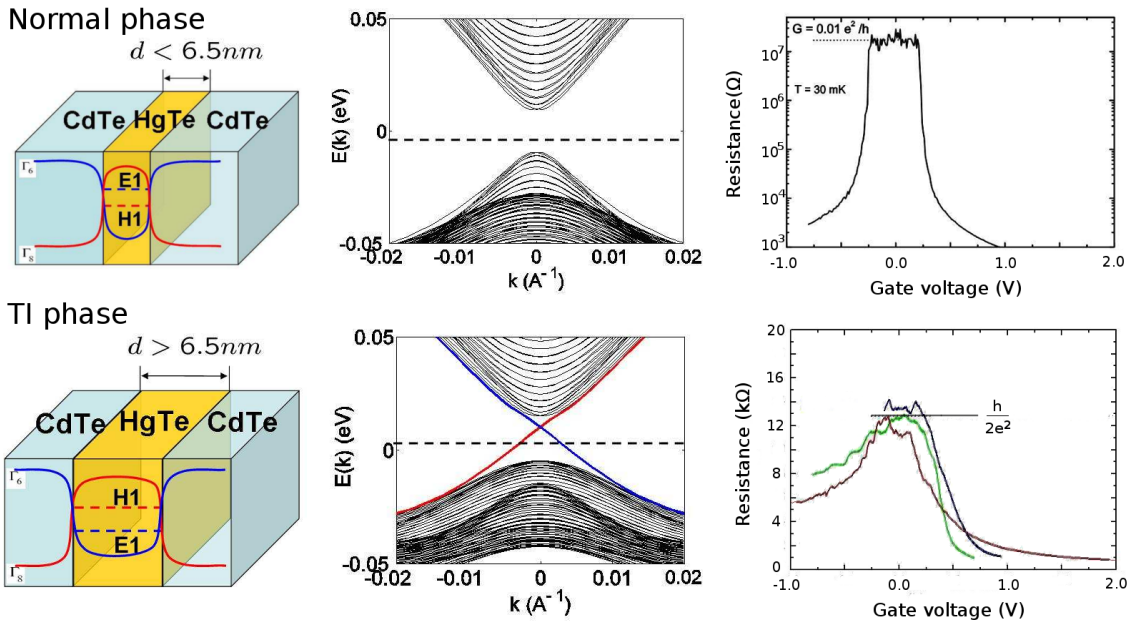

Figure 1.5: Experimental realization of the QSH insulator in HgTe-CdTe heterostructures. The system undergoes a topological phase transition from a normal phase (top) to a TI phase (bottom) as the thickness of the HgTe layer is varied. The huge resistance in the normal phase corresponds to an insulating behaviour, while the TI phase exhibits a resistance plateau at $R = \frac{h}{2e^2}$ due to the perfectly conducting topological edge states. The panels were adopted from the ArXiv version of Ref. [59].

In the level of the BCS theory, superconductors are similar to band insulators in the sense that the excitation spectrum is gapped. The concept of topologically protected edge/surface modes living in the bulk band gap can be generalized to superconductors as well, giving rise to even more exotic modes at the boundary. For instance, they can host

Majorana particles, which are the antiparticles of their own, and their existence had been experimentally demonstrated in highly engineered materials [60, 61].

1.4.1 Topological numbers

An interesting feature of topological insulators is that they are beyond the traditional Ginzburg-Landau description as they exhibit quantum phases without local order parameter. Instead, topologically trivial (normal), and topological insulators are distinguished by topological numbers, which can take values from different sets ($\mathbb{Z}$ or $\mathbb{Z}_2$) depending on the spatial dimension and on the global symmetries of the systems. The bulk-boundary correspondence connects the topological numbers calculated from the bulk with the appearance of surface and edge states. For example in QHE effect, the topological index is the Chern number, the integral of the Berry curvature, which can take any integer values. The Chern number also gives the number of conducting edge states in a finite system. The topological phases are characterized by the dimension and the symmetry class of the systems, and a periodic table of topological insulators and superconductors has been developed [53]. The relevant symmetries are the time reversal symmetry (Θ), the particle-hole symmetry (Ξ), and their product, the chiral symmetry ($\Pi = \Xi\Theta$). These three define the 10 symmetry classes (A, AIII, AI, BDI, D, DIII, AII, CII, C, CI), which are closely related to the Altland-Zirnbauer classification of random matrices.

In section 2.3 we will reveal an interesting impact of the topology on the dynamics of TIs and superconductors following a sudden quench protocol. In particular, we study the A, AIII, BDI and D classes, for which the symmetries and the topological indices are given in Table 1.1. In two-band models the topological invariants for these classes are the winding number or the $\mathbb{Z}_2$ invariant in 1D, and the Chern number in 2D, illustrated in Figure 1.6. The relevant topological indices are defined in section 2.3, in Eqs. (2.36,2.37). We will see that quenches connecting phases with different topological numbers are qualitatively different from quenches within the same phase.

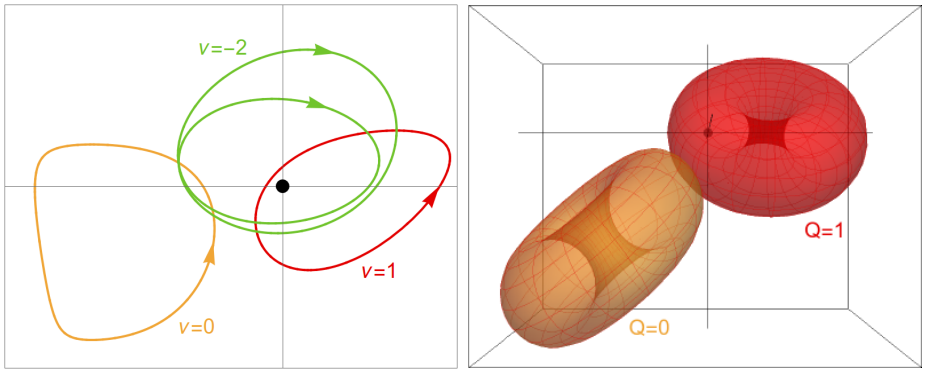

Figure 1.6: The winding number ν is a topological number, which counts the number of times a closed curve winds around the origin in the 2D plane. In in simple cases the Chern number Q is its 3D analog, that is, it counts how many times a closed directed surface encompasses the origin. Without going into the details, these curves and surfaces characterize the many-body ground state wavefunctions of insulators, and they are smooth functions of the parameters appearing in the Hamiltonian.

	Symmetry			Dimension	
Class	Θ	Ξ	Π	1	2
A	0	0	0	0	$\mathbb{Z}$
AIII	0	0	1	$\mathbb{Z}$	0
BDI	1	1	1	$\mathbb{Z}$	0
D	0	1	0	$\mathbb{Z}_2$	$\mathbb{Z}$

Table 1.1: The periodic table of topological insulators and superconductors, restricted to the cases studied in this thesis. Zeros in the "Symmetry" column denote the absense of the symmetry, and ± 1 specifies the value of Θ^2 and Ξ^2. In this restriced table there are no examples with negative sign of Θ^2 and Ξ^2, but generally there are. In the "Dimension" column zeros denote the absense of topological insulator phase and $\mathbb{Z}$, $\mathbb{Z}_2$ characterize the TI phases.

1.4.2 Topological semimetals

Soon after the discovery of topological insulators, it had been noticed that topology can play significant role in gapless sytems as well. As we have discussed, the edge or surface states of topological insulators obey the 1D or 2D Dirac equation. The main interest in the topological Weyl and Dirac semimetals is that they host quasiparticles, which obey the 3D Dirac equation. The Dirac nodes appear as band crossings around some points in the Brillouin zone in these materials. Usually crossings of energy levels are not robust in quantum mechanics, a generic perturbation lifts the degeneracy, unless there is a symmetry protecting it. In contrast, "accidental" band touchings - degenerate points in the spectrum not protected by any symmetries - in 3D materials turn out to be much less accidental, they can be protected by the topology of the band structure. Materials with this property are called Weyl semimetals, because the low-energy physics of these materials mimic the Weyl fermions well known from high energy physics. At the crossing of two *non-degenerate* bands the dispersion relation can be linearized yielding to a Dirac-like effective Hamiltonian $H_{\mathbf{k}} = \epsilon + v(\mathbf{k} - \mathbf{k}^*) \cdot \boldsymbol{\sigma}$, where, for simplicity, we considered isotropic dispersion relation around the Weyl point $\mathbf{k}^*$. The sign of the velocity v characterizes the helicity of the quasiparticles. In contrast to graphene, here all the 3 Pauli matrices $(\sigma_x, \sigma_y, \sigma_z) = \boldsymbol{\sigma}$ appear in the Hamiltonian, and any perturbation proportional to the Pauli matrices can only shift the position of the Weyl node, but it cannot make the Weyl point disappear. Weyl nodes hence can only disappear when they meet with another one of opposite helicity. We can think of these nodes as topological defects in the band structure. More precisely, the nodes of different helicity act like sources and sinks of the Berry curvature of the effective two-level system, defined as $\mathbf{B}(\mathbf{k}) = i\nabla_{\mathbf{k}} \times \langle u_{\mathbf{k}} | \nabla_{\mathbf{k}} | u_{\mathbf{k}} \rangle = \frac{1}{2}\frac{\mathbf{k}}{k^3}$, where $|u_{\mathbf{k}}\rangle$ denotes the ground state of the effective Hamiltonian defined above. The topological charge associated with the Weyl node is the surface integral of the Berry curvature around a surface containing the node, which happens to be the helicity of the Weyl node. A key ingredient in the previous description was the crossings of *non-degenerate* bands, and to achieve this, Weyl semimetals break either inversion or time reversal symmetry.

In contrast to the two-component Weyl fermions in Weyl semimetals, Dirac semimetals are characterized by four-component linearly dispersing low-energy excitations. This can be realized either by having two Weyl nodes with opposite helicity at the same crystal momentum, or by considering a crossing of two doubly degenerate bands [62]. However,

in contrast to the robustness of Weyl nodes, the occurrence of Dirac nodes require either fine-tuning or additional symmetries protecting against mass terms, which otherwise could open a gap at the band crossing.

Condensed matter systems, e.g. graphene, 3D topological insulators and Weyl semimetals, provide unique opportunity to examine fascinating QED effects, like Klein tunneling, Zitterbewegung, chiral anomaly or Schwinger pair production, most of which are barely accessible to experiment otherwise. In addition to this "fundamental" appeal, these phenomena play a crucial role in transport properties of these systems. In chapter 3 we study the Schwinger pair production and its effect on the conductivity of Weyl semimetals after a sudden switching on of an external electric field.

2 Dynamical phase transitions

Phase transitions are amongst the most fascinating phenomena in physics. They describe sharp changes in the properties of the system as a function of temperature or pressure or some other macroscopic parameter. Examples include transitions from water to ice, from metal (or even insulator) to superconductor, from paramagnet to ferromagnet, and many more. In equilibrium, phase transitions are reasonably well understood. Mathematically they are described by singularities in the free energy of the system developing as one crosses this transition. In non-equilibrium systems, which became recently a forefront of research, the situation is much less clear.

Dynamical phase transitions may refer to several different scenarios in the literature. One example is when systems are driven across a (most often second order) phase transition, e.g. by continuously changing the temperature or magnetic field. As opposed to the classical theory of phase transitions, which assumes an infinitely slow process, allowing the system to stay always in equilibrium, the dynamical case may show some interesting additional phenomena, for example the formation of magnetic domains in a magnet, vortices in a superconductor, etc. The corresponding theory describing the scaling of defect generation is called the Kibble-Zurek mechanism, which will be briefly explained in chapter 3. The phase transition might not appear exactly at the equilibrium transition point, but can be slightly shifted dynamically, giving rise to hysteresis. This can be seen e.g. in supercooled liquids, and a similar phenomenon was recently measured in a system with light-matter interaction (Dicke model) [63], which was also called *dynamical phase transition*.

Many-body localization, the localization transition of interacting systems briefly introduced in section 1.1, is also considered as a type of dynamical phase transitions [64], because the transition from a thermalizing (ergodic) phase to the nonergodic MBL phase describes a change in the *dynamics* of the systems.

Another out-of-equilibrium phenomenon, dubbed dynamical (phase) transition, is characterized by the singular behavior of long time averages of certain observables as a function of a control parameter, following a quantum quench. The first examples were found in the Hubbard model [65], and were followed by others e.g. in the Bose-Hubbard model, the Jaynes-Cummings model, the transverse-field Ising model [66] and the ϕ^4 theory [67].

Recently, in 2013, Markus Heyl *et al* [68] showed that one can define dynamical phase transitions (DPTs), where the singularity develops as a function of time after a system

is suddenly kicked from the equilibrium by e.g. an external pulse. This work triggered active research to investigate the properties of dynamical phase transitions [18, 19, 69–92] and experiments as well [93]. In the following we only study DPTs as it was defined in Ref. [68], but we note that recently dynamical transitions in the long time averages of observables and DPTs as singularities in time evolution have been found to be related in some particular models [89], with counterexamples as well [84].

2.1 Theoretical background

2.1.1 The setup and the Loschmidt amplitude

The most robust way to drive a system far from equilibrium is to perform a sudden quench, that is, to change some characteristics of the system or its environment suddenly. As in any other fields of physics, studying the simplest models provide important building blocks to understand the more complicated scenarios, especially for out-of-equilibrium problems, which are inherently more complex than their equilibrium counterparts. Furthermore, these simple systems are of experimental relevance, since they are realized in photonic waveguides [47, 94] and in cold atoms [5, 46]. In this spirit, DPTs have only been studied in closed systems, that is, any dynamical coupling between the environment and the system are neglected. We assume that initially the system rests in equilibrium, more precisely in the ground state of the corresponding initial Hamiltonian. The generalization of the notion of DPTs for finite temperature initial states is nontrivial and has hardly been studied in the literature [81]. Right after the quench, the system is evolved under the new Hamiltonian describing the changed environment. Usually the initial state is not an eigenstate of the new Hamiltonian, and we face a nontrivial time evolution. For the mathematical description we assume that the Hamiltonians are described by a finite set of time-dependent parameters $\{\lambda_i(t)\}$, which are suddenly changed at $t = 0$, such that $\lambda_i(t < 0) = \lambda_i^0$, $\lambda_i(t > 0) = \lambda_i^1$, and $H(\{\lambda_i^0\}) = H_0$, $H(\{\lambda_i^1\}) = H_1$. These parameters also define the phase diagram of the system, and, as it will be shown later, there is a strong relation between the equilibrium phase diagram and the observed dynamics of the system. The quench protocol can conveniently be characterized by the dynamical partition function with no reference to any particular observables, defined as

$$Z(z) = \langle\psi| e^{-Hz} |\psi\rangle \ . \tag{2.1}$$

For positive real values of z, this gives the partition function of a field theory with boundaries $|\psi\rangle$ separated by z [95]. For our purposes, we use $z = it$ with t real, which then gives the Loschmidt amplitude (LA), that is, the overlap of the time evolved state with the initial state is

$$G(t) = Z(it) = \langle\psi| e^{-iHt} |\psi\rangle \ . \tag{2.2}$$

It is also called return amplitude, because $|G(t)|^2$ gives the probability of the time evolved state returning to the initial condition. Analyzing the LA proved to be useful in studying quantum chaos [26], decoherence [27] and quantum criticality [96–98], and is a key concept in DPTs. For a large system $G(t)$ scales exponentially with the system size [99], and in the thermodynamic limit, even states that are parametrically close to each other, are orthogonal. This is a manifestation of Anderson's orthogonality catastrophe [100], and the

LA itself does not give any information about the time evolution. However, the logarithm of the LA divided by the system size,

$$f(t) = -\lim_{N\to\infty} \frac{1}{N} \ln G(t)\,. \tag{2.3}$$

gives an intensive quantity, which, based on the similarity to the definition of the free energy in canonical ensembles, is dubbed *dynamical free energy*. Figure 2.1 shows two qualitatively different behavior of the dynamical free energy of quenches in the transverse field Ising model, which is a 1D quantum spin chain in a homogeneous magnetic field perpendicular to direction of the nearest neighbor spin interaction (its Hamiltonian is $H = \sum_j J\sigma_j^x\sigma_{j+1}^x + h\sigma_j^z$, where $\sigma_j^{x,y,z}$ are the Pauli matrices). In one case the dynamical free energy is a smooth function of time, while in the other kinks appear. The non-analytic behavior of the dynamical free energy was identified as dynamical phase transition in Ref. [68]. As a recap, the analogy between thermal phase transitions and dynamical phase transitions are based on the mathematical similarity of the Loschmidt amplitude and the thermal partition functions. This idea was further elaborated in the original paper of Heyl, where they studied the complex zeros of the (dynamical) partition function, called the Fisher zeros, which give more insight to the nature of (dynamical) phase transitions. This idea and Fisher zeros in general are discussed in sections 2.1.3-2.1.4 in more details.

An experimentally relevant property of the Loschmidt amplitude is that it gives the characteristic function of work done on the system under the quench protocol [25]. The work is not a quantum observable, but rather characterizes thermodynamic processes. Consequently the definition of work requires two energy measurements, one at the beginning and one at the end of the process [8]. In the simple case of the sudden quench experiment described above, the probability density function of the work is conveniently written as $P(W) = \sum_n \delta(W - E_n^1 - E_0^0)|\,\langle\psi_n^1|\psi_0^0\rangle\,|^2$, where $\psi_m^{0/1}$ are the eigenstates of the pre/post-quench Hamiltonians, and $E_m^{0/1}$ are the corresponding eigenvalues. The characteristic function is simply $\int \mathrm{d}t P(W)e^{itW} = e^{-itE_0^0}G(-t)$. We note that this definition of the work is the *inclusive work*, which also accounts for the coupling to the external driving (in contrast to the *exclusive work*, which focuses only on the system). Another interpretation of the Loschmidt echo $|G(t)|^2$, is that it gives the probability of performing zero work in a double quench experiment, when we quench back to the initial Hamiltonian at time t. This is direct consequence of $G(t)$ being the return amplitude. In principle, the LA could be directly measured by coupling the system of interest to an auxiliary qubit [25, 101], and the measurement of the distribution function of work has been reported recently in a closed quantum system [102].

We note that the notion of DPTs can be generalized to ramp protocols as well. Then the return amplitude can be defined either for the initial state [85], that is $G(t) = \langle\psi_0|U(t)|\psi_0\rangle$, where ψ_0 is the initial state and $U(t)$ is the time evolution operator, or for the state achieved at the end of the ramp protocol [78, 82, 90, 103]: $G(t) = \left\langle\psi(\tau)|e^{-iH_f t}|\psi(\tau)\right\rangle$, where τ is the length of the ramp, and $H_f = H(\lambda(\tau))$ is the Hamiltonian at the end of the ramp. Non-analyticities in $G(t)$ were found using both definitions for certain protocols. Quench and ramp protocols provide a natural way to prepare non-equilibrium states, but in principle the LA and the dynamical free energy can be calculated for any pair of initial states and Hamiltonians, with the possibility of finding DPTs. However, it turns out that the occurrence of DPTs are related to equilibrium phase transitions, which motivates the analysis of quench and ramp protocols first, leaving the generic case for future studies.

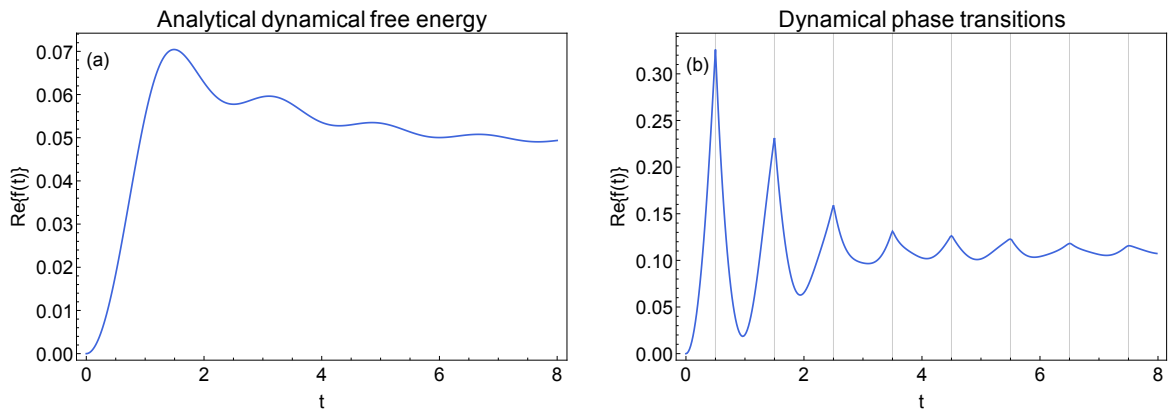

Figure 2.1: Two qualitatively different behavior of the dynamical free energy in the transverse field Ising model: for certain types of quenches the dynamical free energy is an analytical function, for others cusp-like singularities appear, which are identified as dynamical phase transitions. (The curves are generated from Eq. (2.19)).

2.1.2 Relation to the stationary state following the quench

The LA and the dynamical free energy describe the stationary state after the quench [104], which might seem to be surprising, as they gradually emerge from the time evolution of the initial wave function. The state at any time is completely characterized by the density matrix, whose diagonal elements in the eigenbasis of the post-quench Hamiltonian describe the stationary expectation values, as was discussed in section 1.1. As e^{-iH_1t} is diagonal in the eigenbasis of H_1, its expectation value is completely determined by the diagonal ensemble. The dynamical free energy $f(t) = -1/N^d \log(\mathrm{Tr}\,\rho_{DE}e^{-iH_1t})$ in this sense is a characteristic of the diagonal ensemble, that is, of the stationary state, and it provides hope that the presence or absence of DPTs have implication long-time expectation values of operators. The diagonal ensemble contains a lot of information about the initial state, also about non-local correlations, which are not necessary to reproduce the expectation values of local observables. However, the Loschmidt amplitude being a highly nonlocal quantity (as the time evolution operator contains arbitrarily high powers of the Hamiltonian), in general, it cannot be determined by a Gibbs, or a Generalized Gibbs ensemble.

2.1.3 Fisher zeros in thermal phase transitions

M.E. Fisher, borrowing idea from the celebrated Lee-Yang circle theorem, proposed a method to analyze the zeros of the partition function in the *complex temperature plane* [105]. The analysis of the complex partition function provides a good understanding of the non-analytic behaviour of the free energy, a unique characteristic of phase transitions. As we shall see shortly, the key elements are the zeros of the partition function. For a large variety of finite systems, the partition function is an entire function, that is, analytic over the whole complex plane, since it is given by sums of exponential functions $e^{-\beta E_n}$. According to the Weierstass factorization theorem, entire functions can be expressed by

their complex zeros as

$$Z(\beta) = \mathrm{Tr}\{e^{-\beta H}\} = \sum_n e^{-\beta E_n} = e^{-F_{\mathrm{anal}}(\beta)} \prod_j (\beta - \beta_j)\,, \tag{2.4}$$

where β_j are the complex zeros of the partition function, called Fisher zeros, and F_{anal} in the exponent is an entire function, which gives an *analytical* contribution to the free energy density, after taking the logarithm from $Z(\beta)$:

$$f(\beta) = \frac{1}{N^d \beta} \left[F_{\mathrm{anal}}(\beta) - \sum_j \log(\beta - \beta_j) \right] . \tag{2.5}$$

This implies that all possible *non-analyticities* in the thermodynamic limit *are encoded in the Fisher zeros*. In a finite system phase transitions cannot occur, and the Fisher zeros are isolated and do not lie on the real axis. However, in the thermodynamic limit they coalesce into lines (or in general case areas [106]) that can cross the real axis. These crossings are responsible for the breakdown of the analytic continuation of the free energy density as a function of temperature: knowing the free energy above the transition temperature does not give any informations about the free energy below. Figure 2.2 illustrates the above scenario for the Fisher zeros in a hypothetical model, based on Fisher's original cartoon [105].

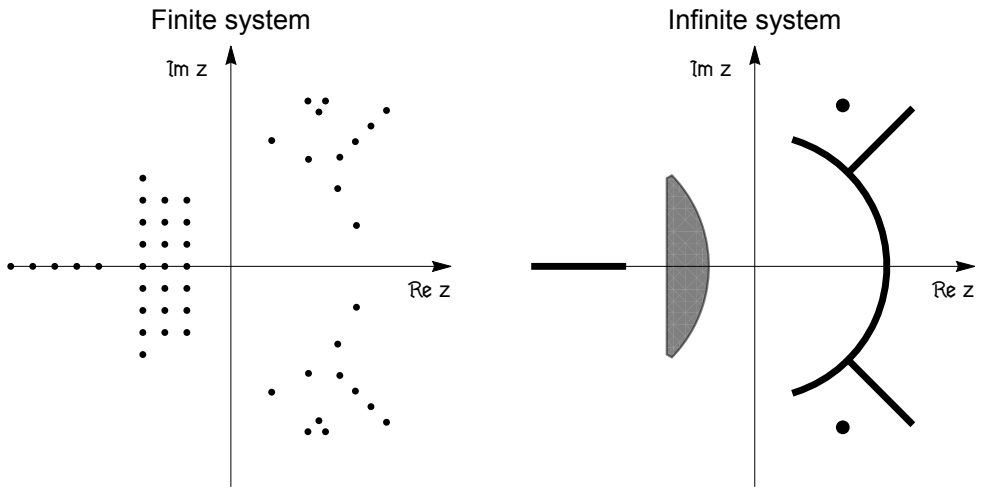

Figure 2.2: Distribution of Fisher zeros in a finite and in an infinite static system. In a finite system, zeros never lie on the real temperature axis ($\mathrm{Re}\, z > 0$), but in the thermodynamic limit they can coalesce to lines, which may cross the real axis giving rise to phase transitions. The plots are based on Fisher's cartoon from Ref. [105].

The Fisher zeros not only provide a new angle to understand the origin of phase transitions, but can also be used to determine the critical behaviour of the systems. The order of the transition is determined by the density of the zeros at the crossings: it is finite at first order transitions, and vanishes as $r^{1-\alpha}$ for continuous phase transitions, where r is the distance from the crossing point, and α is the critical exponent of the specific heat [107]. The correlation length exponent ν for example can be extracted from the finite size scaling of the zero nearest to the real axis [108].

As a side-remark we mention that although the mere definition of the complex temperature partition function might seem to be only an abstract mathematical tool, in principle it is measurable, as it gives the characteristic function of energy contained in the system. A single line derivation follows from the definition of the energy density function: $P(E) = \frac{1}{Z(\beta)} \sum_n e^{-\beta E_n} \delta(E - E_n)$, and $\int \mathrm{d}E e^{-itE} P(E) = \frac{Z(\beta+it)}{Z(\beta)}$.

2.1.4 Fisher zeros in dynamical phase transitions

Similarly to the canonical partition function, the dynamical partition function of Eq. (2.1) is an entire function, and it can be expressed by the complex zeros containing all possible singularities of the dynamical free energy. Following the literature we express the dynamical free energy with the zeros of the dynamical partition function $Z(z) = G(-iz)$,

$$Z(z) = e^{-F_{\mathrm{anal}}(-iz)} \prod_j (1 - \frac{z}{z_n}) \tag{2.6}$$

$$f(t) = \lim_{N\to\infty} \frac{1}{N^d} \left[F_{\mathrm{anal}}(t) - \sum_n \ln\left(1 - \frac{it}{z_n}\right) \right] \tag{2.7}$$

The Fisher zeros corresponding to the quenches of Figure 2.1 are shown on Figure 2.3. In the transverse field Ising model the isolated zeros of finite systems form lines in the thermodynamic limit. If one of these lines crosses the real time axis, then a singularity appears in the dynamical free energy. The properties of this singularity are determined by the position and density of the Fisher zeros near the real time axis. The singular part of (2.6) can be expressed by the integral:

$$\mathrm{Re}\{f_s(t)\} = -\int_{z\in\mathbb{C}} \rho(z) \ln\left|1 - \frac{it}{z}\right| \mathrm{d}z^2 = -\frac{1}{2} \int_{z\in\mathbb{C}} \rho(z) \ln\left(1 - \frac{t^2}{|z|^2}\right) \mathrm{d}z^2\,, \tag{2.8}$$

where ρ is the density of zeros in the complex plane. If a line of Fisher zeros crosses the imaginary axis as in Figure 2.3(b), the corresponding jump in the first derivative of the dynamical free energy can be expressed from Eq. (2.8) following a straightforward, but tedious calculation,

$$\lim_{\epsilon\to 0+} Re\{f'(t_0 + \epsilon) - f'(t_0 - \epsilon)\} = -2\pi\rho_{1d} \cos\varphi \tag{2.9}$$

where ρ_{1d} is the linear density of Fisher zeros at the crossing point, and φ is the angle of incidence of the Fisher line to the imaginary axis, with $\varphi = \pi/2$ being parallel to the real axis. As we will see in section 2.3, in 2D systems areas filled densely with Fisher zeros might cross the imaginary axis. If we consider a strip with homogeneous ρ_{2d} density of the Fisher zeros near the crossing, following an even more tedious calculation, we found that the jump appears in the second derivative of the dynamical free energy as [19]:

$$\lim_{\epsilon\to 0+} Re\{f''(t_0 + \epsilon) - f''(t_0 - \epsilon)\} = -2\pi\rho_{2d} \cos^2\varphi \tag{2.10}$$

One can get this result easier by applying a mapping to a 2D electrostatic problem, where the Fisher zeros play the role of the charges. For this purpose, following the lines of Ref. [109] we define $\phi(z) = \mathrm{Re}\{f_s(-iz)\}$, and notice that the Green function of the 2D

Laplacian is the logarithm: $\Delta \ln|x+iy| = 2\pi\delta(x)\delta(y)$, where $\Delta = \partial_x^2 + \partial_y^2$. Taking the Laplacian of Eq. (2.8) yields

$$\Delta\phi(z) = -2\pi\rho_{2d}(z) \tag{2.11}$$

Schmitt *et al* applied this method to reproduce our result Eq. (2.10) [77].

We note, that in contrast to the equilibrium case, where Fisher zeros never lie on the real temperature axis in finite systems, in the dynamical case isolated Fisher zeros can lie on the time axis. An extreme example is the quench from the Néel state to the XX chain, in which case all the Fisher zeros lie on the time axis [71].

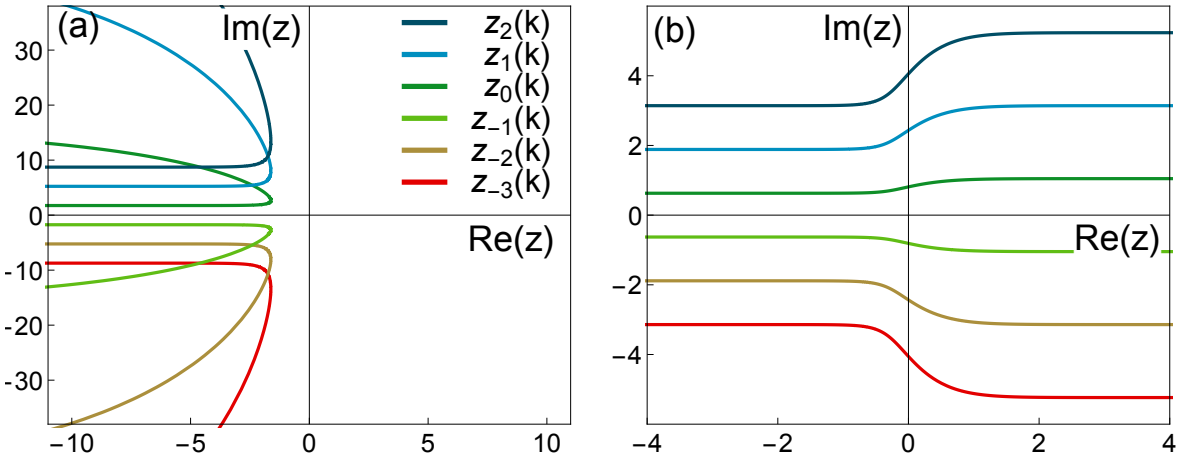

Figure 2.3: Two qualitatively different behavior of the Fisher zeros in the transverse field Ising model for the same quenches as in Figure 2.1. In the thermodynamic limit the zeros form a set of lines $z_n(k)$ indexed by integer numbers n and parametrized by k. (a) the Fisher lines turn back without crossing the time axis ($Im\, z$ axis), (b) they cross the time axis, giving rise to DPTs. (The curves are generated from Eq. (2.21).)

2.1.5 Simple example: a direct mapping to statistical physics

The formal similarity of the Loshmidt amplitude to the canonical partition function at imaginary temperatures becomes an exact mapping in the quench in the transverse Ising model from infinite transverse magnetic field to zero: $h_0 = \infty \to h_1 = 0$. The initial state is fully polarized in the x direction $|\psi_0\rangle = |{\to}{\to}\cdots{\to}\rangle$, and the finial Hamiltonian is $H_1 = J\sum \sigma_i^z\sigma_{i+1}^z$. The initial state in the basis of $|{\uparrow}\rangle$ and $|{\downarrow}\rangle$ spins contains as many orthogonal states as the dimension of the Hilbert space,

$$|\psi_0\rangle = \frac{1}{2^{N/2}}\left(|{\uparrow}{\uparrow}{\uparrow}\ldots{\uparrow}\rangle + |{\downarrow}{\uparrow}{\uparrow}\ldots{\uparrow}\rangle + |{\uparrow}{\downarrow}{\uparrow}\ldots{\uparrow}\rangle + \ldots|{\downarrow}{\downarrow}\ldots{\downarrow}\rangle\right), \tag{2.12}$$

and because of the finial Hamiltonian does not contain any spin flip terms, the LA is expressed as a trace:

$$G(t) = \langle\psi_0|\, e^{-iH_1 t}\,|\psi_0\rangle = \frac{1}{2^N}\,\mathrm{Tr}\, e^{-iH_1 t} = \cos^N(Jt) + (-i)^N \sin^N(Jt)\,, \tag{2.13}$$

where the final result is easily obtained by the standard transfer matrix solution of the 1D Ising model [110]. In the thermodynamic limit either $\cos^N(Jt)$ or $\sin^N(Jt)$ completely dominates the sum and

$$\mathrm{Re}\{f(t)\} = -\lim_{N\to\infty}\frac{1}{N}\ln|G(t)| = \min\{-\ln|\cos(Jt)|, -\ln|\sin(Jt)|\}\,, \tag{2.14}$$

that is, the dynamical free energy switches cyclically between $-\ln|\cos(Jt)|$ and $-\ln|\sin(Jt)|$, giving rise to cusps at $t = \frac{1}{J}\pi/4 + n\pi$, $n \in \mathbb{Z}$. This mapping between the canonical partition function of the 1D Ising model and the Loschmidt amplitude was used to demonstrate scaling and universality at DPTs in Ref. [76]. We note that to express the LA as a trace it was not essential to have all spins pointing to the same direction, but it is necessary that all spins are perpendicular to z axis in the initial state. These states do not appear as a ground states of any simple Hamiltonians, but they give large freedom in the preparation of initial states for example in a cold atomic setting.

2.1.6 Relation between dynamical phase transitions and equilibrium phase transitions

It was found in the transverse field Ising chain that the DPTs and equilibrium phase transitions (EPTs) are ultimately related: The time evolution of $G(t)$ becomes non-analytic whenever the magnetic field is quenched through the (equilibrium) critical value. We have seen a particular example of this in the previous section, but it was generally shown in Ref. [68]. However, it was not clear whether this relation to equilibrium phases is a general feature of DPTs, or just an artefact of the integrable Ising model. Later similar observations were made for non-integrable models [69] and for complex magnetic fields [70].

We showed that this connection is not rigorous [18]. To this aim we investigated the anisotropic XY chain (section 2.2) in transverse magnetic field and demonstrated that, in general, DPTs can occur in quenches within the same phase, i.e. without crossing any equilibrium phase boundaries. A numerical evidence for this phenomenon was also reported in Refs. [71, 104]. In addition, we also presented a counter-example where the quench crosses an equilibrium critical point, but the LA remains analytic. This latter example is not generic as it involves a critical initial or final Hamiltonian. By studying more general models, which contain e.g. the quantum XY spin chain as a special case, we found an interesting relationship between the topological properties of the models and the occurrence of DPTs: DPTs are guaranteed to appear if the topology of the ground states differ in the initial and in the final states [19]. We proved this relation for 2-band topological insulators and superconductors in 1 and 2 dimensions, which is introduced in section 2.3. From a slightly different perspective, this result was generalized to systems with arbitrary number of bands by Huang and Balatsky [88].

2.2 Quantum XY spin chain in magnetic field

A simple generalization of the transverse field Ising model is the XY chain (Figure 2.4), which is still exactly solvable, but it has a much richer phase diagram. The XY Hamiltonian with periodic boundary conditions reads as

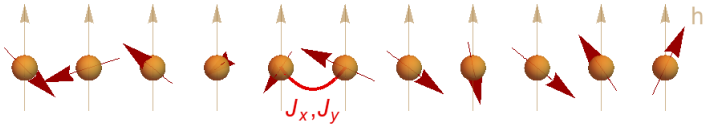

Figure 2.4: The quantum XY spin chain is a 1D lattice of localized spin 1/2 particles in external magnetic field h, with anisotropic nearest neighbor interaction characterized by $J_x = \frac{1+\gamma}{2}$ and $J_y = \frac{1-\gamma}{2}$, see Eq. (2.15).

$$H(\gamma, h) = \sum_{j=1}^{N} \frac{1+\gamma}{2}\sigma_j^x\sigma_{j+1}^x + \frac{1-\gamma}{2}\sigma_j^y\sigma_{j+1}^y - h\sigma_j^z\,, \tag{2.15}$$

where γ and h are the anisotropy parameter and the homogeneous external magnetic field, respectively. The $\gamma = \pm 1$ lines correspond to the transverse Ising model in the x/y direction. The excitation spectrum becomes gapless for $h = \pm 1$ at arbitrary γ, and for $\gamma = 0$ at $-1 \leq h \leq 1$. These critical lines form an "H" letter-like shape, and separate the different phases of the model. Phase I (III) in Figure 2.5 is characterized by spontaneous symmetry breaking with magnetization in the x (y) direction as an order parameter, while phases II and II' describe a disordered phase with polarization in the z direction.

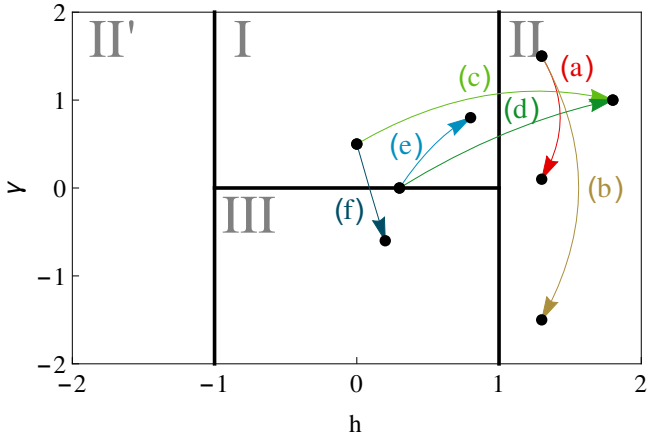

Figure 2.5: The phase diagram of the XY model in magnetic field. The phases (I,II,II',III) are marked on the plot with some examples of qualitatively different quenches. These gapless phases are separated by critical lines that form an "H" letter-like shape.

This model can be mapped to free fermions with the use of Jordan-Wigner transformation (introduced in Appendix A.1) as

$$\begin{aligned} H(\gamma, h) = &\sum_{j=1}^{N-1}[c_j^+c_{j+1} + \gamma c_j^+c_{j+1}^+ - h(c_j^+c_j - \frac{1}{2})] + \text{h.c.} \\ &- [h(c_N^+c_N - \frac{1}{2}) + \mu(c_N^+c_1 + \gamma c_N^+c_1)] + \text{h.c.}\,, \end{aligned} \tag{2.16}$$

where c_j are fermionic operators and $\mu = e^{i\pi N_f}$, $N_f = \sum_{i=1}^{N} c_i^+c_i$. Details of this transformation as well as the solution of the XY chain can be found in many textbooks, for example in Ref. [111]. This Hamiltonian conserves the parity of the particle number and

acts differently on the even and odd subspaces (sometimes referred to as Neveu-Schwarz or Ramond sectors [112]). The Hamiltonian in the two subspaces are formally the same if we impose antiperiodic boundary condition for the even and periodic boundary condition for the odd subspace. In wavenumber space these boundary conditions translate to different quantization of the wave numbers, $k = \frac{2\pi}{N}(n + \frac{1}{2})$ in the even and $k = \frac{2\pi}{N}n$ in the odd subspace. In the fermionic language the ground state is unique in a given subspace, but when $|h| < 1$ the ground states with even and odd parity become degenerate in the thermodynamic limit. These parity eigenstates are the symmetric or antisymmetric combinations of the fully polarized states, they do not possess magnetization in the coupling direction. We start our investigation with the parity eigenstates and we discuss polarized ground states later.

2.2.1 Dynamical free energy

Our goal is to calculate the dynamical free energy for quenches $(\gamma_0, h_0) \to (\gamma_1, h_1)$. A simple way to calculate the LA is to express the initial state with the quasiparticles diagonalizing the final Hamiltonian, and then the time evolution becomes trivial. As it had been mentioned before, the XY Hamiltonian in the fermionic representation acts differently on the even and odd quasiparticle sectors. In the odd sector one needs to separate wave numbers $k = 0$ and $k = \pi$, because for these $-k$ is identical to k. In the even sector this complication does not appear. Following a quench the initial state can be expressed in terms of the fermions f_k that diagonalize the new Hamiltonian: $H_1 = \sum_k \epsilon_k(f_k^+ f_k - 1/2)$ for both sectors, $\epsilon_k = \epsilon_k^1 = 2\sqrt{(\cos(k) - h_1)^2 + (\gamma_1 \sin(k))^2}$. In the even subspace

$$|GS_e\rangle = \prod_{0<k<\pi} [\cos\Theta_k - \sin\Theta_k f_k^+ f_{-k}^+] \, |0\rangle_f^e \ , \tag{2.17}$$

where the product contains all the wave numbers and $|0\rangle_f^e$ denotes the vacuum of the f_k quasiparticles of the even subspace. The angle $\Theta_k = \theta_k^1 - \theta_k^0$ is the difference between the Bogoliubov angles diagonalizing the pre- and post-quench Hamiltonians. The Bogoliubov angles are determined from $e^{i2\theta_k^\alpha} = 2(\cos(k) - h_\alpha - i\gamma_\alpha \sin(k))/\epsilon_k^\alpha$, $\alpha = 0, 1$, and the wave numbers are quantized with respect to the parity of the initial state. In the odd sector the vacuum of the f_k quasiparticles lies in the odd subspace if $|h| < 1$ and in the even subspace if $|h| > 1$.

$$|GS_o\rangle = (f_0^+)^{s_0}(f_\pi^+)^{s_\pi} \prod_{0<k<\pi} [\cos(\Theta_k) - \sin\Theta_k f_k^+ f_{-k}^+] \, |0\rangle_f^o \tag{2.18}$$

where $(s_0, s_\pi) = (0, 0)$ for quenches inside any phases, $(s_0, s_\pi) = (1, 0)$ for quenches from I and III to phase II, $(s_0, s_\pi) = (0, 1)$ for quenches from I and III to II', and $(s_0, s_\pi) = (1, 1)$ for quenches connecting II with II'. With the knowledge of the initial states the Loschmidt amplitude can be calculated easily in both of the even and odd parity sectors:

$$G_s(t) = e^{i\varphi_s(t)} \prod_{0<k<\pi} [\cos(\epsilon_k t) + i\cos(2\Theta_k)\sin(\epsilon_k t)] \ , \tag{2.19}$$

The phase factor satisfies $\varphi_e(t) = 0$ and $\varphi_o(t) = t(\pm\epsilon_0 \pm \epsilon_\pi)/2$, where the signs depend on the position of the initial and final Hamiltonian on the phase diagram, with the same

labeling as in Eq. (2.18) they read:

$$\varphi_o(t) = t/2[(-1)^{s_0+1}\epsilon_0 + (-1)^{s_\pi+1}\epsilon_\pi] \tag{2.20}$$

We focus on the real part of the dynamical free energy, which is the same in thermodynamic limit for both sectors, but the phase becomes important if one is interested in the dynamical free energy starting from the fully polarized initial states.

2.2.2 Fisher zeros

As it had been mentioned before, the non-analytical behaviour of the dynamical free energy is encoded in the zeros of the partition function $Z(z) = G(-iz)$. The simple product form of Eq. (2.19) allows us to determine the Fisher zeros analytically. In the thermodynamic limit they form lines indexed by an integer number n as

$$z_n(k) = \frac{i\pi}{\epsilon_k}(n + \frac{1}{2}) - \frac{1}{\epsilon_k}\,\mathrm{arth}\,[\cos(2\Theta_k)]\ . \tag{2.21}$$

Specially in the XY model the Fisher zeros from $Z(z) = 0$ determine not only the singular part, but the dynamical free energy *completely*, that is,

$$\prod_{n=-\infty}^{\infty}\left(1 - \frac{it}{z_n(k)}\right) = \cos(\epsilon_k t) + i\cos(2\Theta_k)\sin(\epsilon_k t)\,, \tag{2.22}$$

and the entire function in Eq. (2.8) is simply given by $i\varphi_{e/o}(t)$. To see this we use the infinite product representation of the sine function (Ref. [113], page 75.) $\sin(x) = x\prod_{n=1}^{\infty}\left(1 - \frac{x^2}{\pi^2 n^2}\right)$ to prove that $\prod_{n=-\infty}^{\infty}\left(1 - \frac{2x}{\pi(2n+1)+2a}\right) = \cos(x) + \sin(x)\tan(a)$, to which we can readily substitute $z_n(k)$ to get Eq. 2.22.

Eq. (2.21) agrees formally with Ref. [68], but in our case, the Bogoliubov angles depend on more variables, hence are more general function of k. This increased freedom leads to interesting behaviour of the Fisher lines. The main quantity that determines the dynamical free energy is $\cos(2\Theta_k)$, which can be expressed analytically with the parameters of the initial and final Hamiltonian. Furthermore, $\cos(2\Theta_k) = 1-2n_k$, where n_k is the expectation value of the quasiparticle occupation number in the post-quench Hamiltonian and is conserved under the time evolution. A Fisher line crosses the imaginary axis whenever $n_k = 1/2$, which can be interpreted as modes with infinite effective temperature. These crossings are responsible for the non-analytic time evolution of the dynamical free energy.

Due to the parity of the cosine function it is evident that if a Fisher line crosses the imaginary axis for a quench $(h_0, \gamma_0) \to (h_1, \gamma_1)$ it implies a crossing in the reversed protocol $(h_1, \gamma_1) \to (h_0, \gamma_0)$ as well. We call this as the symmetric property of DPT. This seems to be plausible in quenches crossing critical points, but it is less trivial for quenches within the same phase.

The Fisher lines, and hence the LA show different behaviour for quenching between different regions in the phase diagram. The exact values of the initial and final parameters h_0, γ_0, h_1, and γ_1 in given phases do not modify qualitatively the behaviour of the LA as a sign of some kind of universality. We consider 4 types of quenches, 3 of them can be realized with quenching one parameter only, while in third example one needs to quench both the magnetic field and the anisotropy parameter.

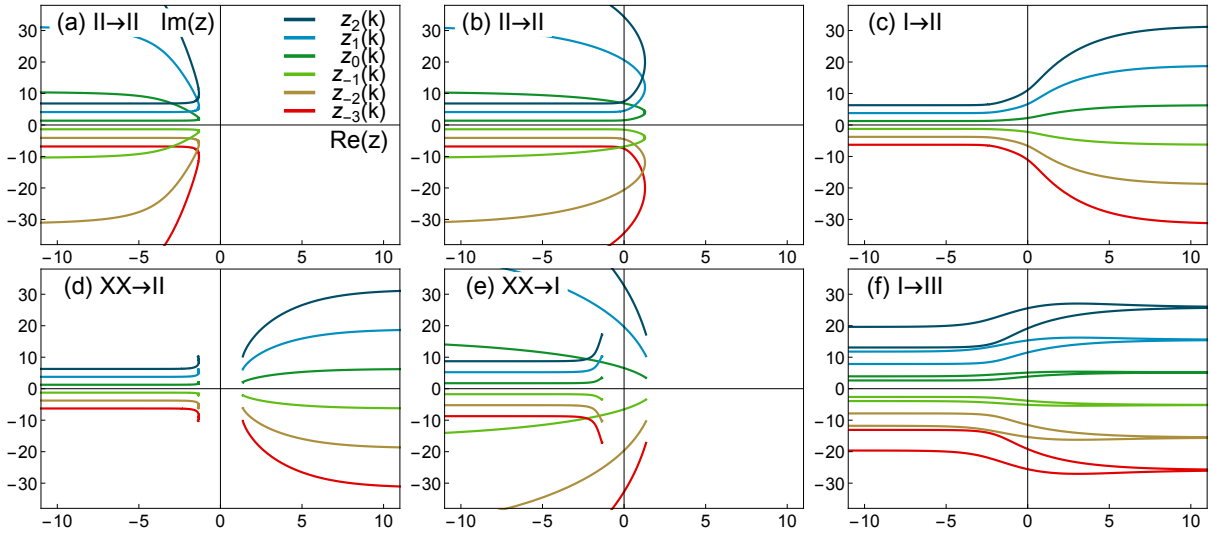

Figure 2.6: The flow of Fisher lines $z_n(k)$ $(n = (-3, \ldots, 2))$ for various types of quenches discussed in the text, and shown in Figure 2.5.

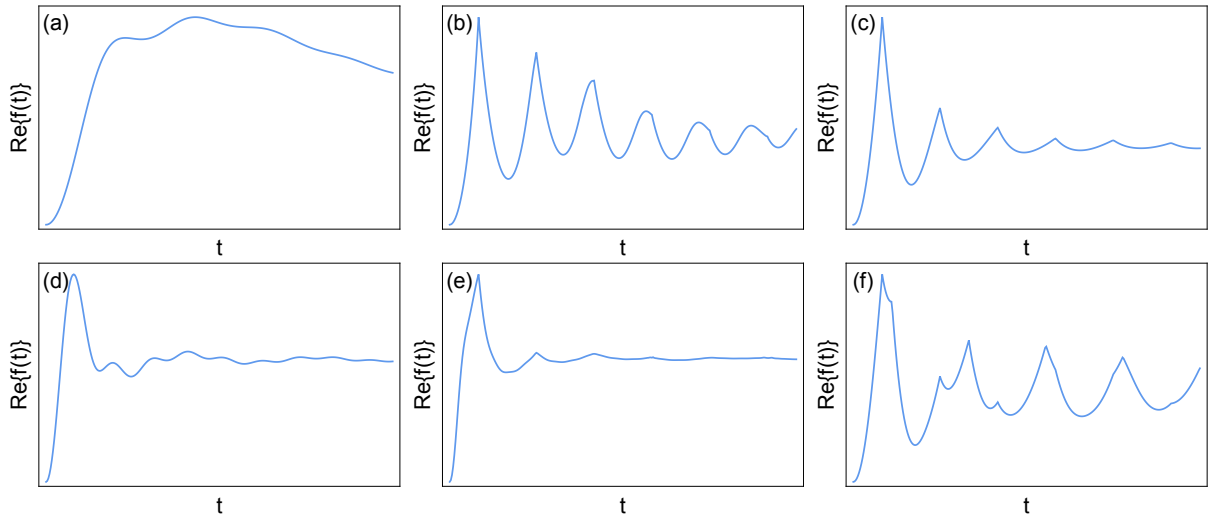

Figure 2.7: Dynamical free energy for the quenches in Figures 2.5 and 2.6. DPTs are seen in (b), (c), (e) and (f).

2.2.3 Examples

DPT without EPT: Quenches not crossing critical points. We start our discussion with quenches inside phase II, where $h_{0,1} > 1$ and we assume that $\gamma_0 > 0$ without loss of generality. In this setup no critical lines are crossed by the parameters of the Hamiltonian during the quench, but DPTs can occur (Figure 2.7(b)). Generally one can show that the $k \to 0, \pi$ tails of the Fisher lines lie in the left half plane: $\lim_{k\to 0} \mathrm{Re}\{z_n(k)\} = -\infty$ and $\lim_{k\to\pi} \mathrm{Re}\{z_n(k)\} = -\infty$. For small quenches the whole lines lie in the left half plane (Figure 2.6(a)), hence the time evolution of the dynamical free energy is analytical. However, the turning point of the Fisher lines can move to the right half plane (Figure 2.6(b)). In this case each Fisher line crosses the time axis twice at wave numbers k_1^* and k_2^*. The non-analytical times are given by $t_i^* = \frac{\pi}{\epsilon_{k_i^*}}(n + \frac{1}{2})$, $i = 1, 2$. This occurs if the anisotropy

parameter is quenched to a sufficiently negative value at fixed magnetic field. No matter how γ is quenched, an equilibrium critical point is never approached, but DPT shows up.

More generally for each point (h_0, γ_0) in phase II , the domain $\mathcal{D}(h_0, \gamma_0) \subset II$ of (h_1, γ_1), where DPT occurs is given by

$$\mathcal{D}(h_0, \gamma_0) = \{(h_1, \gamma_1) | 2\gamma_0\gamma_1 < 1 - h_0h_1 - \sqrt{(h_0 - 1)(h_1 - 1)}\} \tag{2.23}$$

within phase II. The boundary of these regions is a second order curve (a cone-section). A few examples for these domains are shown on Figure 2.8.

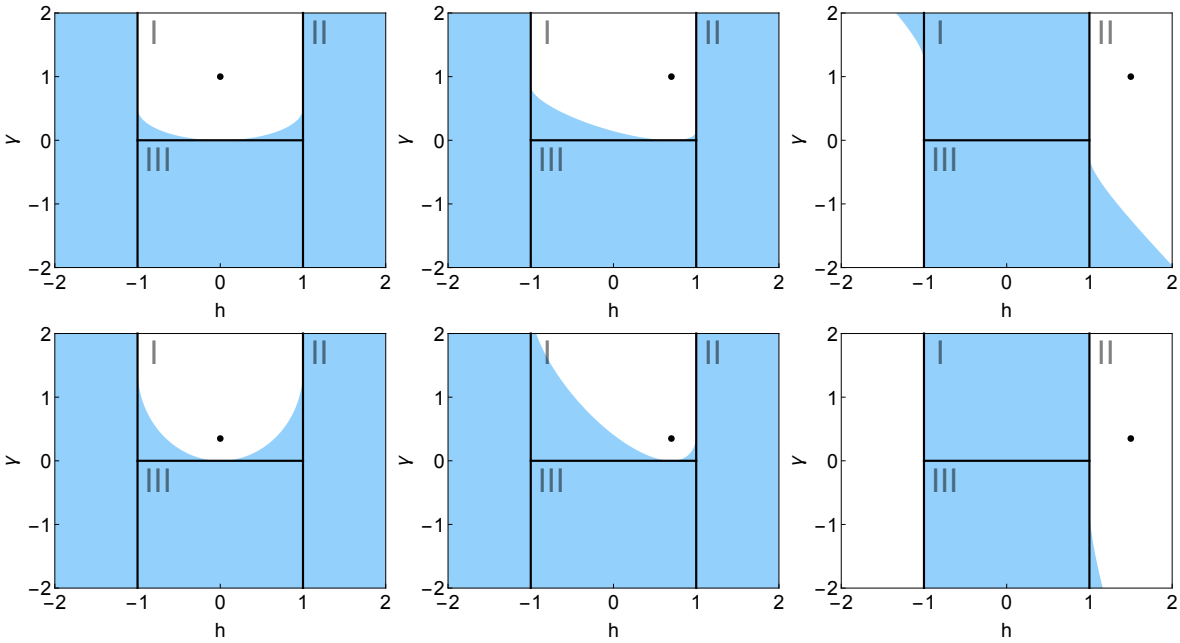

Figure 2.8: DPTs can occur in quenches within the same phase. The domains $\mathcal{D}(h_0, \gamma_0)$ of the final parameters where DPTs appear are shown for six different initial conditions (h_0, γ_0). Except from the region $h_1 < -1$ the domains are determined from Eq. (2.23). Note that when quenching from II to $h_1 < -1$, non-analyticities only show up in the top-left corner of the phase diagram and remain absent otherwise, in spite of crossing several critical lines.

Similar phenomenon can be observed in quenches inside phase I. The Fisher lines start and end in the left half of the complex plane, but some parts of the lines can move to the right half plane. Given (h_0, γ_0) in phase I the domain of final parameters where the non-analyticities occur is given by Eq. (2.23) within phase I. For example starting from the Ising model ($\gamma_0 = 1$, $h_0 = 0$) one needs to quench the magnetic field and the anisotropy parameter as well to see the non-analytic behaviour (see Figure 2.8 top-left corner). However, considering smaller anisotropy the DPT can appear by quenching solely the magnetic field (Figure 2.8 bottom-left corner) when $\gamma_0 < \sqrt{1 + |h_0|}/\sqrt{2}$ is satisfied for the initial Hamiltonian.

DPT together with EPT: Quench between phases I and II. In this setup the quenched parameters cross at least one critical point, and the time evolution of the dynamical free energy is always non-analytical. The asymptotic behaviour of the Bogoliubov angles guarantee that the Fisher lines cross the imaginary axis, that is, $\lim_{k\to 0} \mathrm{Re}\{z_n(k)\} = \infty$ and $\lim_{k\to\pi} \mathrm{Re}\{z_n(k)\} = -\infty$ (Figure 2.6(c)). Because of the symmetries of the XY model quenches between phase II and III behave in the same way.

EPT without DPT: Quench from phase II to the critical XX line ($\gamma = 0$, $|h| < 1$). In quenches $II \to I, III$ DPTs showed up everywhere except for quenches from phase II to the boundary of I and III. Though the asymptotic behaviour of the Bogoliubov angles are similar to the $I \to II$ case, there is an interesting difference as well: there are no Fisher zeros in the vicinity of the imaginary axis. The function $\cos(2\Theta_k)$ is not continuous at $\tilde{k} = \arccos(\frac{h_1\gamma_0 - h_0\gamma_1}{\gamma_0 - \gamma_1})$, therefore $\lim_{\epsilon\to 0^+} \cos(2\Theta_{\tilde{k}\mp\epsilon}) \lesseqgtr 0$. Hence the Fisher lines split into two sections that do not cross the imaginary axis (Figure 2.6(d)).

By considering the XX line as the $\gamma_1 \to 0$ limit, then as we approach the XX line the slope of $\cos(2\Theta_k)$ diverges at $\tilde{k}$, hence the density of Fisher zeros vanishes near the imaginary axis. As opposed to previous examples, when the initial and final Hamiltonians lied in the gapped phase, quenching to the XX line is a special case because the final parameters are on a critical line. Nevertheless, it is still surprising that for quenches $II \to I, III$ DPTs occur everywhere except for the boundary of these regions.

However, non-analytical behaviour in the dynamical free energy can be observed in quenches to the critical lines as well. One example is a quench from I or III to the XX line: $(\gamma_0 \neq 0, |h_0| < 1) \to (\gamma_1 = 0, |h_1| < 1)$ with $h_1 \neq h_0$. In this case, one would think naively the Fisher lines would cross the imaginary axis twice similarly to quenches $I \to I$ and $I \to III$, but one of the crossings does not manifest itself (Figure 2.6(e)) in a similar manner as it was discussed in the previous paragraph. The other example, which we only mention here, is a quench crossing a critical line [1]: starting from III to the $h = 1$ critical boundary of I.

Quench from phase I to III. In this case the anisotropy parameter is quenched from positive to negative values in low magnetic field ($-1 < h_{0,1} < 1$). The system goes through an anisotropy transition at $\gamma = 0$. At $\gamma > 0$ the ground state polarization is in the x, while at $\gamma < 0$ it is in the y direction. For these quenches $\lim_{k\to 0,\pi} \mathrm{Re}\{z_n(k)\} = -\infty$ meaning that the Fisher lines start and end at the left half plane. However, there is wavenumber $0 < \tilde{k} < \pi$ defined by $\cos(\tilde{k}) = \frac{h_1\gamma_0 - h_0\gamma_1}{\gamma_0 - \gamma_1}$, for which $\cos(2\Theta_{\tilde{k}}) = -1$. This means that while k goes through the interval $(0, \pi)$ the Fisher lines come from $\mathrm{Re}\{z\} = -\infty$, reach $\mathrm{Re}\{z\} = \infty$ at $\tilde{k}$ and finally go back to $\mathrm{Re}\{z\} = -\infty$ again (Figure 2.6(f)). Hence all the Fisher lines cross the imaginary axis twice giving rise to two emergent timescales in the dynamical free energy (Figure 2.9(a)). This is qualitative difference between the quenches I to II and I to III.

2.2.4 Longitudinal magnetization

For EPTs, the non-analyticity of the free energy is also imprinted in the non-analytic behaviour of other physical quantities, e.g. the order parameter or its susceptibility. A similar phenomenon is expected to occur for the DPTs as well [68]. For the XY model, the equilibrium order parameter is the magnetization in the XY plane. Therefore, we determined its absolute for the non-equilibrium situation by numerical evaluation of Pfaffians [114]. Whenever the Fisher line crosses the imaginary axis once, only a single emergent non-equilibrium timescale appears from the dynamical free energy, which matches exactly that of the magnetization. However, for quenches $I \to I$ and $I \to III$ each Fisher line crosses the imaginary axis twice which implies two non-equilibrium timescales. Only these

[1] By this we mean that any curves connecting the initial and final parameters cross at least one critical lines.

two timescales and their higher harmonics (in Figure 2.9(d)) appear in the dynamics of magnetization, though generally we were not able to express analytically the zeros of the magnetization by the non-analytic timescales. The red curves in Figure 2.9 demonstrate that the two timescales with exponential decay can reproduce the dynamics of the longitudinal magnetization, with the following ansatz:

$$|m(t)| \approx C|\cos(\epsilon_{k_1^*}(t-t_0))\cos(\epsilon_{k_2^*}(t-t_0))|e^{-\lambda t} \tag{2.24}$$

$$|m(t)| \approx C|\cos((\epsilon_{k_1^*}+\epsilon_{k_2^*})(t-t_0)) + c\cos((\epsilon_{k_1^*}-\epsilon_{k_2^*})(t-t_0))|e^{-\lambda t} \tag{2.25}$$

However, in the $I \to III$ quench protocol when γ_0 and γ_1 are not too close to the $\gamma = 0$ critical line, the magnetization takes zero values in the vicinity of the Fisher times (Figure 2.9(a,b)). The connection between the dynamics of the order parameter and the Loschmidt amplitude was elaborated by Markus Heyl in Ref. [75].

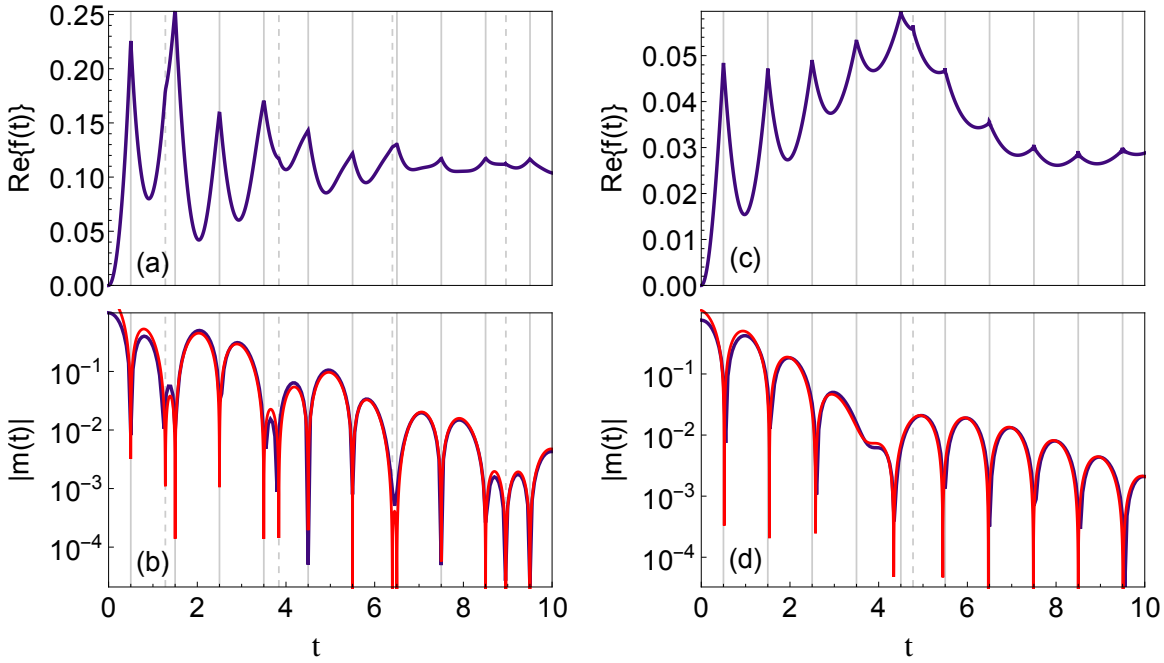

Figure 2.9: The dynamical free energy is non-analytical at Fisher times $t_{i,n} = t_i^*(n+1/2)$ $i = 1, 2$ (solid and dashed lines respectively). The time unit was chosen to be t_1^*. The longitudinal magnetization also shows two timescales, in case (b) the zeros of the magnetization approximately lie at the Fisher times, in (d) the relation between them is more involved. Quench parameters for (a) and (b) are $(h_0 = 0, \gamma_0 = 1) \to (h_1 = 0.6, \gamma_0 = -1)$ and for (c) and (d) are $(h_0 = 0, \gamma_0 = 0.1) \to (h_1 = 0.6, \gamma_0 = 0.1)$. The red curves consist of the two dynamical timescales of the form given in Eqs. (2.24,2.25).

2.2.5 Stationary states

As we have discussed in section 2.1.2, DPTs characterize the stationary state following the quench. For simplicity let us consider only the even subspace. From Eq. (2.17) the initial and the time evolved density matrix can be easily constructed in the basis

diagonalizing the post-quench Hamiltonian:

$$\rho(t) = \prod_{0<k<\pi} \{n_k n_{-k} - \cos^2\Theta_k(n_k + n_{-k}) + \cos^2\Theta_k \\ -e^{i\epsilon_k t}\cos\Theta_k \sin\Theta_k f_{-k} f_k - e^{-i\epsilon_k t}\cos\Theta_k \sin\Theta_k f_k^+ f_{-k}^+\} \ . \tag{2.26}$$

The density matrix is the tensor product of the reduced density matrices of $(-k, k)$ subspace. In the basis $|n_k n_{-k}\rangle$, that is $|00\rangle$, $|01\rangle$,$|10\rangle$ and $|11\rangle$ the density matrix is

$$\rho(t) = \prod_{0<k<\pi} \otimes \begin{pmatrix} \cos^2\Theta_k & 0 & 0 & -e^{i\epsilon_k t}\cos\Theta_k \sin\Theta_k \\ 0 & 0 & 0 & 0 \\ 0 & 0 & 0 & 0 \\ -e^{-i\epsilon_k t}\cos\Theta_k \sin\Theta_k & 0 & 0 & \sin^2\Theta_k \end{pmatrix} \tag{2.27}$$

The stationary behavior of observables (if it exists) is determined by the time average of the density matrix $\bar{\rho} = \lim_{T\to\infty} \frac{1}{T}\int_0^T \rho(t)\mathrm{d}t$, which is the diagonal ensemble for nondegenerate Hamiltonians. For example when $h_1 = 0$, $\epsilon_k = \epsilon_{\pi-k}$ and the process $f_{\pi-k}^+ f_{k-\pi}^+ f_k f_{-k}$ is non vanishing in the stationary state. As the time evolution is diagonal in the quasiparticles f_k, the non-diagonal elements of $\bar{\rho}$ does not influence the Loschmidt amplitude, but for the stationary expectation value of a general physical quantity one should take into account these terms. The diagonal density matrix depends only the fermion occupation numbers n_k and it can be expressed explicitly as

$$\rho_{DE} = \prod_{0<k<\pi} (n_k n_{-k} + \cos^2(\Theta_k)(1 - n_k - n_{-k})) \tag{2.28}$$

$$= \prod_{0<k<\pi} \cos^2(\Theta_k)\delta_{n_k,0}\delta_{n_{-k},0} + \sin^2(\Theta_k)\delta_{n_k,1}\delta_{n_{-k},1} \tag{2.29}$$

From the latter form it is straightforward to reproduce Eq. (2.19). The correlation between wave numbers k and $-k$ come from the BCS superconductor-like initial state. The Loschmidt amplitude - up to a trivial phase factor - is the characteristic function of work done on the system [8], hence it depends on all moments of the energy. As it is a non-local quantity the generalized Gibbs ensemble $\rho_{GGE} \sim e^{\sum \lambda_k n_k}$, where λ_k fixes the expectation value of n_k, would not give the proper result for the LA, because it does not describe well the correlations between n_k and n_{-k}. With the diagonal ensemble in Eq. (2.28), we took into account the correlations among the modes hence it can be applied to calculate any moment of the energy.

2.2.6 Polarized initial states

Until now we considered quenches starting from even or odd parity eigenstates. It is an important question whether the non-analytic behaviour is present in quenches starting from polarized states or not. For quenches through the critical point in the transverse field Ising model it has been shown that DPTs can be observed, but the non-analyticities are not at the Fisher times of the parity subspaces [68, 69]. We found similar behaviour in the XY model. The polarized states are superpositions of the even and odd ground states: $|GS_{pol,\pm}\rangle = \frac{1}{\sqrt{2}}(|GS_e\rangle \pm |GS_o\rangle)$. The Hamiltonian conserves the parity, hence the

LA of the polarized state is simply the average of overlap calculated in the even and odd ground states:

$$G_{pol}(t) = e^{i\phi_e(t)}|G_e(t)| + e^{i\phi_o(t)}|G_o(t)| \tag{2.30}$$

where we decomposed the complex overlap to the absolute value and a phase factor. We note that $\phi_{e/o} \neq \varphi_{e/o}$ from Eq. (2.20), because there is a complex contribution from each k in the product $G_{e/o}(t) = e^{i\varphi_{e/o}} \prod_k |G_k(t)|e^{i\phi_k(t)}$. In Ref. [80] a dynamical topological order parameter, which changes its value at every DPT point, was introduced from (the geometrical part of) $\phi_k(t)$.

The overlap $G_{pol}(t)$ can be evaluated numerically, and we found that the dynamical phase transitions occur in the polarized case as well. We observed that the phase difference $\phi_e(t) - \phi_o(t)$ is a piecewise constant function in the thermodynamic limit. At $t = 0$ the phase difference is zero, and it is changed by π at the Fisher points (see Figure 2.10). This means that depending on the time $|G_{pol}(t)| = ||G_e(t)| \pm |G_o(t)||$. Though real parts of the dynamical free energies f_e and f_o are equal in the thermodynamic limit, this does not imply that $|G_{pol}(t)|$ would be identically zero at certain intervals, because of the division by the system size in the definition of the dynamical free energy. The non-analytic behaviour of the dynamical free energy for polarized initial state is encoded in the small difference between $|G_e|$ and $|G_o|$.

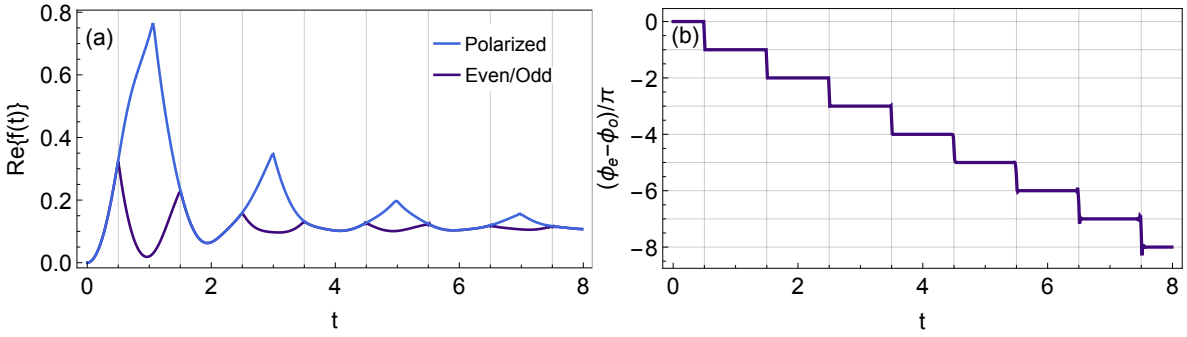

Figure 2.10: (a) dynamical free energy from parity eigenstates and polarized initial states. (b) the phase difference of the Loschmidt overlaps in the even and the odd sectors.

2.3 Dynamical phase transition and topology

The main message of the previous section was that dynamical phase transitions can occur in quenches inside a given phase. As a side-result we observed qualitatively different behaviour of the Fisher lines for quenches connecting different phases. In quenches connecting phase I with phase III the Fisher zeros span the real axis *twice*: they start from $\pm\infty$, reach $\mp\infty$, than they bend back and finally reach $\pm\infty$ again (Figure 2.6(f)). As a consequence, two non-equilibrium timescales emerge. In quenches connecting phases I or III with phase II, the Fisher lines sweep through the real axis only *once* (Figure 2.6(c)). In quenches inside any phase, the Fisher lines start from $\pm\infty$, and they bend back to $\pm\infty$ without spanning the whole real axis, or we might translate it as spanning the real axis *zero* times (Figure 2.6(a,b)).

The fermionic representation of the XY chain in a given parity sector is equivalent to the Kitaev wire [115], which is one of the simplest examples of topological superconductors.

It is a tight-binding chain of spinless fermions with a BCS pairing term describing p-wave superconductivity. The Hamiltonian reads

$$H = \sum_{j=1}^{N} (c_j^+ c_{j+1} + c_{j+1}^+ c_j) + \Delta(c_j^+ c_{j+1}^+ + c_{j+1} c_j) - \mu(c_j^+ c_j - \frac{1}{2}) \,, \tag{2.31}$$

which is indeed the same as Eq. (A.5), following the idenfication of the anisotropy parameter γ of the XY chain with the superconducting gap Δ and twice the magnetic field $2h$ with the chemical potential μ of the Kitaev wire. This model hosts exotic topological edge modes, Majorana fermions, which are their own antiparticles. In addition to the fundamental interest in particles showing exotic statistics, Majorana fermions could be used as building blocks of (topological) quantum computers [116]. These perspectives also motivated experimental groups to realize the Kitaev wire [60, 61].

In the topological superconductor language, the phases I,II and III of the XY chain are characterized by topological winding numbers 1, 0 and -1 respectively. We can now observe, that the *difference between the winding numbers of the initial and final phases is equal to the number of times the Fisher lines sweep through the real axis in the corresponding quench.* It might seem to be a sole coincidence, especially considering that the winding numbers classify the ground-state topology of the system, and quench protocols create highly excited states. In contrast, we show in this section that the above relation holds for a wide variety of systems, and can also be generalized to higher dimensions.

It turned out that the key element in DPTs is not the superconducting correlations in the transverse Ising or XY chain, but rather the topology of the underlying fermionic model. For this reason, we consider 2-band translational invariant insulators and Bogoliubov-de Gennes superconductors in 1 and 2 dimensions, and we treat them together in a generalized notation. Such systems are widely studied in the literature, and some of them had already been realized experimentally, either in cold atomic or in condensed matter systems [46, 60, 61, 117]. The Hamiltonian for these systems can be parametrized by a vector $\mathbf{d_k}$,

$$H = \sum_{\mathbf{k}} \mathbf{c}_\mathbf{k}^+ h_\mathbf{k} \mathbf{c}_\mathbf{k} \tag{2.32}$$

$$h_\mathbf{k} = \mathbf{d_k} \cdot \boldsymbol{\sigma} \,, \tag{2.33}$$

where $\mathbf{c}_\mathbf{k}^+ = (c_{\mathbf{k},A}^+, c_{\mathbf{k},B}^+)$ for insulators and $\mathbf{c}_\mathbf{k}^+ = (c_\mathbf{k}^+, c_{-\mathbf{k}})$ for superconductors. In the insulating case the internal degrees of freedom A, B refer to pseudo-spin components, e.g. to different sublattices. A sudden quench protocol can be described by the change in the vector fields characterizing the Hamiltonian: $\mathbf{d_k}(t) = \mathbf{d}_\mathbf{k}^0$ for $t < 0$ and $\mathbf{d_k}(t) = \mathbf{d}_\mathbf{k}^1$ for $t > 0$. The Loschmidt amplitude following this quench can be expressed in a compact form independently of the spatial dimensions:

$$G(t) = \prod_{\mathbf{k}} \left[\cos(\epsilon_\mathbf{k}^1 t) + i \, \hat{\mathbf{d}}_\mathbf{k}^0 \cdot \hat{\mathbf{d}}_\mathbf{k}^1 \sin(\epsilon_\mathbf{k}^1 t) \right] \,, \tag{2.34}$$

but the product is taken for all wavenumbers in the Brillouin zone for normal insulators and for half of the Brillouin zone for superconductors (e.g. as we had in Eq. (2.19)).

Here, $\hat{\mathbf{d}}^i_{\mathbf{k}}$ denotes the unit vector in the direction of $\mathbf{d}^i_{\mathbf{k}}$ and $\epsilon^i_{\mathbf{k}} = |\mathbf{d}^i_{\mathbf{k}}|$ for insulators and $\epsilon^i_{\mathbf{k}} = 2|\mathbf{d}^i_{\mathbf{k}}|$ for superconductors. The Fisher zeros, i.e. the solutions of $Z(z) = 0$ are

$$z_n(\mathbf{k}) = \frac{i\pi}{\epsilon^1_{\mathbf{k}}}(n + \frac{1}{2}) - \frac{1}{\epsilon^1_{\mathbf{k}}} \operatorname{arth}\left[\hat{\mathbf{d}}^0_{\mathbf{k}} \cdot \hat{\mathbf{d}}^1_{\mathbf{k}}\right], \tag{2.35}$$

which follow from the product form of the Loschmidt amplitude. The Fisher zeros fill domains of the complex plane, which are indexed by an integer number n and are parametrized with $\mathbf{k}$. In 1D these domains form lines, while in 2D they fill areas. The necessary condition to observe DPTs is having Fisher zeros approaching the imaginary axis, which occurs when $\mathbf{d}^0_{\mathbf{k}} \cdot \mathbf{d}^1_{\mathbf{k}} = 0$, i.e. when the vector $\mathbf{d}_{\mathbf{k}}$ in the final Hamiltonian is perpendicular to the initial one for some $\mathbf{k}$. This geometrical condition connects DPTs with the topology of the initial and the final systems. In the following we will consider the 1 and 2 dimensional cases separately.

2.3.1 One dimensional case

Topological insulators in 1D are characterized by chiral (AIII symmetry class) or chiral and particle-hole symmetry (BDI) [118], which constrain $\mathbf{d}_k$ to lie in a 2D plane. The corresponding topological number is the winding number: the number of times $\mathbf{d}_k$ winds around the origin when k sweeps through the Brillouin zone. If, for example $\mathbf{d}_k$ lies in the xy plane,

$$\nu = \frac{1}{2\pi} \int \mathrm{d}k \, (\hat{d}^x_k \partial_k \hat{d}^y_k - \hat{d}^y_k \partial_k \hat{d}^x_k). \tag{2.36}$$

> If the winding number of two vector fields $\mathbf{d}^0_k$ and $\mathbf{d}^1_k$ defined on the Brillouin zone (S^1) differ by $\Delta\nu \in \mathbb{N}$, the image of the scalar product field $\hat{\mathbf{d}}^0_k \cdot \hat{\mathbf{d}}^1_k$ covers the interval $[-1, 1]$ at least $2\Delta\nu$ times.

This means that the Fisher zeros in equation (2.35) sweep through the real axis $2\Delta\nu$ times while k goes through the Brillouin zone. Consequently there are at least $2\Delta\nu$ points in k space where the vectors are perpendicular (for illustration see Figure 2.11(a)), implying DPTs. Let us suppose that the (ground state) winding number of the initial (final) Hamiltonian is ν_0 (ν_1), then the angle of rotation ϕ^i_k for $\mathbf{d}^i_k$ is a smooth function differing by $2\pi\nu_i$ at $k = -\pi$ and π for $i = 0, 1$. The angle of rotation $\Delta\phi_k$ between $\mathbf{d}^0_k$ and $\mathbf{d}^1_k$ changes $2\pi\Delta\nu$, hence $\hat{\mathbf{d}}^0_k \cdot \hat{\mathbf{d}}^1_k = \cos(\Delta\phi_k)$ covers the interval $[-1, 1]$ at least $2\Delta\nu$ times. If the model has further symmetries that connect wavenumbers k and $-k$ (e.g. inversion or time reversal symmetry (TRS)), the Fisher lines can be doubly degenerate and there will be only $\Delta\nu$ non-equilibrium timescales, as it happens for example in the Su-Schrieffer-Heeger (SSH) model (see later).

Our argument applies also for 1D topological superconductors (e.g. the Kitaev wire and its generalization for higher winding numbers [119]) with a little modification. Now the product is taken only for positive momenta in the Loschmidt amplitude in Eq. (2.34). The Bogoliubov Hamiltonian is particle-hole symmetric (PHS) by construction, implying that the x and y components of $\mathbf{d}_k$ are odd and the z component is even function of the wavenumber: $d^x_{-k} = -d^x_k$, $d^y_{-k} = -d^y_{-k}$ and $d^z_{-k} = d^z_k$. For the degenerate momenta $k = 0, \pi$, the vector describing the Hamiltonian points to the z direction: $\mathbf{d}_{0/\pi} = (0, 0, d^z_{0/\pi})$.

If the system is time reversal invariant as well (BDI symmetry class) $d_k^x \equiv 0$ and the topological number is the winding number similarly to the previous case. Because of PHS the winding of the angle of $\mathbf{d}_k$ is already determined in the $k \in (0, \pi)$ domain. That is, if the winding number is ν, the angle changes $\pi\nu$ while k goes through the positive half of the Brillouin zone. Therefore for a quench from ν_0 to ν_1 DPTs will appear with $\Delta\nu$ topologically protected timescales (Figure 2.11(b)). This result applies for the quantum XY chain of the previous section, and also for the transverse field Ising model studied in [68], as both of them can be mapped to Hamiltonians in the form of (2.32). The topological protection of DPTs for quenches connecting different phases was also revealed for the transverse field Ising chain [70, 120].

If TRS is broken (D symmetry class, [118]) $\mathbf{d}_k$ is not confined to a 2D plane. The $\mathbb{Z}_2$ invariant is 0 (topologically trivial) if $\hat{\mathbf{d}}_0 = \hat{\mathbf{d}}_\pi (= (0, 0, \pm 1))$ and it is 1 (nontrivial) if $\hat{\mathbf{d}}_0 = -\hat{\mathbf{d}}_\pi$. If the quench connects phases with different topology, e.g. $\nu_0 = 1$ and $\nu_1 = 0$, there must be a wavenumber k^* for which $\mathbf{d}^0_{k^*} \cdot \mathbf{d}^1_{k^*} = 0$ (illustrated on Figure 2.11(c)), because $\hat{\mathbf{d}}^0_0 \cdot \hat{\mathbf{d}}^1_0 = -\hat{\mathbf{d}}^0_\pi \cdot \hat{\mathbf{d}}^1_\pi = \pm 1$, hence $\hat{\mathbf{d}}^0_\mathbf{k} \cdot \hat{\mathbf{d}}^1_\mathbf{k}$ covers the interval $[-1, 1]$.

So far we have demonstrated that the change in topology under a sudden quench is an eligible condition for DPTs to occur. Note that $\mathbf{d}^0$ and $\mathbf{d}^1$ can become perpendicular *accidentally* even if the topological numbers do not differ in the initial and final Hamiltonians, as we have seen in the quantum XY chain. This parallels to the appearance of topologically non-protected edge or surface states in certain systems, whose existence is not connected to topology but is accidental [53, 121, 122].

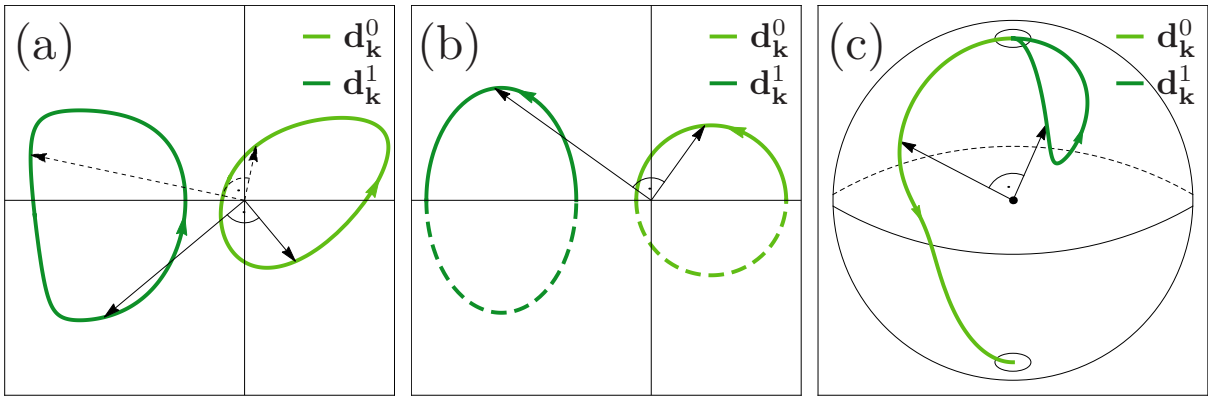

Figure 2.11: Illustration for the existence of perpendicular vectors if the quench connects domains with different topological numbers. (a) Topological insulators in AIII symmetry class. As k goes through the Brillouin zone $\mathbf{d}_k$ draws a closed loop. For any parametrization of these loops there will be at least $2\Delta\nu$ wavenumbers for which $\mathbf{d}^0 \perp \mathbf{d}^1$ if the winding number of the two vector fields differ by $\Delta\nu$. (b) Superconductors in BDI symmetry class. In the $k \in [0, \pi]$ domain (solid line) there will be at least $\Delta\nu$ perpendicular $\mathbf{d}$ vectors in a quench characterized by $\Delta\nu$. (c) Superconductors in D symmetry class. The vectors $\hat{\mathbf{d}}$ are no longer confined to a plane, but the occurrence of perpendicular vectors is still ensured when the topology of $\hat{\mathbf{d}}^1$ an $\hat{\mathbf{d}}^0$ are different.

2.3.2 Two dimensions

The topological number is the Chern number Q for 2-band topological insulators, which is calculated from the vector $\mathbf{d_k}$ defining the Hamiltonian [123],

$$Q = \frac{1}{4\pi}\int_{BZ} \mathrm{d}k_x \mathrm{d}k_y \; \hat{\mathbf{d}}_\mathbf{k} \cdot (\partial_{k_x}\hat{\mathbf{d}}_\mathbf{k} \times \partial_{k_y}\hat{\mathbf{d}}_\mathbf{k}) \tag{2.37}$$

counting how many times the surface defined by $\hat{\mathbf{d}}_\mathbf{k}$ covers the unit sphere. We show that if the quench connects phases with Chern numbers differing in their moduli, DPTs will necessarily occur. However, DPTs in 2D are qualitatively different from those in 1D, because of the Fisher zeros form areas instead of lines.

> If the Chern numbers of two vector fields $\mathbf{d}^0_\mathbf{k}$ and $\mathbf{d}^1_\mathbf{k}$ defined on the Brillouin zone (T^2) differ in the modulus $|Q_1| \neq |Q_0|$, the image of the scalar product field $\hat{\mathbf{d}}^0 \cdot \hat{\mathbf{d}}^1$ is $[-1, 1]$.

We prove our statement in four steps:
(a) If $\hat{\mathbf{d}}^0_\mathbf{k} \cdot \hat{\mathbf{d}}^1_\mathbf{k} > -1 \Rightarrow Q_1 = Q_0$, because there is a continuous mapping $\mathbf{f_k}(\gamma)$ between $\hat{\mathbf{d}}^0_\mathbf{k}$ and $\hat{\mathbf{d}}^1_\mathbf{k}$ such that $|\mathbf{f_k}(\gamma)| > 0$.

$$\mathbf{f_k}(\gamma) = (1-\gamma)\hat{\mathbf{d}}^0_\mathbf{k} + \gamma\hat{\mathbf{d}}^1_\mathbf{k}, \qquad \gamma \in [0,1]$$
$$|\mathbf{f_k}(\gamma)|^2 = 1 + 2\gamma(1-\gamma)(-1 + \hat{\mathbf{d}}^0_\mathbf{k} \cdot \hat{\mathbf{d}}^1_\mathbf{k}) > 0$$

The inequality in the second line came from the fact that $\gamma(1-\gamma) < 1/4$ for $\gamma \in [0,1]$. In other words if the vector fields $\hat{\mathbf{d}}^0_\mathbf{k}$ and $\hat{\mathbf{d}}^1_\mathbf{k}$ are nowhere antiparallel, then one can continuously deform one into the other. Under this deformation the Chern number does not change [124].
(b) If $Q_1 \neq Q_0 \Rightarrow \hat{\mathbf{d}}^0_\mathbf{k} \cdot \hat{\mathbf{d}}^1_\mathbf{k} = -1$ for some $\mathbf{k}$. This comes from reversing (a) and can be proved indirecly.
(c) If $Q_1 \neq -Q_0 \Rightarrow \hat{\mathbf{d}}^0_\mathbf{k} \cdot \hat{\mathbf{d}}^1_\mathbf{k} = 1$ for some (other) $\mathbf{k}$. We trace back this statement to (b) by defining the vector field $\hat{\mathbf{d}}'^1_\mathbf{k} \equiv -\hat{\mathbf{d}}^1_\mathbf{k}$, which satisfy $Q'_1 \neq Q_0$. Hence $\hat{\mathbf{d}}^0_k \cdot \hat{\mathbf{d}}'^1_\mathbf{k} = -1$ for some $\mathbf{k}$ implying (c). Supported by the continuity of $\hat{\mathbf{d}}^i_\mathbf{k}$ when the topology is well-defined, combining (b) and (c) finishes the proof.

This argument cannot be generalized to the $Q_1 = -Q_0$ case, a trivial counterexample is given by the quench $\mathbf{d}^1_\mathbf{k} = -\mathbf{d}^0_\mathbf{k}$, where the initial and final Chern numbers are the opposite, but $\mathbf{d}^0 \cdot \mathbf{d}^1 \equiv -1$.

The statement ensures that Fisher zeros connect $-\infty$ to ∞ if the modulus of the Chern number changes under the quench. Nevertheless, one might find Fisher lines connecting $-\infty$ to ∞ also when the modulus of the Chern numbers are the same. A 2D system can be thought of as a collection of 1D chains. If these 1D systems can be characterized by winding numbers, it is enough to find a pair of these 1D systems with differing winding numbers to see DPTs. On the other hand, Fisher zeros can also expand through the imaginary axis *accidentally* similarly to the 1D case.

In the superconducting case the product in Eq. (2.34) is taken for the half Brillouin zone. However, because of PHS one gets exactly the same contribution from the other half of Brillouin zone, so one can express $G(t)^2$ as a product over the whole BZ. From this the existence of DPTs follows for quenches connecting superconducting phases with different moduli of the Chern numbers.

2.3.3 Relation to entanglement dynamics

Our results on the mappings $\mathbf{d}_k^0 \cdot \mathbf{d}_k^1$ are important not only in the context of DPTs, but for the entanglement properties as well. Entanglement is a measure of non-local correlation in quantum states without reference to any observables [125]. The most common measure of the entanglement is the entanglement entropy, which is usually defined as the von Neumann or the Rényi entropy of the reduced density matrix for a particular bipartition of the system. Entanglement is a key notion in quantum information theory [11], and it is also used to characterize topologically ordered states [126] (which should not be confused with topological insulators), like quantum spin liquids or fractional quantum Hall states. The scaling of the entanglement entropy with system size also distinguishes between the eigenstates of many-body localized and ergodic phases, and the spreading of entanglement in a quench dynamics is also different in the two cases [33].

Another measure of the entanglement is the entanglement spectrum, that is, the spectrum of the reduced density matrix calculated for a physically relevant bipartition [127]. The time dependence of the entanglement spectrum has been studied in topological systems following a sudden quench in Refs. [128, 129]. Interestingly, the evolution of the entanglement spectrum shows a qualitative difference for quenches where $\mathbf{d}_k^0 \perp \mathbf{d}_k^1$ for some k, which is the very same condition that appeared in the context of DPTs. Further connections between DPTs and the entanglement spectrum is a subject of future research.

Now we illustrate the general results on some particular examples.

2.3.4 Example: Generalized SSH model

The SSH model is a 1D tight-binding chain that was originally introduced to model polyacetylene [130]. It is probably the simplest topological insulator, belonging to the BDI symmetry class [118]. The model is described by $\mathbf{d}_k = (t_0 + t_{-1}\cos(k), t_{-1}\sin(k), 0)$, where t_0 and t_{-1} are the staggered hopping amplitudes. The ground state is topologically trivial ($\nu = 0$) when $t_0 > t_{-1}$ and is non-trivial if $t_0 < t_{-1}$. The model can be extended to produce higher winding numbers by introducing longer ranged hopping terms that preserve chiral symmetry. The Hamiltonian in this case is characterized by the vector

$$\mathbf{d}_k = \sum_{m=0}^{\infty} \mathbf{d}_{m,k} = \sum_{m=0}^{\infty} (t'_m \cos(mk), t''_m \sin(mk), 0)\,, \tag{2.38}$$

where $t'_0 = t_0$, $t''_0 = 0$, $t'_m = t_m + t_{-m}$, $t''_m = t_{-m} - t_m$, and t_m is the real hopping amplitude between sublattices A in unit cell i and B in unit cell $i+m$, see Figure 2.12 for illustration. We note that in this labeling of the hopping amplitudes t_m and t_{-m-1} are independent and are responsible for the staggered nature of the system. Higher winding numbers can be produced by the proper choice of the hopping amplitudes, for example the winding number is $|\nu| = n \geq 1$ if t'_n and t''_n dominate the other hopping terms. An eligible condition for this is $\sum_{m=0}^{m\neq n} \max\{|t'_m|, |t''_m|\} < \min\{|t'_n|, |t''_n|\}$.

Proof. Let's consider first the limit when all other terms except from t'_n and t''_n are zero, then the winding number is clearly $\nu = n$. Now, by slowly turning on the other coefficients, the winding number cannot change as long as the gap does not close. As the excitation energy is given by the length of vector $\mathbf{d}_k$, the system is gapless if $||\mathbf{d}_k|| > 0$ for all k. The vector $\mathbf{d}_k$ is a sum of vectors $\mathbf{d}_{m,k}$ pointing in different directions depending

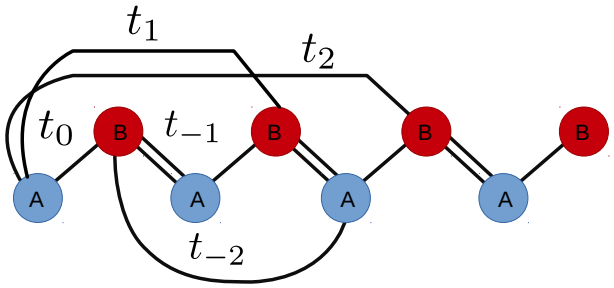

Figure 2.12: Generalized SSH model with long-range hopping terms. Chiral, or sublattice symmetry requires a bipartite structure, such that sites on sublattice A are only connected with sites on sublattice B.

on k, as written in Eq. (2.38). The n^{th} vector is the longest by assumption, and its norm is bounded from below as $||\mathbf{d}_{n,k}|| \geq \min\{t'_n, t''_n\}$. The upper bound for the norm of the other terms is $||\mathbf{d}_{m,k}|| \leq \max\{t'_m, t''_m\}$. If the longest vector is longer than the sum of the length of all other terms, then the sum of the vectors is guaranteed to have finite length, independently from their direction. More precisely, if $\sum_{m=0}^{m\neq n} \max\{|t'_m|, |t''_m|\} < \min\{|t'_n|, |t''_n|\}$, then $||\mathbf{d}_k|| = ||\sum \mathbf{d}_{m,k}|| \geq 0$ follows e.g. by applying the reverse triangular inequality.

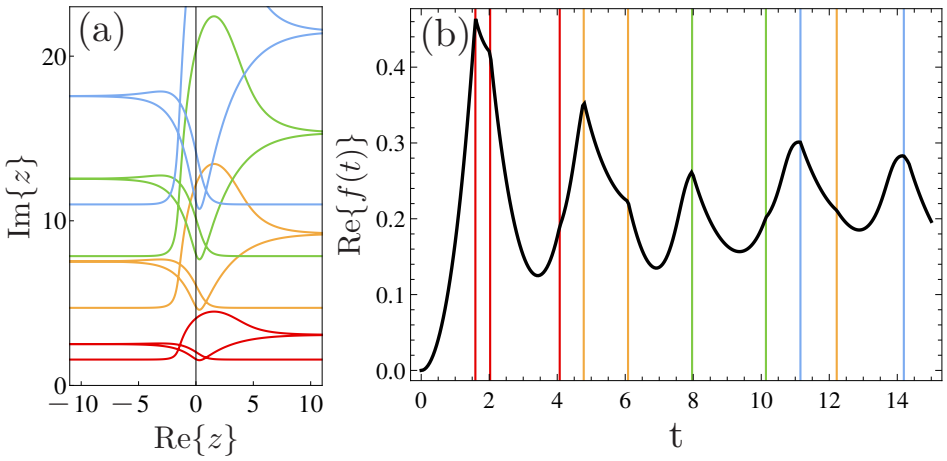

Figure 2.13: Fisher lines $z_n(k)$ (for $n = 0..3$) and DPTs in the generalized SSH model in a quench $\nu_0 = 1 \to \nu_1 = -2$. (a) The lines of Fisher zeros are doubly degenerate due to the $(k, -k)$ symmetry, they sweep through the real axis $|\Delta\nu| = 3$ times. (b) Dynamical phase transitions appear where the Fisher zeros cross the imaginary axis. The grid lines show the DPTs corresponding to the first four Fisher lines.

Besides the chiral symmetry this model has TRS as well. Therefore in a quench characterized by $\Delta\nu$, the $2\Delta\nu$ topologically protected $(-\infty, \infty)$ sections of the Fisher lines are pairwise degenerate (consider e.g. that $|\mathbf{d}^1_k| = |\mathbf{d}^1_{-k}|$ and $\mathbf{d}^0_k \cdot \mathbf{d}^1_k = \mathbf{d}^0_{-k} \cdot \mathbf{d}^1_{-k}$), implying only $\Delta\nu$ non-equilibrium timescales. The flow of the Fisher lines and the dynamical free energy are shown on Figure 2.13 for a quench from a phase with $\nu_0 = 1$ to $\nu_1 = -2$.

2.3.5 Example: The Haldane model

The Haldane model is a next-nearest neighbor hopping model on a honeycomb lattice with artificial magnetic field [56], which can produce topologically nontrivial states. The model is illustrated on Figure 2.14, which has been realized experimentally in cold atoms [46] and in photonic waveguides [47]. The Hamiltonian is characterized by the vector

$$\mathbf{d}_\mathbf{k} = (\mathrm{Re}\{g_1(k)\}, \mathrm{Im}\{g_1(k)\}, m - g_2^{\mathrm{asym}}(k,\phi))\,, \tag{2.39}$$

where $g_1(k) = \gamma_1 \sum_j e^{-i\mathbf{k}\boldsymbol{\delta}_j}$ and vectors $\boldsymbol{\delta}_j$ point to the three nearest neighbors. The mass term $m\sigma_z$ describes a homogeneous staggered lattice potential. The $-g_2^{\mathrm{asym}}(\mathbf{k},\phi)\sigma_z$ term comes from a second neighbor hopping considering the staggered magnetic field characterizing the Haldane model. This latter term is necessary to produce nontrivial topology in the model. The Chern number depends on the phase ϕ characterizing the magnetic field, on the next nearest hopping amplitude γ_2, and on the mass term. The Chern number is $Q = 0$ if $|m| > |3\sqrt{3}\gamma_2 \sin\phi|$, and $Q = \pm 1$ if $|m| < |3\sqrt{3}\gamma_2 \sin\phi|$ with the sign depending on ϕ and γ_2. The phase diagram of the model with the Chern numbers are show on Figure 2.14.

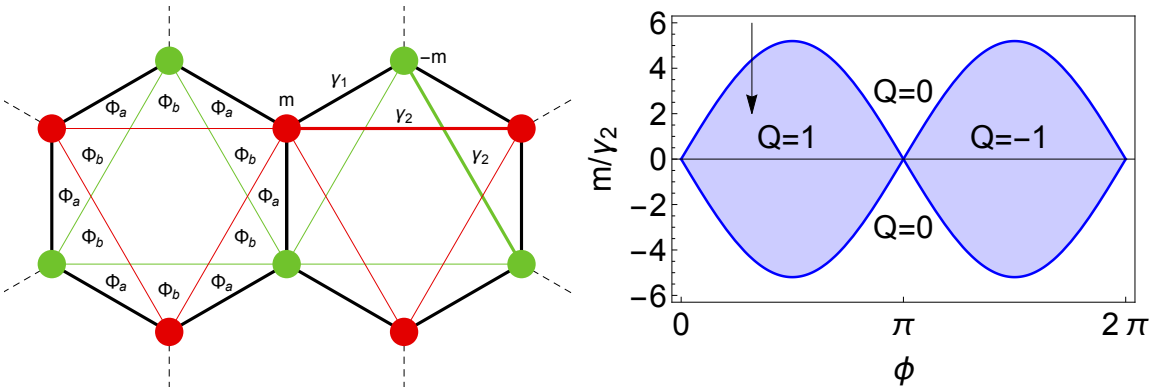

Figure 2.14: Illustration of the Haldane model and its phase diagram. A staggered magnetic field with zero net flux through a unit cell breaks the time reversal symmetry, and the next-nearest neighbor hopping terms (γ_2) acquire a phase $\phi = e/h2\pi(2\Phi_a + \Phi_b)$, while the nearest neighbor hopping terms (γ_1) are unaffected. The two inequivalent sublattices are characterized by on-site energies $\pm m$. The arrow on the phase diagram corresponds to the quench from $Q_0 = 0$ to $Q_1 = -1$ studied on Figure 2.15.

We have already proved that if the Chern number of the initial and final Hamiltonian differs, the Fisher zeros connect $-\infty$ with ∞. However, in contrast to the one dimensional case, in two dimensions the Fisher zeros fill areas rather than forming lines. Similar behaviour occurs for quenches in spin-glass systems [131, 132]. In our case the appearance of Fisher area is not unexpected, since each Fisher domain corresponding to a given n in Eq. (2.35) is parametrized by two variables k_x and k_y. As we have discussed in section 2.1.4, in contrast to Fisher lines, if a Fisher area crosses the imaginary axis, the dynamical free energy looks smooth and its first derivative shows cusps at the boundaries of the Fisher area (Figure 2.15(b)). The size of the jump of the second derivative is proportional to the density of zeros normalized by the system size (ρ) and with the cosine square of the impact angle (φ) of the boundary line, see Eq. (2.10). If the density

of the Fisher zeros diverges as $|y - y_0|^{-\alpha}$ at the boundary of the Fisher area, the slopes of the cusps in $\mathrm{Re}\{f'(t)\}$ inside the Fisher area diverge similarly. In the Haldane model this latter behavior occurs as shown in Figure 2.15.

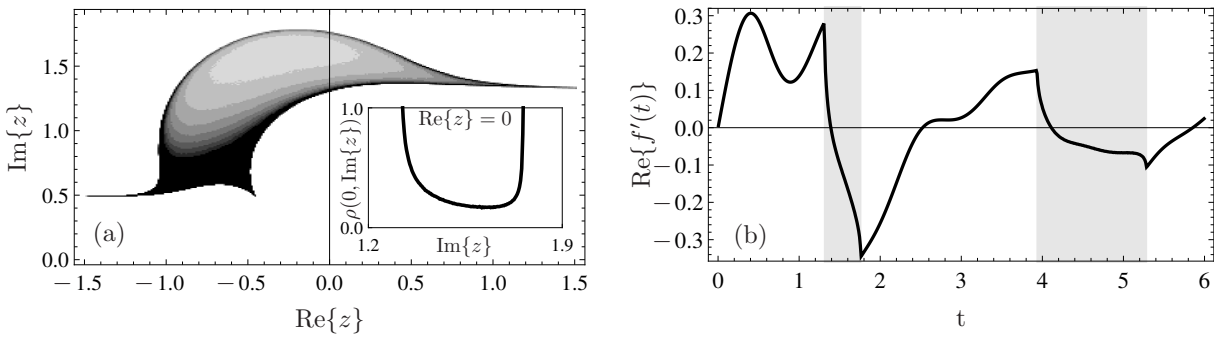

Figure 2.15: Quench in the Haldane model from $Q_0 = 0$ to $Q_1 = 1$. (a) Fisher zeros corresponding to $n = 0$ in Eq. (2.35). The normalized density of the Fisher zeros $\rho(\mathrm{Re}\{z\}, \mathrm{Im}\{z\})$ is shown as the darkness of the area. Inset: the density diverges on the imaginary axis at the boundary of the Fisher area. (b) Cusplike singularities in the first derivative of the dynamical free energy. The shaded areas emphasize the regions where the Fisher zeros cross the time axis.

These features are not specific to the Haldane model, but show up in a wide range of models, e.g. in the "half"-BHZ model [133], which is described by the vector $\mathbf{d_k} = (A \sin kx, A \sin ky, \Delta + \cos k_x + \cos k_y)$, or in the lattice version of the chiral topological $p + ip$ superconductor with similar $\mathbf{d_k}$ [134].

Our work triggered the experiments of Flaschner *et al* [93] to study the DPTs a Haldane-like model. They used ultracold atoms to realize the quench protocol. Their initial Hamiltonian is a static band insulator, but the topologically nontrivial Hamiltonian is generated by Floquet engineering. That is, they apply a high-frequency driving (shaking of the lattice), and the dynamics in stroboscopic times is governed by an effective static Hamiltonian, which exhibits bands with nonzero Chern numbers. This setup allows only stroboscopic measurements, and the singularities in the dynamical free energy cannot be resolved. However, they are able to measure Fisher zeros approaching the time axis. Their experimental apparatus allows them to realize time resolved state tomography, which is a momentum selective method to follow the evolution of the states on the Bloch sphere, for experimental data see Figure 2.16(c). If the north pole of the Bloch sphere is chosen to be the ground state of $H^0_{\mathbf{k}}$ for each $\mathbf{k}$ (Figure 2.16(b)), then a Fisher zero approaching the time axis is seen as there is a $\mathbf{k}$ for which the time evolved Bloch vector points to the south pole. This follows from the factorized form of the Loschmidt amplitude, which becomes zero if the time evolved state is orthogonal to the initial one for one momentum. In the 2D models with Fisher areas, there are time domains of finite length, where Fisher zeros approach the time axis, and there are states at the south pole, which is measurable. States appearing at the south pole translate into vortices in the azimuthal angle profile $\varphi_{\mathbf{k}}(t)$ on the Bloch sphere (Figure 2.16(d-g)). The measurement of these vortices is experimentally more robust, and their number is identified as a dynamical order parameter in Ref. [93].

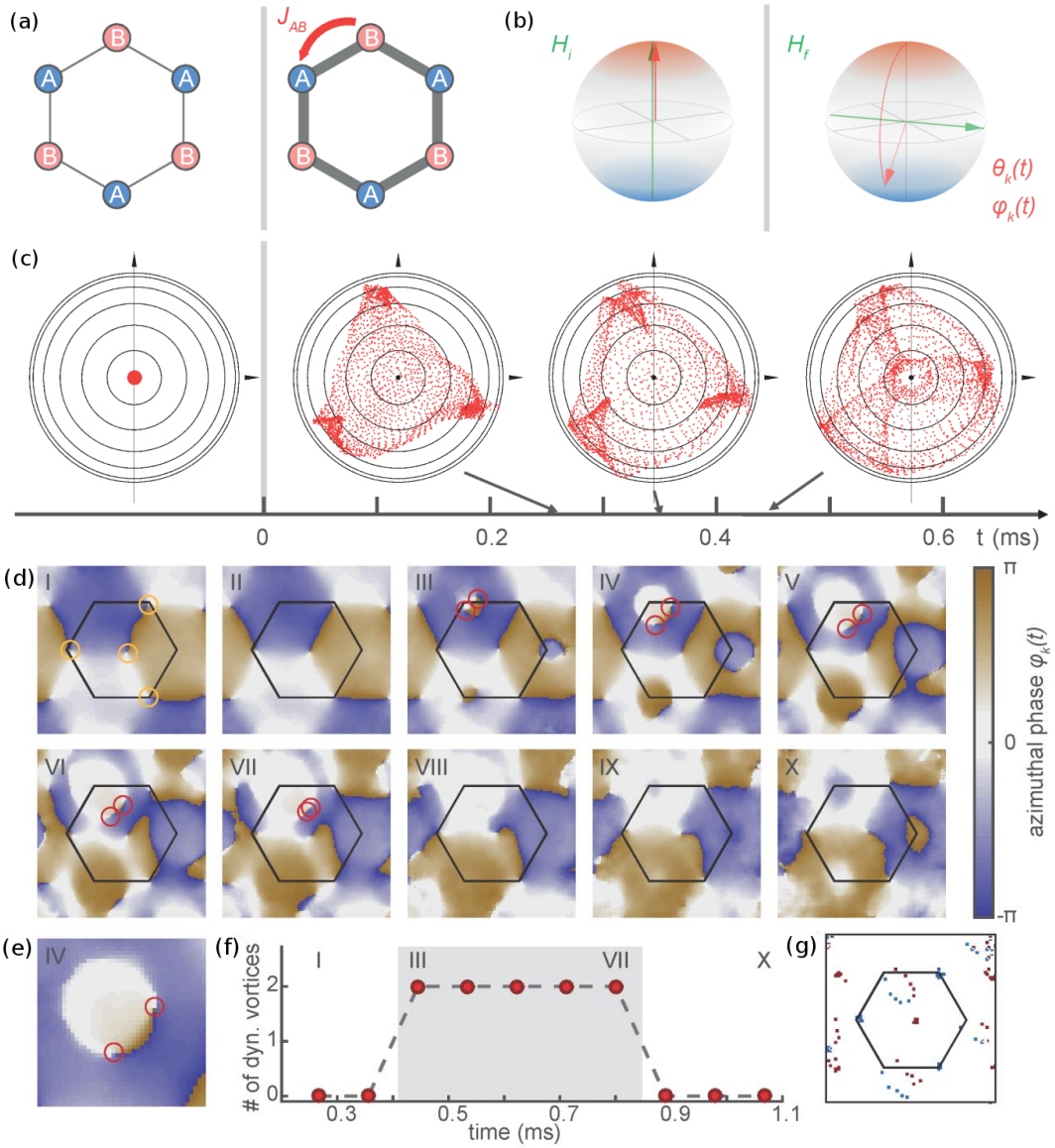

Figure 2.16: Experimental observation of DPTs. (a,b) The initial state is characterized by atoms localized on B sites, which corresponds to the north pole on the Bloch sphere for all $\mathbf{k}$. After the quench each state rotates around a momentum-dependent vector defined by the post-quench Hamiltonian $H_f(\mathbf{k})$. (c) The dynamics on the Bloch sphere can be experimentally monitored by the state tomography technique. (d,e) Dynamical vortices appear in the azimuthal angle profile $\varphi_\mathbf{k}$ when the south pole is reached for any $\mathbf{k}$, which also corresponds to Fisher zeros approaching the time axis. (f) The number of dynamical vortices as a function of time. (g) Path drown by the dynamical vortices. Panels (a-g) are adopted from Ref. [93].

2.3.6 Effect of disorder

Topology is a global property of systems, and is uniquely robust to local perturbations. For instance, topologically protected edge states, and edge currents cannot be destroyed by weak local perturbations. This topological protection underlies for example the exceptionally precise quantization of the conductivity of Quantum Hall edge states, that allowed it to serve as a basis of resistance standards in the past 15 years [135]. Although

we have shown that quenches connecting topologically distinct phases display DPTs, the proof assumed translational invariance, and it is not clear if disorder could wash away the cusps in the dynamical free energy. One could imagine a qualitative difference in the disordered case, because e.g. in 1D all eigenstates become localized by arbitrarily small disorder. In contrast, numerical simulations show that the dynamical free energy is not sensitive to disorder: the precise location of the cusps shift a little, but there is no signal of getting washed away by disorder, for illustration see Figure 2.17.

For simplicity let us focus on insulators, where the initial state is the entirely filled lower band, that is, in models with chiral symmetry, such as the SSH model, all states with negative energy are filled at zero temperature. This state on a chain of $2N$ lattice sites can be written as a Slater determinant, and the Loschmidt amplitude is expressed as

$$G(t) = \det\left[V_0^+ e^{-itH_1} V_0\right]_{1:N,1:N} \tag{2.40}$$

where the first and last N columns of V_0 are the negative and positive energy eigenvectors of H_0, respectively, and the subscript $1:N, 1:N$ refers to the upper-left corner of the $2N \times 2N$ matrix. In the translational invariant case this matrix is block-diagonal, and the determinant decomposes to a product of the determinants of the k-blocks, which allowed for the analytical expression for the Fisher zeros. In the disordered case finding the Fisher zeros is very difficult, even numerically.

The classifying global symmetries of the model (see section 1.4.1) have to be respected by the disorder, otherwise we substantially change the system and it leaves its original topological insulator phase. Particularly in the SSH model, on-site disorder is prohibited by the chiral symmetry, and we introduce disorder only in the nearest neighbor hopping terms t_0 and t_{-1}. The Hamiltonian becomes

$$H_{SSH} = \sum_{n=1}^{2N-1} t_{n,n+1} c_n^+ c_{n+1} + \text{h.c.} \tag{2.41}$$

with random hopping elements $t_{2n-1,2n} = t_0 + \xi_0(n)$ and $t_{2n,2n+1} = t_{-1} + \xi_{-1}(n)$, where $\xi_{0,-1}(n)$ are independent identically distributed random variables, with uniform distribution on $(-w, w)$. The dynamical free energy is then evaluated from Eq. (2.40) in a quench $(t_0^0, t_{-1}^0, w^0) \to (t_0^1, t_{-1}^1, w^1)$. Figure 2.17 shows that topologically protected DPTs are not washed away by the bond-disorder, and there are no qualitative differences between the translational invariant ($w = 0$) and disordered ($w > 0$) cases.

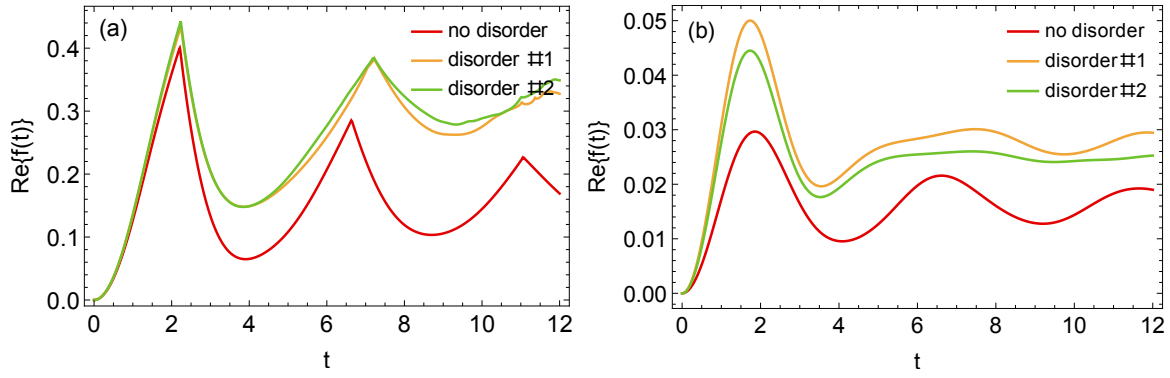

Figure 2.17: Comparison of the dynamical free energy with and without disorder in the SSH model on 800 lattice sites. (a) Parameters in the initial state are set to $t_0^0 = 1$, $t_{-1}^0 = 1.6$, and $t_0^1 = 1$, $t_{-1}^1 = 0.4$ in the final state, with uniform independent identically distributed bond-disorder $\xi_{0,-1}^{0,1} \in (-w, w)$ for both types of bonds in both the initial and final Hamiltonians, $w = 0.3$. (b) initial parameters: $t_0^0 = 1$, $t_{-1}^0 = 0.7$, final parameters: $t_0^0 = 1$, $t_1^0 = 0.4$, with the same disorder distribution as in (a).

2.4 Summary and outlook

Since the discovery of DPTs, much effort has been made to understand the details of this phenomenon. The first most important question was how generic DPTs are. Its robustness was verified by finding non-analytical dynamical free energy in a large variety of systems, which covers almost the entire spectrum of theoretical condensed matter physics: non-interacting and interacting spin and fermionic systems in 1 and 2 dimensions. Our contribution was to generalize DPTs to other models than just spin chains, and we were the first to show DPTs in higher than 1 dimensions. The occurrence of these transitions are related to the equilibrium phases of model with rigorous proofs for sufficient conditions for the occurrence of the non-analyticities. We found analytical counterexample to the conjecture that DPTs appear if and only if equilibrium phase boundary is crossed by the quench, and we also proved that in translation-invariant 2-band insulators and superconductors DPTs are guaranteed by topology if the quench connects topologically distinct phases. The dynamical free energy, or the Loschmidt amplitude are closely related to the work distribution of the quench protocol, which in principle is a measurable quantity, but an experimental demonstration of DPTs by measuring work distribution would be very challenging, as the relevant information is stored in the exponentially small tail of the distribution. Although DPTs have been found experimentally by state tomography in cold atomic systems, it is probably the most important perspective of research to find consequences of DPTs in other observables. It has been demonstrated that DPTs influence the dynamics of the order parameter starting from symmetry breaking initial conditions [75], and there is a proposal for generalized expectation values [74], which are non-analytic functions of time, however they also do not correspond to experimentally accessible observables. There might also be an interesting relation between the dynamics of quantum entanglement and DPTs [19], and we have preliminary results indicating that when DPTs appear, the single particle entanglement spectrum becomes gapless in the long-time limit, while if they are absent, it stays gapped, at least for 1D 2-band models.

3

Schwinger pair creation in Weyl semimetals

In this chapter we continue the analysis of time evolution following sudden quench protocols, but we change the focus from the Loschmidt amplitude to the *creation of particle-hole pairs* following an abrupt switching on of an external electric field. However, as a connection to the previous chapter, in section 3.5 we show that the vacuum persistence probability, a quantity closely related to the Loschmidt echo, provides a good measure for the pair creation rate.

As we briefly introduced in section 1.4.2, Weyl semimetals (WSMs) are 3D materials, which similarly to the 2D Dirac electrons in graphene, are characterized by linearly dispersing low energy excitations around some points in the Brillouin zone [136–139]. These Weyl points are intersections of nondegenerate bands, and are stable against perturbations according to their topological nature. In contrast to chapter 2, topology does not play a fundamental role in the time evolution other than being responsible for the existence of Weyl nodes.

Similar to clean graphene, when the Fermi energy in WSMs is near the Weyl point, there are no charge carriers available for transport at zero temperature, since the density of states vanishes as $\sim \epsilon^2$ close to the Weyl point. However, in an applied electric field, particle-hole pairs created by the Schwinger mechanism [140] contribute to transport.

The non-equilibrium state that evolves after turning on an electric field can be characterized by the statistics of the excitations, and by the induced current. As pair creation is described by the Landau-Zener (LZ) formula in the strong electric field regime, it is intrinsically related to the Kibble-Zurek (KZ) mechanism [141–143], which describes the universal scaling of defect generation in driven systems near a critical point, further discussed in section 3.1.1. Alas, KZ scaling gives only the mean number of excitations, and thus does not fully characterize the non-equilibrium state.

Such a characterization, however, is possible through all the higher moments or cumulants, as these contain all information about non-local correlations of arbitrary order and entanglement. This is practically equivalent to determining the full distribution function of the quantity of interest. Therefore, the full distribution function of the number of electron-hole pairs is also of importance, yielding additional information about the physics of Schwinger pair production. Condensed matter physics and cold atomic systems thus provide a unique way to experimentally detect such quantities [144, 145], beyond the current capabilities of high energy physics. These ideas also relate to the discipline of full

counting statistics [146, 147], where outstanding experiments measure whole distribution functions [148, 149], and cumulants up to the 15th order e.g. in Ref. [150].

Our results on the time evolution of the current and statistics of electron-hole pairs are summarized in Table 3.1. The time domain is split into three distinct regions with different behaviour, which we call classical (ultrashort), Kubo (short), and Landau-Zener regime (long perturbations).

Time domain	Classical $t \ll \frac{\hbar}{v_F\Lambda}$	Kubo $\frac{\hbar}{v_F\Lambda} \ll t \ll \sqrt{\frac{\hbar}{v_F eE}}$	Landau-Zener $\sqrt{\frac{\hbar}{v_F eE}} \ll t$
# pairs (n)	$\sim E^2t^2\Lambda$	$\sim E^2t$	$\sim E^2t$
Statistics	Poissonian	Poissonian	Gaussian-like
Current (j)	$\sim Et\Lambda^2$	$\sim E/t$	$\sim E^2t$

Table 3.1: The electric field and time dependence of the total number of excitations or pairs created (n) and its statistics, together with the electric current (j) is shown. Λ is the momentum cutoff, E is the electric field.

The time evolution of the current also allows us to conjecture qualitatively the behaviour of the steady state current-voltage characteristics. For small voltages, the dynamical calculation combined with a generalized Drude theory reproduces the results of Kubo formula calculations, i.e. the current is proportional to the electric field. However, Ohm's law breaks down for larger voltages and the current-electric field dependence becomes non-linear. This critical electric field as well as the non-linear current-voltage relation are important for possible transport experiments in WSMs.

3.1 Electric field switch-on in a Weyl semimetal

We perform a sudden global quench in the electric field, that is, we switch on a homogeneous electric field E at time $t = 0$. Instead of following the lines of the previous chapter to study the post-quench time evolution, here it is more convenient to map the quench in the electric field to a ramp protocol in the vector potential, because the latter treatment preserves translational invariance. We consider noninteracting Weyl fermions near a single Weyl point. The time dependent vector potential describing the quench in the electric field is simply given by $\mathbf{A}(t) = (eEt\Theta(t), 0, 0)$. The time evolution of a given mode $\mathbf{p} = (p_x, p_y, p_z)$ is then governed by the Hamiltonian

$$H = v_F(\mathbf{p} - e\mathbf{A}(t)) \cdot \boldsymbol{\sigma}\,, \tag{3.1}$$

where $\boldsymbol{\sigma}$ denotes the vector of Pauli matrices and v_F is the Fermi velocity. The spectrum consists of two bands as $\pm v_F\sqrt{p_x^2 + p_\perp^2}$, with $p_\perp = \sqrt{p_y^2 + p_z^2}$ the perpendicular momentum. Initially ($t < 0$), the system is assumed to be in the $T = 0$ vacuum state, with all modes with negative single particle energy filled and positive energy modes empty. This effective Weyl theory is valid at low energies compared to a high energy cutoff $v_F\Lambda$ introduced for integrals over momentum space whenever necessary.

3.1.1 Landau-Zener problem and the Kibble-Zurek mechanism

At $t = 0$, the electric field is switched on, and the time dependent Schrödinger equation defines the famous Landau-Zener problem, illustrated on Figure 3.1. Each momentum $\mathbf{p}$

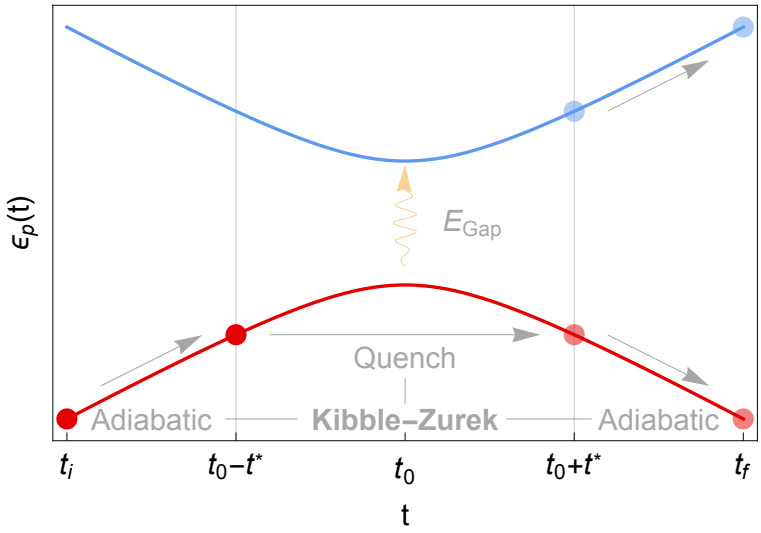

Figure 3.1: Illustration of the Landau Zener problem and the Kibble-Zurek mechanism. When a two level system initially prepared in the ground state is driven across an avoided crossing, the driving induces transition to the excited state with a probability depending on the minimal separation of the energy levels and on the speed of the driving. When the gap is large compared to the rate of change of the Hamiltonian, $\epsilon_{\mathbf{p}}(t) \gg \hbar\dot{\epsilon}_{\mathbf{p}}(t)/\epsilon_{\mathbf{p}}(t)$, the dynamics is near adiabatic. In the opposite limit the system cannot follow the external perturbation, which is approximated by a sudden quench in the KZ mechanism. The excitations created in the middle region freeze out and evolve adiabatically after leaving the avoided crossing behind.

acts as a two-level system, which is driven through an avoided crossing. If the driving were adiabatic, no transitions would occur to the upper band, but any finite electric field generates excitations. Landau and Zener studied the transition probability of two-level systems following a linear ramp across an avoided crossing. They found a simple analytical expression for the transition probability with a sweep starting at $t_i = -\infty$ and ending at $t_f = \infty$:

$$P_{ex} = \exp\left(-\pi \frac{E_{\mathrm{Gap}}^2}{4\hbar v_{\mathrm{driv}}}\right) = \exp\left(-\pi \frac{v_F p_\perp^2}{\hbar e E}\right) \tag{3.2}$$

where $E_{\mathrm{Gap}} = 2v_F p_\perp$ is the minimum value of the gap at the avoided crossing, and $v_{\mathrm{driv}} = v_F eE$ is the velocity of the sweep. For quick sweeps the excitation probability is well approximated by the Kibble-Zurek mechanism, which was originally developed to describe defect generation in classical phase transitions [151, 152], but later it was extended to quantum phase transitions [142], and to the Landau-Zener transition as a minimal model [143, 153]. The basic idea of the KZ mechanism is that as long as the gap is large, excitations are suppressed, and the time evolved state remains close to the adiabatically evolved state. However, the reaction time of systems near a quantum phase transition diverges due to the vanishing gap, which phenomenon is known as the *critical slowing down*. Consequently, the systems cannot follow the perturbation: the adiabatic

regime breaks down and defects are generated. This picture still holds when there is a small band gap E_{Gap}, but the driving is quick. After sweeping through the transition point, or the avoided crossing, the gap increases, which brings the system back to the adiabatic regime, where no new defects are generated, but those that are already present freeze into the adiabatically evolving state. The middle region, where the system cannot follow the change of the Hamiltonian, is approximated by a quench in the KZ mechanism. The only remaining question is at which time instant t^* the crossover from adiabatic to diabatic dynamics occurs. This is heuristically estimated from the timescales characterizing the Hamiltonian. The reaction timescale $\tau = \frac{\hbar}{\epsilon_{\mathbf{p}}(t)}$ of the system is given by the inverse of the instantaneous gap

$$\epsilon_{\mathbf{p}}(t) = v_F \sqrt{(p_x - eA(t))^2 + p_\perp^2}\,, \tag{3.3}$$

while the timescale characterizing the swiftness of the quench is given by $\tau_Q = \frac{\epsilon_{\mathbf{p}}(t)}{\dot{\epsilon}_{\mathbf{p}}(t)}$. The crossover time is estimated as $\tau(t^*) = \tau_Q(t^*)$, and for convenience we measure t^* from the time reaching the avoided crossing. This constraint sets $t^* = t_E = \sqrt{\hbar/v_F eE}$ in the strong electric field regime, where t_E is the timescale related to the electric field. The associated correlation length, which also gives the scaling of the separation of defects is $\xi^* = v_F \tau(t^*) \approx v_F t^* = \sqrt{\hbar v_F/eE}$. The power of the KZ scaling is that the crossover time and the correlation length are universal functions of the velocity. For generic quantum phase transitions they are given by $t^* \sim v_{\mathrm{driv}}^{-z\nu/(z\nu+1)}$ and $\xi^* \sim v_{\mathrm{driv}}^{-\nu/(z\nu+1)}$, where the exponents ν, z characterize the quantum critical point [1], and v_{driv} characterizes the speed of the ramp protocol. The $\nu = z = 1$ exponents of the transverse field Ising model reproduce the estimates for the LZ dynamics [154]. From these general considerations, the density of the particle-hole excitations can be readily estimated. For any fixed p_x, the resulting 2(+1)D system exhibits $n_{ex,2D} \sim (\xi^*)^{-2} \sim eE/\hbar v_F$ excitations, and because of only momenta with $0 < p_x < eEt$ are driven across an avoided crossing, the total density of excitations scale as $n_{ex} \sim \frac{(eE)^2 t}{\hbar^2 v_F}$, agreeing with the outcome of a more elaborate calculation, Eq. (3.26).

The Landau-Zener solution is a valid approximation only if the dynamics describes a complete crossing, that is, if t_i and t_f fall into the adiabatic regime. In the 3D system we are considering, this constraint also depends on the value of p_x, which we have taken into account in the KZ estimate for the particle-hole density. Shortly after switching on the electric field, the number of complete crossings is negligible, while at later times they become responsible for the main contribution to the excitations. In the following we will consider the complete time evolution starting from short to long times. Although the Landau-Zener problem can be solved analytically using parabolic cylinder functions [155–157] for any finite values of t_i and t_f, the general formula is very complicated, and it hides the interesting physics behind the problem. Instead, we proceed with applying various approximations to the excitation number: we use a perturbative solution at short times and the Landau-Zener formula at large times. These provide transparent results for the emerging current and the statistics of excitations in the vicinity of a Weyl node, which we also compare with numerical calculations.

3.1.2 Landau-Zener dynamics and the induced current

It is convenient to work in the adiabatic basis, which is the time-dependent basis diagonalizing the instantaneous Hamiltonian. This, following the derivation in Refs. [158, 159], is achieved by a two-step unitary transformation $U = U_s U_d$. First, we apply a static rotation U_s around the x axis such that the new y' axis points in the direction of $\mathbf{p}_\perp = (0, p_y, p_z)$. Then we diagonalize the Hamiltonian with the dynamical $U_d = \exp(-i\delta(t)\sigma_z/2)(\sigma_x+\sigma_z)$, where $\tan\delta(t) = \frac{p_\perp}{p_x - eEt}$. The time dependent Schrödinger equation in the adiabatic basis reads as

$$i\hbar\partial_t \Phi_{\mathbf{p}}(t) = H'\Phi_{\mathbf{p}}(t) \tag{3.4}$$

$$H' = \sigma_z \epsilon_{\mathbf{p}}(t) - \sigma_x \frac{\hbar v_F^2 eEp_\perp}{2\epsilon_{\mathbf{p}}^2(t)}\,, \tag{3.5}$$

with the initial condition $\Phi_{\mathbf{p}}(0) = (0,1)^T$ corresponding to the fully occupied lower band. The wavefunction in the original basis is given by $U\Phi_{\mathbf{p}}$. The instantaneous eigenenergies form two bands as $\pm\epsilon_{\mathbf{p}}(t)$ with $\epsilon_{\mathbf{p}}(t)$ defined in Eq. (3.3). The pair creation is generated by the offdiagonal term $\sim \sigma_x$. By denoting the solution of Eq. (3.4) by $\Phi_{\mathbf{p}}(t) = (a_{\mathbf{p}}(t), b_{\mathbf{p}}(t))$, the mode excitation probability $n_{\mathbf{p}}(t) = |a_{\mathbf{p}}|^2$, which gives the number of electrons created in the upper band due to the electric field and also the holes in the lower band. The current operator in the original basis is $j_x = -ev_F\sigma_x$, which transforms into $j_x = -ev_F(\sigma_z\cos\delta + \sigma_y\sin\delta)$ in the adiabatic basis. This formula distinguishes between the conduction (intraband, $\sim\sigma_z$) and the polarization (interband, $\sim\sigma_y$) parts of the current. The current contribution $\langle j_x\rangle_{\mathbf{p}}(t) = j^{\mathrm{c}}_{\mathbf{p}}(t) + j^{\mathrm{p}}_{\mathbf{p}}(t)$ from a given mode $\mathbf{p}$ is determined by the mode excitation probability $n_{\mathbf{p}}(t)$, with the observation that $\mathrm{Re}\{iab^*\} = -\frac{\epsilon_{\mathbf{p}}^2}{v_F p_y eE}\partial_t n_{\mathbf{p}}(t)$ [158, 159],

$$j^{\mathrm{c}}_{\mathbf{p}}(t) = -ev_F\left[\frac{v_F(p_x - eEt)}{\epsilon_{\mathbf{p}}(t)}(2n_{\mathbf{p}}(t)-1)\right], \tag{3.6}$$

$$j^{\mathrm{p}}_{\mathbf{p}}(t) = ev_F\frac{2\epsilon_{\mathbf{p}}(t)}{v_F eE}\partial_t n_{\mathbf{p}}(t)\,. \tag{3.7}$$

The total contribution of a Weyl node is obtained after momentum integration. In Eq. (3.6), the $n_{\mathbf{p}}$ independent background is discarded, as an empty or fully occupied band does not carry current [158, 160]. In our non-interacting model, the total current, excitation numbers and higher cumulants are additive, i.e. given by the sum over the Weyl nodes.

The vanishing gap is a signature of the "criticality" of the WSM phase. As such, it exhibits scaling properties, which allow us to deduce important properties of the system without explicitly solving the Schrödinger equation. The excitation probability of the modes satisfies a scaling relation (in units of $\hbar, v_F, e = 1$),

$$n^E_{\mathbf{p}}(t) = n^{b^2E}_{b\mathbf{p}}(b^{-1}t)\,, \tag{3.8}$$

which follows from the time dependent Schrödinger equation, and holds for any choice of the dimensionless scaling parameter b. The invariants of the scaling transformation yield the natural dimensionless combinations which determine the physics e.g. $\frac{p}{eEt}$, $\sqrt{\frac{v_F}{\hbar eE}}p$, $\tilde{t} = \sqrt{\frac{v_F eE}{\hbar}}t$, etc. The dimensionless time $\tilde{t} = \frac{t}{t_E}$ uniquely classifies the excitation probability

as a function of $\mathbf{p}$. Time reversal considerations also give constraint on the excitation probabilities [157]

$$n_{\mathbf{p}}(t) = n_{e\mathbf{E}t-\mathbf{p}}(t)\,, \tag{3.9}$$

which means that the excitation probability is symmetric with respect to $p_x = \frac{1}{2}eEt$, which is also apparent in the numerical solutions in Figs. 3.2 and 3.3. Accordingly, in Eq. (3.11), and everywhere where spherical coordinates are used, the momentum is measured from $(eEt/2, 0, 0)$. That is, $p = \sqrt{(p_x - eEt/2)^2 + p_\perp^2}$. At time t momenta $\mathbf{p}$ and $e\mathbf{E}t - \mathbf{p}$ are related by the fact that they share the same ratio of level crossing in the Landau-Zener transition. For example in the particular case of $p_x = 0$ and $p_x = eEt$ there is only a half-crossing [156], that is, the particles are not driven through the gap minimum, but the drive either starts or finishes there, respectively. To be more precise, the symmetry (3.9) originates in the following symmetry of the Hamilton operator: $H_{e\mathbf{E}t'-\mathbf{p}}(t) = -H_{\mathbf{p}}(t'-t)$, and $H'_{e\mathbf{E}t'-\mathbf{p}}(t) = H'_{\mathbf{p}}(t'-t)$ in the adiabatic basis. The time evolution operator in the adiabatic basis is $\mathcal{U}_{\mathbf{p}}(t,0) = \mathcal{T}e^{-\frac{i}{\hbar}\int_0^t H'_{\mathbf{p}}(s)\mathrm{d}s}$, and applying the above symmetry transformation yields

$$\mathcal{U}_{e\mathbf{E}t-\mathbf{p}}(t,0) = \mathcal{A}e^{-\frac{i}{\hbar}\int_0^t H'_{\mathbf{p}}(s)\mathrm{d}s} = \mathcal{K}\mathcal{U}^+_{\mathbf{p}}(t,0)\mathcal{K}\,, \tag{3.10}$$

where $(\mathcal{A})\mathcal{T}$ is the (anti) time-ordering operator, and $\mathcal{K}$ is complex conjugation. From this Eq. (3.9) follows.

The excitation probability as a function of p is qualitatively different in the $\tilde{t} \gg 1$ and $\tilde{t} \ll 1$ cases (Figs. 3.2,3.3).

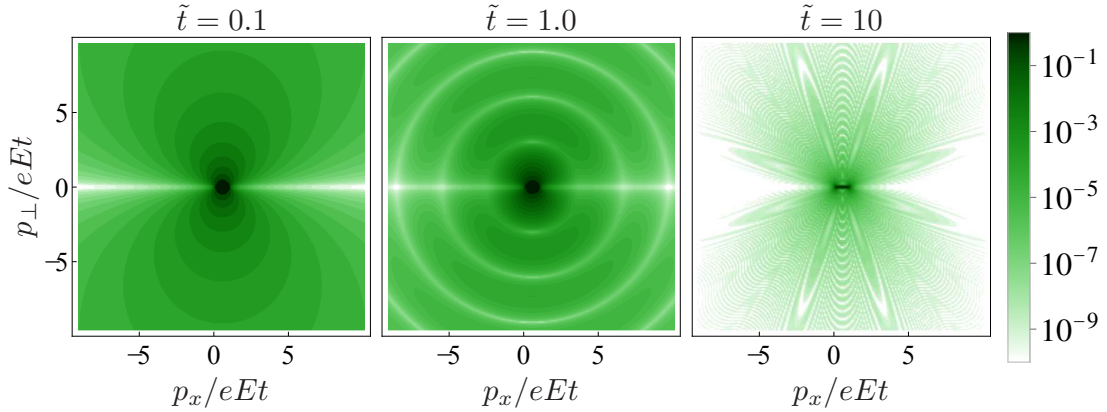

Figure 3.2: Excitation probabilities in momentum space for short (left), intermediate (middle) and long (right) perturbations. While at short times ($\tilde{t} \ll 1$) there are many excitations with large momenta, with increasing time the excitations are more and more confined to momenta $p \leq eEt$. Note the logarithmic scale on the colorbar.

A perturbative solution valid for $\tilde{t} \ll 1$ is [158]

$$n_{\mathbf{p}} = \frac{(eE\hbar p_\perp)^2}{4v_F^2 p^6} \sin^2\left(\frac{v_F p t}{\hbar}\right)\,. \tag{3.11}$$

This gives a good approximation for the excitation number for $p \gg eEt$. At short times high energy states may become excited, which is reflected in the power law decay of excitations as a function of momentum ($\sim p^{-2}$ for $p \ll \hbar/v_F t$).

If the perturbation is long, the probability of exciting a given mode is well approximated by the LZ solution [161],

$$n_{\mathbf{p}} = \Theta(p_x)\Theta(eEt - p_x) \exp\left(-\frac{\pi v_F p_\perp^2}{\hbar e E}\right). \tag{3.12}$$

This describes a "dynamical steady state", which is characterized by a longitudinally growing cylinder of excited states of length eEt and radius $\sim \sqrt{\frac{\hbar eE}{\pi v_F}}$. In contrast to the short time limit, the excitation probability decays exponentially for large momentum. This exponential decay can be explained as a tunneling effect within the WKB approach [162].

Along with the analytical calculations, for comparison, we determine numerically $n_{\mathbf{p}}$ and $\partial_t n_{\mathbf{p}}$ by applying an explicit Runge-Kutta method [163] to solve the time dependent Schrödinger equation. In Figure 3.3 we compare the approximations used for $n_{\mathbf{p}}$ with the numerically obtained values.

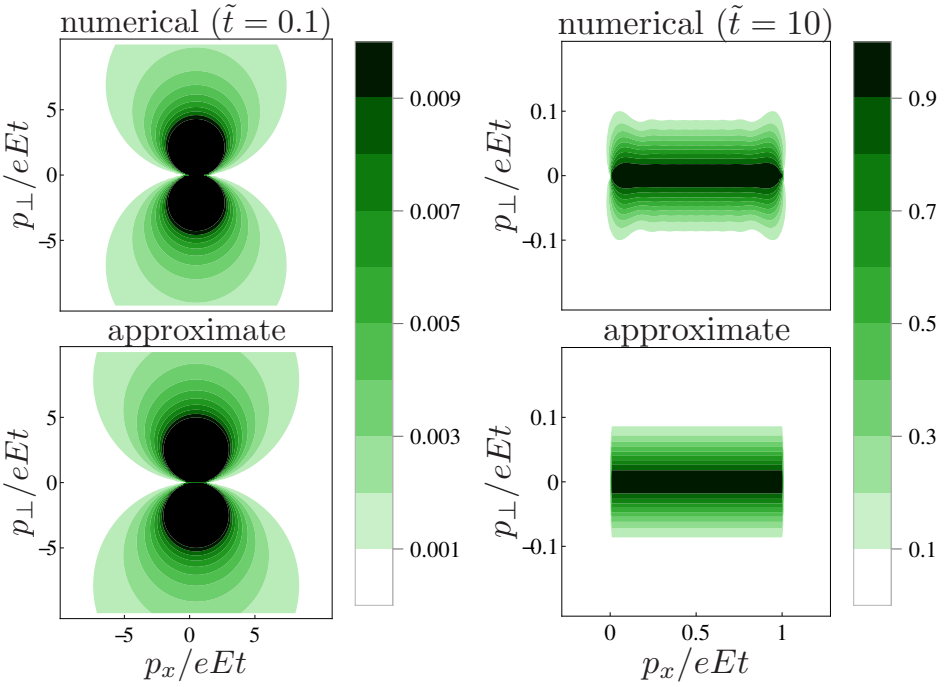

Figure 3.3: Comparison of the numerical and approximate excitation probabilities for short (left) and long perturbations (right). The excitation map has a "dipolar" character for short times, and the approximate formula (3.11) is nearly indistinguishable from the numerical solution for $p \gg eEt$. The excitation map is cylindrical for long times. An (asymptotically irrelevant) increased number of excitations at $p_x = 0$ and $p_x = eEt$ is not captured in the approximation (3.12).

3.2 Evolution of the current

We are now in a position to discuss the time evolution of the current. The high energy cutoff, $v_F\Lambda$ defines an ultrashort timescale $t_\Lambda = \frac{\hbar}{v_F\Lambda}$, which satisfies $t_\Lambda \ll t_E$ for both

condensed matter [137] and cold atomic [145] realizations of WSMs, similarly to the 2D case [144]. The scaling property (3.8) implies a scaling for the integrated current as

$$j^{\mathrm{c/p}}_{E,\Lambda}(t) = b^{-3} j^{\mathrm{c/p}}_{b^2 E, b\Lambda}(b^{-1}t)\,. \tag{3.13}$$

The particular choice of $b = t_E$ allows us to reveal the electric field and time dependence of the physical quantities. The current is expressed as $j^{\mathrm{c/p}}_{E,\Lambda}(t) = E^{3/2} j^{\mathrm{c/p}}_{1,t_\Lambda/t_E}(t/t_E)$. The scaling functions $j^{\mathrm{c/p}}_{1,y}(x)$ are determined from Eqs. (3.6,3.7) after evaluating the momentum integrals with the particular form of $n_{\mathbf{p}}(t)$,

$$j^{\mathrm{c}}_{E,\Lambda}(t) \sim E^{3/2} \begin{cases} -\left(\frac{t}{t_E}\right)^3 \ln \frac{t\, t_\Lambda}{t_E^2} & t \ll t_\Lambda \\ -\left(\frac{t}{t_E}\right)^3 \ln \frac{t}{t_E} & t_\Lambda \ll t \ll t_E \\ \frac{t}{t_E} & t_E \ll t \end{cases} \tag{3.14}$$

$$j^{\mathrm{p}}_{E,\Lambda}(t) \sim E^{3/2} \begin{cases} \frac{t\, t_E}{t_\Lambda^2} & t \ll t_\Lambda \\ (1 + \text{non-univ.}) \frac{t_E}{t} & t_\Lambda \ll t \ll t_E \\ \text{const} & t_E \ll t \end{cases} \tag{3.15}$$

The term "non-univ." in the second line of Eq. (3.15) denotes the non-universal contribution from the high energy regularization, which dies out with increasing time, as discussed further in Eq. (3.17).

For $t \ll t_E$ the current is dominated by the polarization part. Because of the large weight of high energy states available to excite at ultrashort times $t < t_\Lambda$, the current is determined by the cutoff. The ultrashort time contribution of a Weyl point to the current is linear in time,

$$j(t) = \frac{1}{6\pi^2} \frac{e v_F}{\hbar^3} e E t \Lambda^2\,. \tag{3.16}$$

This behavior has also been observed for 2D Dirac fermions [158], and can be explained using a classical picture of particles with effective mass $m^{-1}_{i,j} = \frac{\partial^2 \epsilon_{\mathbf{p}}}{\partial p_i \partial p_j}$ accelerating in an external field satisfying Newton's equation. In 2D, the current saturates at $t \sim t_\Lambda$, and remains constant until $t \sim t_E$. In 3D the behavior is sharply different as the current starts to decay as t^{-1} after reaching a maximal value at $t \sim t_\Lambda$. The precise form of the decay depends on the microscopic details (i.e. on the cutoff), but the exponent is a universal characteristic of Weyl physics. Imposing a sharp cutoff results in an oscillating current $j \sim t^{-1}(1 + \cos(t/t_\Lambda))$, also obtained within linear response [164]. A smooth (exponential or Gaussian) cutoff of the form $\exp(-\sqrt{2}p/\Lambda)$ or $\exp(-p^2/\Lambda^2)$ does not generate the oscillating part, and gives

$$j(t) = \frac{1}{6\pi^2} \frac{e^2 E}{\hbar v_F t} F(t/t_\Lambda)\,, \tag{3.17}$$

where $F(y) = \frac{y^2}{2y^2+1}$ when the exponential and $F(y) = \int_0^\infty \mathrm{d}x\, e^{-x^2/y^2} \sin 2x$ when the Gaussian cutoff is used, both of which show the same limiting behaviour $F(y) \sim y^2$ for $y \ll 1$ and $F(y) = 1/2$ for $y \gg 1$. The qualitative difference between the 2D and 3D cases

is a consequence of their respective phase space sizes. The polarization current is a sum of contributions with oscillating signs $j \sim \int \mathrm{d}p \, \sin(2pt) p^{d-3}$, which, by simple scaling, results in a time independent contribution in 2D, but decays as t^{-1} in 3D.

The conduction part overtakes the polarization term at $t \sim t_E$, beyond which the current increases linearly with time and nonlinearly with electric field as

$$j(t) = \frac{1}{4\pi^3} \frac{e^3 E^2}{\hbar^2} t \,. \tag{3.18}$$

This is simply the number of charge carriers per unit volume in the steady-state cylinder multiplied by ev_F. It is beyond linear response, as it depends quadratically on the external field [159]. Our analytical predictions for the current are illustrated on Figure 3.4, together with the numerical results.

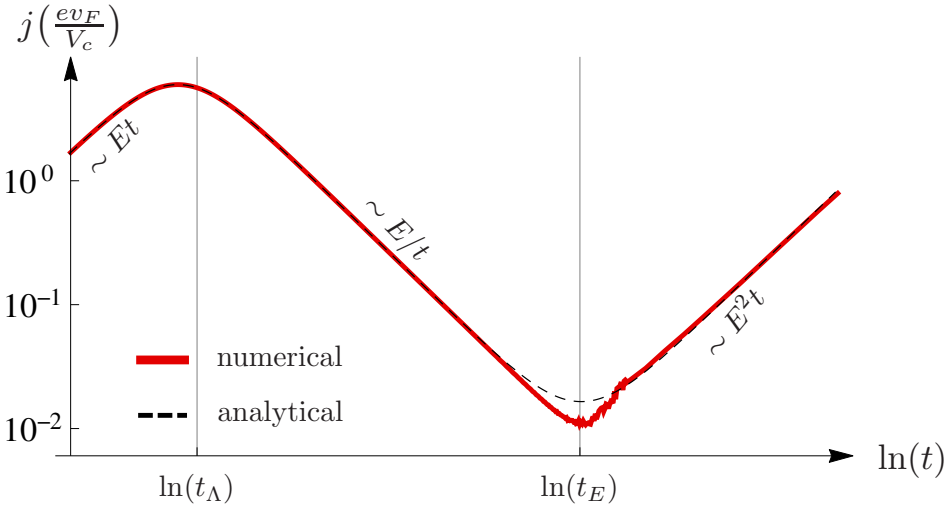

Figure 3.4: Time evolution of the total current after switching on an electric field. The analytical curve is the sum of polarization current (3.17), dominant for $t \ll t_E$, and conduction current (3.18), dominant for $t \gg t_E$. The evolution of the number of pairs, κ_1, is shown in Figure 3.5.

Bloch oscillations appear on a timescale $t_{\mathrm{Bloch}} \sim \frac{\hbar}{eEa}$, where a is the lattice constant, and our description holds for $t \ll t_{\mathrm{Bloch}}$. The timescale related to the cutoff is non-universal, and both t_E and t_{Bloch} depend on the applied field. These three scales are in fact not independent, which can be seen in the following way. The momentum cutoff is proportional to the largest momentum in the system $\Lambda = \frac{1}{c}\frac{\hbar}{a}$, which relates the timescales as $t_\Lambda t_{\mathrm{Bloch}} = c\, t_E^2$, where $c > 1$ is a system dependent constant describing the ratio of the linear size of the Brillouin zone and the validity range of Weyl physics. This also implies that in the experimentally relevant $t_\Lambda \ll t_E$ case, $t_E \ll t_{\mathrm{Bloch}}$ is also satisfied, and all three regions appear before Bloch oscillations set in. Λ is also limited by the separation of the closest Weyl points in the Brillouin-zone. If two Weyl points lie close to each other, it limits the domain of applicability of our method through the parameter c. If $c \gg 1$, the Weyl physics describes only a small fraction of the Brillouin zone, and the contribution of the remaining parts can be large in the ultrashort perturbation limit. For intermediate and long perturbations, the cutoff does not play an important role, and the Weyl contribution dominates the total current and the excitation number. The results of a single Landau-Zener transition break down when the excitations are driven through another Weyl point.

The timescale when it happens is given by $\frac{\Lambda}{eE} = \frac{1}{c} t_{\mathrm{Bloch}}$ for an electric field pointing in the direction along which the two closest Weyl nodes are aligned, and it varies with the angle. To describe the behaviour at $t \gg t_{\mathrm{Bloch}}$, one needs to go beyond the continuum description of Eq. (3.1) and consider the full lattice model, as was done for graphene in Ref. [165].

It is interesting to note that the maximal current is $j_{max} \sim e^2 v_F E\Lambda/\hbar^3$, which the system reaches upon leaving the classical region during the time evolution. Even in the nonlinear region in Eq. (3.18), the maximal current falls to the same order of magnitude, which is in sharp contrast to 2D Dirac semimetals, where the non-linear current strongly exceeds the current from the classical region.

As the external field induces current, it also injects energy into the system. The conduction and the polarization current decompose the total pumped energy into reversible ("work") and irreversible ("heat"), as follows. An infinitesimal change in the energy can be written as $\mathrm{d}E = \sum_i (\mathrm{d}\epsilon_i n_i + \epsilon_i \mathrm{d}n_i)$, where $i = (\mathbf{p}, \pm)$ runs over all momenta of the two bands. The first term corresponds to the reversible work done on the system, $\mathrm{d}W = \sum_{\mathbf{p}} \partial_t \epsilon_{\mathbf{p}} (2n_{\mathbf{p}} - 1)\mathrm{d}t = VEj^{\mathrm{c}}(t)\mathrm{d}t$, while the second corresponds to the heat exchange, $\mathrm{d}Q = 2\sum_{\mathbf{p}} \epsilon_{\mathbf{p}} \partial_t n_{\mathbf{p}} \mathrm{d}t = VEj^{\mathrm{c}}(t)\mathrm{d}t$, where we have expressed everything by the properties of the lower band. Correspondingly the work done on the system and the heat are

$$W = VE \int_0^t \mathrm{d}s\, j^{\mathrm{c}}(s) \tag{3.19}$$

$$Q = VE \int_0^t \mathrm{d}s\, j^{\mathrm{p}}(s)\,. \tag{3.20}$$

It is easy to check that the sum of the heat and work yields the total energy of the time evolved state $\Delta E = W + Q = \sum_{\mathbf{p}} 2\epsilon_{\mathbf{p}} n_{\mathbf{p}}$, i.e. simply the sum of the energy absorbed by the excited modes.

3.3 Steady state picture from Drude theory

The Drude picture provides a heuristic way to relate our results to optical conductivity studies of a WSM in the presence of impurities. In general, this is expected to work [160] for (contributions to) quantities independent of the relaxation time, as e.g. the high frequency conductivity or the universal minimal conductivity of graphene [166]. In this spirit, the dynamics described above holds until a characteristic time determined by an effective scattering rate $1/\tau$, and the zero frequency limit of the AC conductivity can be estimated by substituting time as $t \to \tau$. This results in the counterintuitive conclusion that in the $t_\Lambda < \tau < t_E$ region, the conductivity is proportional to the scattering rate, $\sigma(\omega \to 0) \approx \frac{e^2}{12\pi^2 \hbar v_F \tau}$, which agrees with the results of Ref. [167] based on Kubo formula calculations. Although this simple Drude picture works well for graphene [158], it fails to describe the transport properties of WSMs because in 3D, the density of states at the Weyl point vanishes even in the presence of small amounts of disorder [168], and concomitantly the quasiparticle lifetime diverges [137, 138]. The Drude picture can be rescued if we apply it to $j_{\mathbf{p}}$, substituting the time variable with the momentum dependent lifetime, and then evaluating the integral. The scattering rate in the Boltzmann or Born

approximation is $1/\tau_{\mathbf{p}} = 2\pi\gamma g(\epsilon_{\mathbf{p}})$ [137, 138], where $g(\epsilon) = \frac{\epsilon^2}{2\pi^2\hbar^2 v_F^3}$ is the density of states, and γ characterizes the scattering strength. In the large scattering limit $\gamma \gg \frac{\hbar v_F^2}{\Lambda}$, integrating Eq. (3.7) with $n_{\mathbf{p}}(\tau_{\mathbf{p}})$ from (3.11) reproduces the results of Refs. [137, 138], that is

$$\sigma \sim \frac{e^2 v_F^2}{\hbar\gamma}, \tag{3.21}$$

with a different prefactor and an additional logarithmic correction $\sim \frac{e^2 v_F^2}{\hbar\gamma} \ln(\frac{\hbar v_F^2}{\gamma\Lambda})$. The above treatment is valid for small electric fields $eE \ll \frac{\gamma^2\Lambda^4}{\hbar^3 v_F^3}$, when the dominant contribution to the current comes from the momenta satisfying $\tau_{\mathbf{p}} \ll t_E$. In the case of additional Weyl nodes in the Brillouin zone, internode scattering can occur on a timescale τ_{inter}. This also limits our real time study to $t < \tau_{inter}$, above which internode processes should be taken into account. This is clearly beyond the scope of the present work.

If the scattering strength is small, such that there is enough time for the modes to go through the LZ transition, then the steady state occupation profile will be qualitatively similar to the LZ solution. As the quasiparticle lifetime is finite everywhere except in the close vicinity of the Weyl point, the cylinder of densely excited states will not extend to infinity, but will be characterized by a finite length $eE\tau_{\text{eff}}(E)$. The precise form of τ_{eff} depends on the detailed nature of the scattering process. If there is a constant scattering rate $1/\tau$, then $\tau_{\text{eff}} = \tau$, but generally it will depend on the electric field. The Drude picture estimates the stationary current in the non-linear regime as

$$j_{\text{stac}} = \frac{1}{4\pi^3}\frac{e^3E^2}{\hbar^2}\tau_{\text{eff}}(E), \tag{3.22}$$

and Ohm's law breaks down. The explicit E dependence, however, depends strongly on the precise form of $\tau_{\text{eff}}(E)$. In case the relaxation time becomes independent of the electric field in the non-linear region, a crossover from the $j \sim E$ linear region to a $j \sim E^2$ non-linear region is expected.

3.4 Statistics of pair creation

The expectation value and time evolution of the current is largely influenced by the number of pairs created, as follows from Eqs. (3.6, 3.7). This we now investigate in more detail. Although the expectation value of a quantity reveals much about underlying physical processes, fluctuations contain essential information as well and are important to provide a comprehensive description of the system [8]. Therefore, beyond simple expectation values, we study the fluctuations of the pairs created by their full distribution function. This provides a complementary measure to characterize the out-of-equilibrium state. As opposed to calculating the probability distribution function of pairs created directly, it is more convenient to work with the cumulant generating function (CGF) in unit volume, which is the logarithm of the characteristic function $\phi(\varphi) = \frac{1}{V}\ln\left\langle \exp(i\varphi\hat{N})\right\rangle$. Here, $\hat{N}$ denotes the excitation number operator, V is the volume, and the expectation value is taken with the time evolved initial state. The CGF is expressed as sum over momentum

space,

$$\phi(\varphi) = \frac{1}{V}\sum_{\mathbf{p}} \ln\left[1 + (\exp(i\varphi) - 1)n_{\mathbf{p}}\right] \tag{3.23}$$

The probability density function is the inverse Fourier transform of the characteristic function, that is, $p(n) = \frac{1}{2\pi}\int \mathrm{d}\varphi\, \exp(V\phi(\varphi) - in\varphi)$. For short perturbation, i.e. $t \ll t_E$ the excitations add up from an extended region in momentum space with small excitation probability. The contribution from $p \lesssim 2eEt$, where $n_{\mathbf{p}} \sim 1$, is negligible because of the small volume of the domain $\sim t^3$, and a Taylor expansion of the logarithm in Eq. (3.23) gives a good approximation, $\phi(\varphi) = (\exp(i\varphi) - 1)\frac{1}{V}\sum n_{\mathbf{p}}$. That is, the total number of excitations per unit volume is Poissonian as $p(n) = \lambda^n \exp(-\lambda)/n!$ with

$$\lambda = \frac{1}{12\pi^2}\frac{(eE)^2 t}{\hbar^2 v_F} S_2(t/t_\Lambda)\,, \tag{3.24}$$

where $S_2(y) = \int_0^y \mathrm{d}x\, \sin^2 x/x^2 \approx y$ for $y \ll 1$, while it saturates to $\pi/2$ for $y \gg 1$. All cumulants of the Poisson distribution are equal to the single parameter λ. The first cumulant is the expectation value, that is, for $t \ll t_\Lambda$ the excitations are created quadratically in time, while for $t_\Lambda \ll t \ll t_E$, the creation rate is constant. This behavior is clearly seen in Figure 3.5, where we compare the numerically determined cumulants with the approximate solutions.

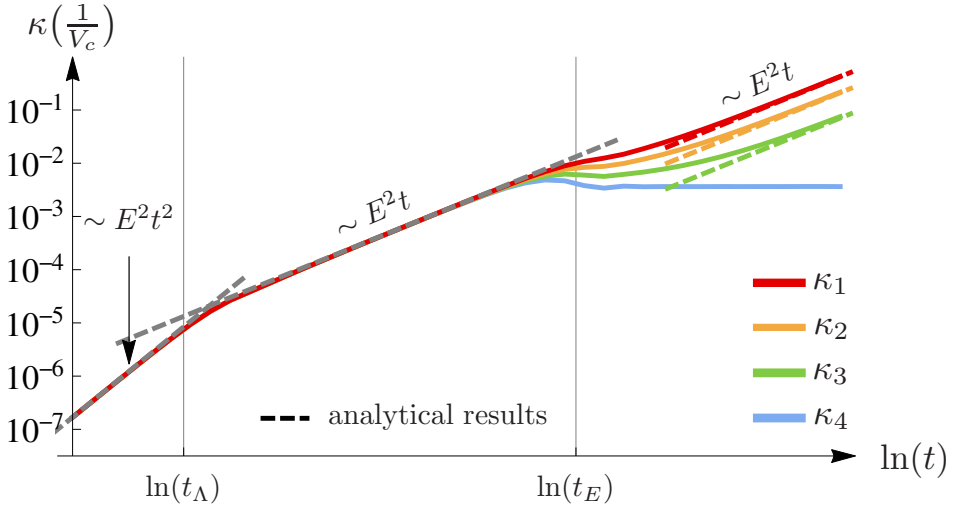

Figure 3.5: Time evolution of the cumulants (κ_{1-4}) of electron-hole pairs per unit volume (log-log plot, numerical results). The cumulants coincide for $t \ll t_E$, which is a clear signature of the Poissonian distribution. The grey dashed lines show the $t \ll t_\Lambda$ and $t \gg t_\Lambda$ asymptotics of the analytical formula Eq. (3.24). For long times, the cumulants branch and follow the approximate formulae derived from Eq. (3.25) (colored dashed lines) within a time independent constant coming from the difference between the exact $n_{\mathbf{p}}$ and the LZ approximation (Figure 3.3).

For $t_E \ll t$ the excited states are confined to a cylinder in momentum space, and substituting Eq. (3.12) into (3.23) yields

$$\phi(\varphi) = -\alpha\, \mathrm{Li}_2(1 - \exp(i\varphi)) \tag{3.25}$$

$$\alpha = \frac{1}{8\pi^3}\frac{(eE)^2 t}{\hbar^2 v_F} \tag{3.26}$$

where $\mathrm{Li}_2(x) = \sum_{m=1}^{\infty} x^m/m^2$ is the dilogarithm function [169], in agreement with Ref. [170]. As time evolves the higher cumulants start to deviate from the first one, and the distribution is no longer Poissonian (see Figure 3.5). The cumulants are determined from the series expansion of the CGF, the first few being $\kappa_1 = \alpha$, $\kappa_2 = \alpha/2$, $\kappa_3 = \alpha/6$, $\kappa_4 = 0$. Except for the variance all even cumulants vanish. There is a time independent contribution from the $p_x \approx 0$ and $p_x \approx eEt$ regions in $n_{\mathbf{p}}$ (see Figure 3.3), which is not captured in Eq. (3.12), and which gets overwhelmed by the time dependent terms. Apart from this, the cumulants listed above approximate very well the numerical results (Figure 3.5). The peak of the distribution function is well captured in the central limit theorem (CLT) approximation, which states that the excitation number is Gaussian with mean α and variance $\sigma^2 = \alpha/2$: $p(n) = \frac{1}{\sqrt{2\pi\alpha}} \exp[-(n-\alpha)^2/\alpha]$. This approximation neglects the cumulants higher than the second. The asymptotic decay of the distribution can be determined from the Gärtner-Ellis theorem [171], which in this case is essentially a saddle point approximation of the inverse Fourier transform of the characteristic function. The probability of exciting a large number of pairs decays slower than estimated from the CLT, but still in a Gaussian manner $p(n) \sim \exp(-n^2/2\alpha)$ (note the factor 2 difference in the denominator of the exponential with respect to the Gaussian distribution).

3.5 Probability of no current and the vacuum persistence probability

In spite of the applied electric field, there is a finite probability of no pair creation and no induced current, also known as the vacuum persistence probability. The vacuum persistence probability characterizes the time evolution similarly to the Loschmidt echo: it measures the overlap of the non-equilibrium time evolved wave function $U(t,0)\,|0\rangle$ with a reference wave function, which in this case is the adiabatically evolved state. Analyzing the decay of this probability provides an alternative way to determine the pair-creation rate, which was used e.g. by Schwinger in his seminal paper [140]. The vacuum persistence probability is $P_0(t) = |\,\langle\tilde{0}|\,U(t,0)\,|0\rangle\,|^2$, where $U(t,0)$ is the time evolution operator in the external field, $|0\rangle$ and $|\tilde{0}\rangle$ are the (Schrödinger) vacua at time 0 and t respectively. With the knowledge of $n_{\mathbf{p}}$ it is expressed as

$$P_0 = \exp\left(-\sum_{\mathbf{p}} \ln(1-n_{\mathbf{p}})\right) \equiv \exp\left(-Vwt\right), \tag{3.27}$$

where

$$w = \frac{1}{t} \times \begin{cases} \lambda & \text{for } t \ll t_E, \\ \dfrac{\alpha\pi^2}{6} & \text{for } t \gg t_E \end{cases} \tag{3.28}$$

is the rate of vacuum decay per unit volume and time, increasing as E^2 and being independent of time for $t \gg t_\Lambda$ and increasing linearly with time for $t \ll t_\Lambda$. Alternatively, the pair-creation rate can also be defined as the total number of pairs created divided by the time it took, i.e. as κ_1/t. Nevertheless, these two definitions agree in the short time limit and only differ by a constant prefactor in the long perturbation limit (Figure 3.6).

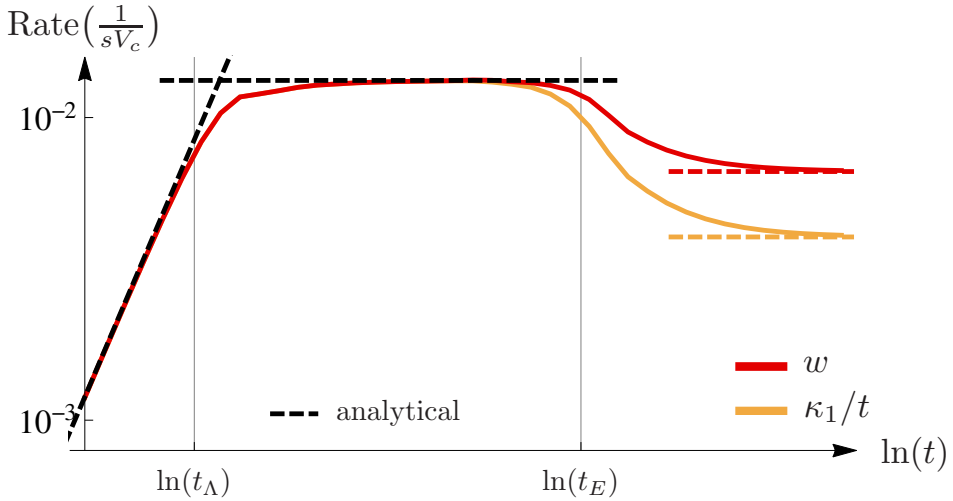

Figure 3.6: Particle creation rate as a function of time estimated from the vacuum persistence probability and from the total number of excitations (log-log plot). The dashed lines show the results of Eqs. (3.24,3.26) and Eq. (3.28).

3.6 Finite temperature

So far we have assumed the initial state to be the ground state without any excitations, which describes the zero temperature response of WSMs. An arbitrary initial distribution function can be handled similarly, as long the modes with different momenta are independent, which is the case e.g. at finite temperature. Let $f(\mathbf{p})$ be the probability distribution function of having an excitation with momentum $\mathbf{p}$ in the initial state. The post-quench occupation number is expressed as a weighted sum of the excitation probability of an unexcited and an excited mode as [157]

$$n^f_{\mathbf{p}} = [1 - f(\mathbf{p} - e\mathbf{E}t)]\, n_{\mathbf{p}} + f(\mathbf{p} - e\mathbf{E}t)\, [1 - n_{\mathbf{p}}] \ ,$$

where $f(\mathbf{p}) = 1/(\exp(\beta\epsilon_{\mathbf{p}}) + 1)$, $\beta = 1/k_B T$. The initial number of excited states due to thermal fluctuations is $n_T \sim 1/(\beta\hbar v_F)^3$, which is small near $T = 0$, and does not modify qualitatively the results. This argument applies for systems with thermal initial density matrices, which are detached from the environment during time evolution. This assumption needs a thermalization time much longer than the observation time, which is usually not satisfied in condensed matter, but could be achieved with cold atoms. Similarly a small deviation in the Fermi energy from the Weyl point gives only a subleading correction.

Our results can be readily applied also for inversion symmetric Dirac semimetals (referred to as structure I in Ref. [62]). The low energy excitations of these systems are described by a 4×4 Dirac equation, which is decoupled to two degenerate Weyl fermions with opposite chirality. As the electric field does not couple these Weyl fermions, the two copies behave independently, which can be incorporated in a factor of 2 in the current and in the cumulants. On the other hand, in inversion symmetry-breaking Dirac semimetals (called structure II in Ref. [62]), the electric field couples the two copies of the (nondegenerate) Weyl fermions. If the inversion symmetry breaking is small, the results do not change qualitatively, but generally the description of the tunneling due to the electric field becomes more involved.

3.7 Conclusion

In this chapter we have studied the nonlinear response of WSMs after switching on an external electric field before Bloch oscillations set in. The ultrashort time dynamics is non-universal and the current depends on the details of the band structure at high energies. The current and the number of created electron-hole pairs grow linearly and quadratically with time, respectively. The universal properties of Weyl nodes are manifested in the intermediate and long time responses. In particular, at intermediate times, the current *decays* as $1/t$ due to the interplay of the number of created pairs and the available phase space. Particles are created at a constant rate, generating a Poissonian distribution for the statistics of the electron-hole pairs. At long times, the particle creation rate takes on a constant value again, but the current starts to increase again in time because of the increasingly large number of pairs moving in the same direction. The distribution function of excitations crosses over from a Poissonian profile to a Gaussian distribution, which follows from the central limit theorem, applicable in the long time limit due to the large number of pairs created. The real time evolution of the current is translated to the conductivity of disordered WSMs within a generalized Drude picture, reproducing the results of previous calculations with different methods. This is a remarkable example of a problem from high energy physics which naturally corresponds to one in condensed matter physics with a separate set of observables, and which allows an exquisitely detailed analysis, thus holding the promise of a detailed experimental study in a tabletop experiment.

4 Floquet topological phases coupled to environments

As discussed in section 1.2 of the introduction, a prospering application of Floquet physics is engineering topologically nontrivial band structures by exposing normal insulators to periodic driving. Although the resulting Floquet spectrum often possesses a topology different from that of their static parents, the actual occupation of the various Floquet bands is, however, essential to evaluate physical observables. For example, a topologically non-trivial but only partially filled band cannot profit from topological protection.

In this last chapter of the thesis we study equilibration properties of periodically driven systems attached to environments. Equilibration in periodically systems is an intricate question from multiple points of view. First, as we have mentioned in section 1.1, generic interacting quantum systems are conjectured to approach an infinite temperature state in the presence of global periodic driving, which is a consequence of absorbing energy continuously from the external perturbation. However, when we couple them to an infinitely large environment, heat can flow away from the system to the bath, which can lead to a qualitatively different steady state. Second, in non-driven systems, according to the laws of statistical mechanics, a weak coupling to a bath in thermal equilibrium leads to thermal occupation of the eigenstates, which means that the occupation probability is a function of solely the *energy* of the states. Floquet systems with dissipation are also expected to reach steady states, which can be a periodic function of time due to the periodicity of the Hamiltonian. It is an interesting question whether there is a simple analogue of the energy in the non-driven case, which determines the occupation of these steady states.

The most convenient framework to study steady states in periodically driven systems is through the Floquet theory, which we have briefly introduced in section 1.2. The Floquet solution Eq. (1.9) of the time-dependent Schrödinger equation (1.8),

$$\Psi_n(t+T) = e^{-i\epsilon_n T}\Psi_n(t)\,,$$

describes a time periodic state in the sense that it obtains only a phase factor after a driving period, and expectation values of observables in this state are periodic. Based on the analogy between the energy in non-driven systems and the quasienergy ϵ_n, the latter could be a candidate to determine the filling of the steady states in a thermal environment. However, due to the breaking of continuous time translation symmetry,

the quasienergies are well-defined only modulo $\omega = \frac{2\pi}{T}$ (we set $\hbar = 1$ throughout this chapter), hence there is no unambiguous ordering of the Floquet quasienergies. This is illustrated on Figure 4.1 for a hypothetical translational invariant 1D system, where the quasienergies form two nonequivalent bands, which can be arbitrarily shifted by multiples of ω. These replicas of the Floquet bands (also called shadow bands) are experimentally detectable by time- and angle-resolved photoemission spectroscopy [172]. Unless there is

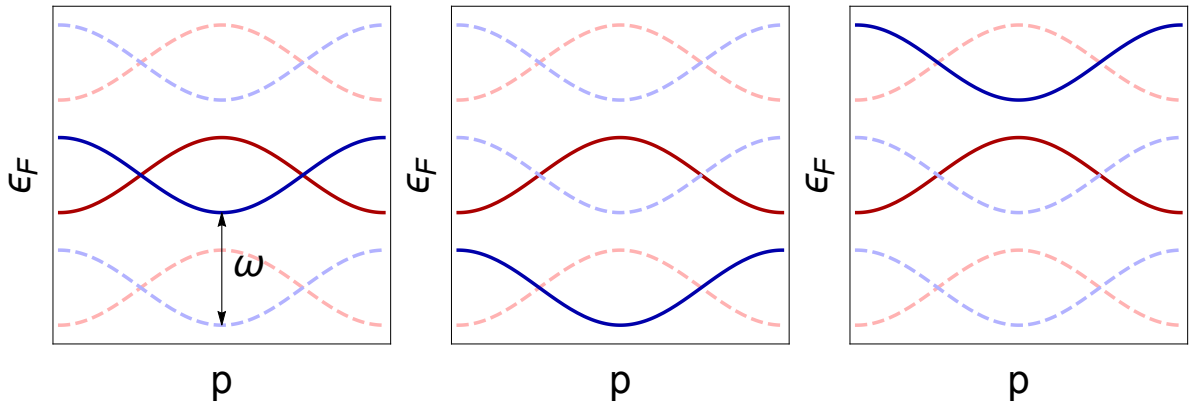

Figure 4.1: Illustration of nonequivalent Floquet bands (solid lines), and their replicas (dashed lines) shifted by multiples of the driving frequency in a translational invariant system. The choice of the reference Floquet bands is arbitrary (left, middle and right panels), and there is no notion of lower-lying quasienergy bands, which are filled at low temperatures in contrast to non-driven systems.

a natural ordering of the Floquet bands, Floquet states cannot be filled according to a simple decaying function of the quasienergies. An example where such an ordering can be constructed is the case of high frequency driving, when the ordering of quasienergy levels is defined by the Hamiltonian obtained from the high frequency expansion [173]. Another example where the Floquet states are filled with respect to their quasienergy is presented in section 4.3.1.

A phenomenological way of determining filled Floquet states [174–176] relies on the average energy [39], defined as

$$\bar{E}_n = \frac{1}{T}\int_0^T \mathrm{d}t\ \langle \Psi_n(t)|H(t)|\Psi_n(t)\rangle \tag{4.1}$$

which is always single valued as opposed to the ladder of quasienergies. Within the average energy concept, the states with lower average energy are filled first in a low temperature environment. This scenario is illustrated on Figure 4.2. Although this scenario might sound intuitive, in contrast to the non-driven case, there is no underlying microscopic theory which would validate this picture.

The rigorous way to determine the filling of Floquet bands is through coupling the system to an environment. This setup defines the field of driven-dissipative systems, which has also been studied in the literature [11, 173, 177–185]. Most of the recent studies were related to driven graphene, showing that dissipation effects generally inhibit the

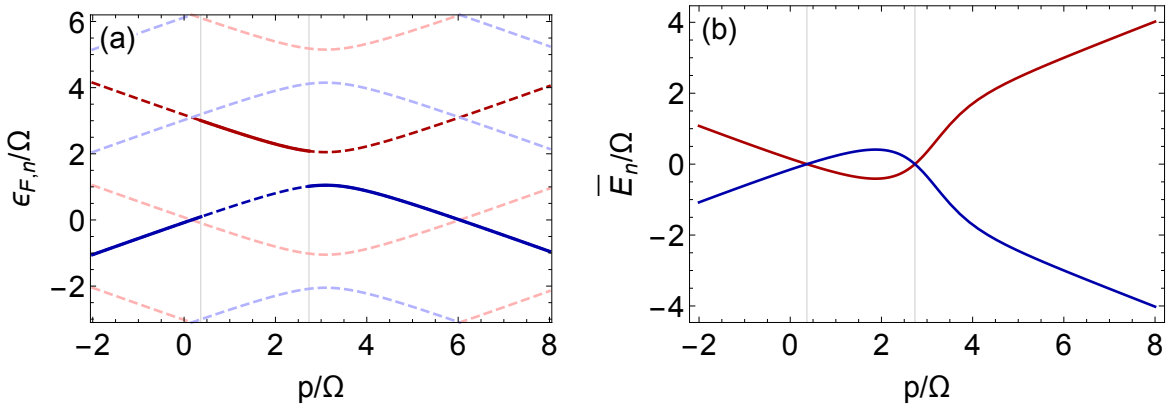

Figure 4.2: (a) Within the average energy concept the nonequivalent Floquet bands (red and blue thick dashed lines, partially covered by solid lines) are filled with respect to their average energy, illustrated as thick solid lines. The Floquet shadow bands are also shown as pale replicas. (b) The time averaged energy as a function of momentum, with the red (blue) curve corresponding to the red (blue) quasienergy band. The curves correspond to Eqs. (4.5,4.7) with $n = \pm$, $\omega = 3.1\Omega$.

naive generalization of the static results on topological band structures to the Floquet case, due to the non-thermal occupation of these bands. Moreover, the occupation is not even universal in sense that it depends not only on the temperature, but also on other properties of the bath, as well as on the way the system is coupled to the bath. So far we assumed that the Floquet basis, which is although a natural choice to study steady states, is also characterized by a well defined occupation. We find this behavior in the infinitesimal system-bath coupling limit in section 4.3.1. However, it is also possible that the steady states filled in an environment are not the Floquet states, which we find at finite system-bath coupling near resonances (section 4.3.2).

In the following, we restrict our analysis to a particular system, which had been studied previously within the average energy concept [186], and we coupled it in various forms to thermal environments. Interestingly, we found qualitative agreement with the average energy concept [21].

4.1 Quantum spin Hall edge states irradiated by circularly polarized light

As we have introduced in section 1.4, topological insulators (TI) represent peculiar states of matter with robust, topologically protected conducting edge or surface states [53, 187], and due to the strongly coupled spin and charge degrees of freedom, possible applications in spintronics or quantum computation have been proposed. In particular, the two-dimensional TI, i.e. the quantum spin Hall (QSH) state has been predicted and experimentally observed for a number of systems, including graphene [57], HgTe/CdTe [58, 133] and InAs/GaSb [188] quantum wells, lattice models [189–191] and multicomponent ultracold fermions in optical lattices [192–194].

Near the Fermi energy, the QSH insulator is characterized by counter-propagating spin-up and spin-down fermions localized along the edges of a finite sample, whose energy lie in the bulk band gap, see the middle panel of Figure 1.4 for illustration. Within the framework of the average energy concept, an interesting proposal was made in Ref. [186] to induce quantized photocurrent in a quantum spin Hall insulator by irradiating its edges with circularly polarized light. The electromagnetic field acts as a periodic driving as it couples the QSH edge states. When the frequency of the driving matches twice the energy of the Zeeman coupling, a topological phase transition was found to a non-quantized photocurrent.

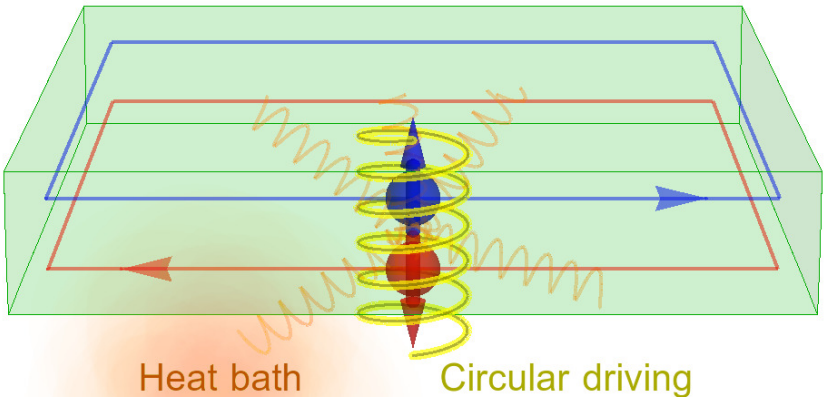

Figure 4.3: The cartoon of the system studied in this chapter, consisting of a QSH edge state with spin filtered conducting channels, interacting with circularly polarized electromagnetic field and coupled to an environment.

The one-dimensional chiral edge state of a QSH insulator in a circularly polarized radiation field, shown in Figure 4.3, is described by the non-interacting Hamiltonian $\tilde{\mathcal{H}}_S = \sum_p \psi_p^\dagger \tilde{\mathcal{H}}_S(p)\, \psi_p$, with $\psi_p^\dagger = (\psi_{p,\uparrow}^\dagger, \psi_{p,\downarrow}^\dagger)$ and

$$\tilde{\mathcal{H}}_S(p) = \tfrac{1}{2} p \sigma_z - \tfrac{1}{2}\Omega(\sigma_+ \mathrm{e}^{-i\omega t} + h.c.). \tag{4.2}$$

Here $\psi_{p,\sigma}^\dagger$ creates a QSH edge excitation of momentum p and spin σ, with $\frac{1}{2}p$ being the energy of the right moving spin up fermions, and $-\frac{1}{2}p$ being that of the left moving spin down fermions (Fermi velocity v_F is set to 1/2). The term with Ω comes from the Zeeman coupling between the magnetic component of the ω frequency electromagnetic field and the electron's spin, and Ω is identified as the Rabi frequency. The laser frequency is assumed to be smaller than the bulk gap of the QSH insulator. In Eq. (4.2) we neglected the effect of the electric field of the laser, whose contribution is small compared to the Zeeman coupling for small intensity or large frequencies satisfying $v_F e E_0/\omega \ll \hbar\omega$, with E_0 being the amplitude of the electric field oscillations. For more details about the orbital effect see Ref. [186] and its supplementary material.

4.1.1 Chiral edge current in the average energy concept

First, we review the Floquet solution and the induced edge current within the average energy concept [186]. The time-dependent Schrödinger equation,

$$i\partial_t \Psi_{p,\pm}(t) = \tilde{\mathcal{H}}_S(p)\Psi_{p,\pm}(t), \tag{4.3}$$

is solved using the Floquet ansatz Eq. (1.9) for the steady state solution,

$$\Psi_{p,\pm}(t) = \exp[-i\epsilon_\pm(p)t]\Phi_\pm(p,t). \tag{4.4}$$

Here, $\epsilon_\pm(p)$ denotes the Floquet quasienergy, and $\Phi_\pm(p,t) = \Phi_\pm(p,t+T)$ with $T = 2\pi/\omega$,

$$\epsilon_\pm(p) = \frac{\omega \pm \Omega'}{2}, \tag{4.5}$$

$$\Phi_\pm(p,t) = \frac{1}{\sqrt{2\Omega'}} \begin{pmatrix} \sqrt{\Omega' \mp \delta\omega} \\ \mp \exp(i\omega t)\sqrt{\Omega' \pm \delta\omega} \end{pmatrix}, \tag{4.6}$$

where $\Omega' = \sqrt{\delta\omega^2 + \Omega^2}$ is the renormalized Rabi frequency and $\delta\omega = \omega - p$ denotes the detuning. The average energy Eq. (4.1) in the Floquet states is calculated as

$$\bar{E}_\pm(p) = \frac{1}{T}\int_0^T \mathrm{d}t\, \langle \Psi_{p,\pm}(t)|\tilde{H}_S(p)|\Psi_{p,\pm}(t)\rangle = \pm\frac{1}{2}\left[\Omega' - \frac{\omega\delta\omega}{\Omega'}\right]. \tag{4.7}$$

At low frequencies $\omega < 2\Omega$, one of the quasienergy bands, $\epsilon_-(p)$, is characterized by lower average energy than the other for all momenta. Within the average energy concept it implies a completely filled $\epsilon_-(p)$ and an empty $\epsilon_+(p)$ band. The electric current operator is $\hat{j}_p = \frac{1}{2}e\sigma_z$ (since $v_F = 1/2$), and the photocurrent is evaluated as

$$j(\omega) = j_c = \frac{e}{2}\frac{1}{2\pi}\int_{-\Lambda}^{\Lambda} \mathrm{d}p\, \langle \Phi_-(p,t)|\sigma_z|\Phi_-(p,t)\rangle = \frac{e}{4\pi}\int_{-\Lambda}^{\Lambda} \mathrm{d}p\, \frac{\delta\omega}{\Omega'} = \frac{1}{2\pi}e\omega\,, \tag{4.8}$$

where a symmetric cutoff $\Lambda \to \infty$ was introduced to evaluate the integral, as in Ref. [186]. This expression has a simple physical interpretation: in every period a single charge is transmitted through the edges, and we refer to this as quantized edge current j_c. In the adiabatic $\omega \to 0$ limit this result corresponds to the Thouless charge pumping [195], which was also obtained for a QSH insulator in rotating magnetic field in Ref. [196].

When the driving frequency exceeds 2Ω, the average energy $\bar{E}_+$ of the ϵ_+ band becomes lower than $\bar{E}_-$ for $p_- < p < p_+, p_\pm = \frac{1}{2}(\omega \pm \sqrt{\omega^2 - 4\Omega^2})$, where population inversion occurs. This is shown on Figure 4.2 for $\omega = 3.1\Omega$. The electric current then obtains contribution from both of the quasienergy bands, which breaks down the quantization,

$$j(\omega) = j_c - \frac{e}{4\pi}\int_{p_-}^{p_+} \mathrm{d}p\, \langle \Phi_-(p,t)|\sigma_z|\Phi_-(p,t)\rangle - \langle \Phi_+(p,t)|\sigma_z|\Phi_+(p,t)\rangle \tag{4.9}$$

$$= \frac{e}{2\pi}[\omega - (\sqrt{\omega p_+} - \sqrt{\omega p_-})]\,. \tag{4.10}$$

In Ref. [21], we extended the model for a driven QSH system [186] to include various types of environments. In particular, we studied a QSH insulator coupled to a bosonic

heat bath, and irradiated by a circularly polarized light (see Eq. (4.2)). The cartoon of the system is sketched in Figure 4.3. We found that the occupation of the bands deviates from the one found using the average energy assumption [174, 186], which leads to a *weak violation* of *current quantization* in the Floquet topological phase. Our main result concerning the induced photocurrent along the edge is summarized in Figure 4.4.

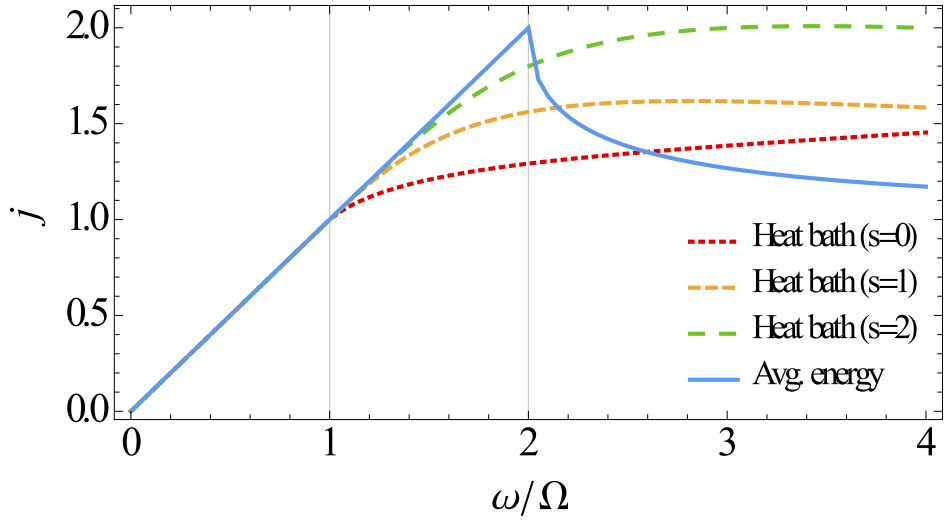

Figure 4.4: Comparison of the edge current (in units of $e\Omega/2\pi$)) when the states are occupied based on their average energy [186], and when they are coupled to a zero temperature sub-Ohmic ($s < 1$), Ohmic ($s = 1$) and super-Ohmic ($s > 1$) bath. The curves correspond to the secular approximation (defined above Eq. (4.19)), which describes the infinitesimal system-bath coupling. The $s = 0$ curve is understood as the limiting behavior as $s \to 0$.

4.1.2 Coupling the system to a heat bath

We assume that the inelastic electron scattering processes are the main source of dissipation, similar to Ref. [197]. For the sake of simplicity, we consider a model with the simplest possible form of a bosonic dissipation, where dissipation does not couple states of different momenta, but drives spin flip transitions. That is, we assume in the following that excitations of the environment have a very long wavelength compared to that of edge excitations, and will also neglect the coupling it generates between different momenta. Under these conditions, we can restrict our considerations to a single momentum mode p, which we then couple to the environment through

$$\tilde{\mathcal{H}}_{SE} = -\tfrac{1}{2} b_x \sigma_x X - \tfrac{1}{2} b_y \sigma_y Y - \tfrac{1}{2} b_z \sigma_z Z \ . \tag{4.11}$$

Here X, Y and Z denote Gaussian bosonic fields, coupled to the Pauli matrices, and b_μ ($\mu \in \{x, y, z\}$) denote the corresponding couplings. Their dynamics is encoded in the environment Hamiltonian, $\tilde{\mathcal{H}}_E = \tilde{\mathcal{H}}_E(X, Y, Z)$, whose explicit form is not needed here as it only determines the spectral functions of the noise (see section 4.2). We refer to this coupling scheme as the XYZ coupling. Below we consider also other forms of $\tilde{\mathcal{H}}_{SE}$, which are given by identifying Y with X (the XXZ scheme), and both Y and Z with X (referred to as XXX coupling).

The actual form of the system bath coupling depends on the physical realization, but as we will show, in the limit of weak coupling, they give similar results. The environment is characterized by the bath spectral functions

$$J_{\mu=x,y,z}(\omega) = \alpha\omega_c^{1-s}\omega^s \mathrm{e}^{-\omega/\omega_c}\,, \tag{4.12}$$

which determine the correlation functions

$$\gamma_\mu(\omega) = \frac{\mathrm{e}^{\beta\omega}}{\mathrm{e}^{\beta\omega}-1} J_\mu(\omega) \tag{4.13}$$

at arbitrary temperature $1/\beta$. The dimensionless quantity α is the spectral strength and ω_c is a high frequency cutoff. The system-bath coupling can be incorporated into α e.g. by considering $b_x X$ as the environment degree of freedom. In the following we keep the variables b_μ to describe the symmetry of the system-bath coupling, and we refer to the strength of the coupling by α. An Ohmic bath corresponds to $s = 1$, while $s \lessgtr 1$ describes the sub- and super-Ohmic baths, respectively.

Following the lines of Ref. [198], we apply a generalized Lindblad type formulation (the Bloch-Redfield equations) to describe how the environment affects the dynamics of the edge states. In particular we keep non-secular terms, which are not captured in the Lindblad equation, but are found to affect the dynamics considerably. This requires, in general, a numerical solution, though near critical points we find that there is a single dominant non-secular term that allows a rotation into a time independent frame. The effect of non-secular terms in graphene shined by circularly polarized light was studied numerically after a quantum quench of the driving field in Ref. [185], our method of analytical treatment of the dominant resonances generalizes to that case too. Topological edge current subject to environment has also been studied for non-driven systems [199].

4.2 The non-secular Lindblad equation

In this section, we follow the lines of Refs. [11] and [198] to outline a theoretical framework to describe the time dependent reduced density matrix by a generalized Lindblad-type equation, up to 2nd order in the coupling with an environment.

As a first step, one switches to the interaction picture with respect to the non-interacting Hamiltonians, $\mathcal{H}(t) = \tilde{\mathcal{H}}_S(t) + \tilde{\mathcal{H}}_E$, where the time evolution of the interacting system's density matrix $\rho(t)$ is governed simply by the Hamiltonian $\mathcal{H}_{SE}(t)$ which we factorize as

$$\mathcal{H}_{SE}(t) = \sum_\mu A_\mu(t) \otimes B_\mu(t). \tag{4.14}$$

Here the operators $A_\mu(t)$ and $B_\mu(t)$ act on the system and the environment, and their time evolution is governed by $\tilde{\mathcal{H}}_S(t)$ and $\tilde{\mathcal{H}}_E$, respectively. To keep notation simple, we suppress the index μ in what follows, and restore it only in the final results.

Within second order perturbation theory, the density matrix factorizes as $\rho(t) = \rho_S(t) \otimes \rho_E$, and from the von Neumann equation one derives the integral equation [200],

$$\dot{\rho}_S(t) \approx \int_0^t ds \Gamma(s)[A(t-s)\rho_S(t-s)A(t) - A(t)A(t-s)\rho_S(t-s)] + h.c, \tag{4.15}$$

with $\Gamma(t) \equiv \langle B(t)B(0)\rangle_E$ the correlation function of the operator $B(t)$.

To proceed, one usually assumes that $\Gamma(s)$ is short ranged, and then makes a Markovian approximation, $\rho_S(t-s) \to \rho_S(t)$. The physical picture behind this approximation is that memory effects within the bath are neglected, which is well-founded if the rate of change of the density matrix is small compared to the bath correlation time. Similarly, the physical interpretation of the factorization of density matrix is that the effect of higher order correlations, where subsequent interactions between the system and the bath depend on the state of the bath modified by earlier interactions, is neglected [201]. Keeping non-Markovian terms is discussed in Appendix A.2.

Then, decomposing $A(t)$ into its eigenmodes of frequencies $\nu_{-j} = -\nu_j$ (and $A_j^\dagger = A_{-j}$)

$$A(t) = \sum_{j=-J,\dots,J} A_j \mathrm{e}^{-i\nu_j t} = A^\dagger(t), \tag{4.16}$$

and taking the long time limit one obtains

$$\dot\rho_S = \sum_{j,k} \tilde\Gamma(\nu_j)\mathrm{e}^{i(\nu_k-\nu_j)t}[A_j\rho_S A_k^\dagger - A_k^\dagger A_j\rho_S] + h.c. \tag{4.17}$$

with the couplings $\Gamma(\nu_j)$ defined as

$$\tilde\Gamma(\omega) = \int_0^\infty ds\Gamma(s)\mathrm{e}^{i\omega s} = \tfrac{1}{2}\gamma(\omega) + i\,\mathrm{Im}\tilde\Gamma(\omega)\,, \tag{4.18}$$

where the real and the imaginary parts are connected by the Kramers-Kronig relation, $\mathrm{Im}\tilde\Gamma(\omega) = \mathcal{P}\int \frac{\mathrm{d}\nu}{2\pi}\frac{\gamma(\nu)}{\omega-\nu}$. The generalized Lindblad's equation (or Bloch-Redfield equation), Eq. (4.17), is the cornerstone of our analysis, what we examine beyond the secular approximation.

Usually [11, 202–205] one makes an additional assumption of keeping only secular terms with $\nu_j = \nu_k$, which we refer to as the secular approximation, also known as the "*modified rotating wave approximation*" [201]. In this limit, terms proportional to $\mathrm{Im}\tilde\Gamma(\nu_j)$ just renormalize the subsystem's Hamiltonian (produce a Lamb shift) and can thus be dropped [11], and a usual Lindblad equation is recovered,

$$\dot\rho_S^{\mathrm{sec}} = \sum_j \gamma(\nu_j)\big\{A_j\rho_S^{\mathrm{sec}}A_j^\dagger - \tfrac{1}{2}A_j^\dagger A_j\rho_S^{\mathrm{sec}} - \tfrac{1}{2}\rho_S^{\mathrm{sec}}A_j^\dagger A_j\big\}\,. \tag{4.19}$$

To appreciate the role of the non-secular terms assume that an equilibrium solution ρ_{eq} is found for the secular Eq. (4.19), and that deviations from equilibrium decay to it exponentially, $\delta\rho(t) \sim \delta\rho(0)\exp(-\Gamma t)$. Treating then the non-secular terms of Eq. (4.17) iteratively, one can immediately see that they generate corrections $\propto 1/(i(\nu_k-\nu_j)+\Gamma)$, clearly demonstrating critical regions with $|\nu_k - \nu_j| \lesssim \Gamma$. In these regions the non-secular terms become important, and the secular approximation fails.

Recovering the indices μ in Eq. (4.17), the time evolution of the density matrix is given by

$$\dot\rho_S = \sum_{\mu,j,k} \tilde\Gamma_\mu(\nu_j)\mathrm{e}^{i(\nu_k-\nu_j)t}[A_{\mu,j}\rho_S A_{\mu,k}^\dagger - A_{\mu,k}^\dagger A_{\mu,j}\rho_S] + h.c., \tag{4.20}$$

Frequency	$A_{x,j}$	$A_{y,j}$	$A_{z,j}$
$\nu_0 = 0$	0	0	$-\frac{b_z}{2}\cos\theta\sigma_z$
$\nu_1 = \Omega'$	0	0	$\frac{b_z}{2}\sin\theta\sigma_-$
$\nu_2 = \Omega' + \omega$	$-\frac{b_x}{4}(1+\cos\theta)\sigma_-$	$-i\frac{b_y}{4}(1+\cos\theta)\sigma_-$	0
$\nu_3 = \Omega' - \omega$	$\frac{b_x}{4}(1-\cos\theta)\sigma_-$	$-i\frac{b_y}{4}(1-\cos\theta)\sigma_-$	0
$\nu_4 = \omega$	$\frac{b_x}{4}\sin\theta\sigma_z$	$-i\frac{b_y}{4}\sin\theta\sigma_z$	0

Table 4.1: The operators appearing in Eq. (4.16) in the XYZ coupling defined in Eq. (4.11), $\sigma_\pm = (\sigma_x \pm i\sigma_y)/2$. In case of XXZ coupling the operators $A_{x,j}$ are given by the sum of $A_{x,j}$ and $A_{y,j}$ of the XYZ case, and similarly by $\sum_{\mu=x,y,z} A_{\mu,j}$ in the XXX coupling.

where μ runs over statistically independent noise components, see Table 4.1.

In the secular approximation only the real part of $\tilde{\Gamma}(\nu)$ appears in the stationary solution, correspondingly it behaves well for any values of s (characterizing the low-frequency behaviour of the bath spectral function), even for the white noise limiting case ($s = 0$) of the sub-Ohmic regime. However, if non-secular terms are considered, one cannot neglect the imaginary parts. If $s = 0$, $\mathrm{Im}\tilde{\Gamma}(\nu)$ diverges logarithmically for small frequency, which also implies unphysical stationary states with diverging components of the density matrix. This divergence originates from the extension of the upper limit of the integral in the Bloch-Redfield equation to ∞ in Eq. (4.15). Without extending the integral to ∞, the equation can be used to study the short time dynamics in the $s = 0$ case, but it cannot describe the stationary state. When $s > 0$, the bath correlation function decays as $\Gamma(t) \sim t^{-s}$ at zero temperature, and as the value of s is increased, the approximations made to obtain the generalized Lindblad equations remain valid for increasingly stronger system-bath couplings α.

4.3 Applying the Lindblad equation to the edge state

Let us now combine the results of the previous sections to investigate the fate of the driven spin Hall system coupled to an environment. We start by deriving the time evolution operator for $\tilde{\mathcal{H}}_S(p)$. We note first that $\tilde{\mathcal{H}}_S(p)$ becomes static in the rotating frame, i.e. using the transformation $U_r = \mathrm{e}^{-\frac{1}{2}i\omega t\sigma_z}$ yields the Hamiltonian

$$\tilde{\mathcal{H}}_{S,\mathrm{rot}}(p) = U_r^\dagger \tilde{\mathcal{H}}_S(p) U_r - U_r^\dagger \dot{U}_r = \tfrac{1}{2}(p-\omega)\sigma_z - \tfrac{1}{2}\Omega\sigma_x\,. \tag{4.21}$$

This is similar to the construction of the Floquet Hamiltonian in Eq. (1.11), with the difference that U_r does not have the right periodicity ($U_r(t+T) \neq U_r(t)$), hence the eigenvalues of $\tilde{\mathcal{H}}_{S,\mathrm{rot}}(p)$ are not equal to the Floquet quasienergies. Nevertheless, the eigenvectors of the Hamiltonian in the rotating frame are related to the Floquet states by the identity

$$\tilde{\mathcal{H}}_{S,\mathrm{rot}}(p) U_r \Psi_{p,\pm} = \pm\Omega' U_r \Psi_{p,\pm}\,. \tag{4.22}$$

Next we rotate into the z axis by $U_p = \mathrm{e}^{\frac{1}{2}i\theta\sigma_y}$ where $\sin\theta = -\Omega/\Omega'$, $\cos\theta = -\delta\omega/\Omega'$, leading to the Hamiltonian $\mathcal{H}_S^1(p) = \frac{1}{2}\Omega'\sigma_z$. Finally, the time evolution with respect to

$\mathcal{H}_S^1(p)$ is $\mathrm{e}^{-\frac{1}{2}i\Omega' t\sigma_z}$, hence the total evolution operator is

$$U_S(t) = \mathrm{e}^{-\frac{1}{2}i\omega t\sigma_z}\mathrm{e}^{-\frac{1}{2}i\theta\sigma_y}\mathrm{e}^{-\frac{1}{2}i\Omega' t\sigma_z}\mathrm{e}^{\frac{1}{2}i\theta\sigma_y}\,. \tag{4.23}$$

For convenience, in addition to the usual interaction picture, we apply the static rotation U_p to get simpler equations for the time evolution of the reduced density matrix. This is also equivalent to going into the interaction picture with the operator $\tilde{U}_S(t) = U_S(t)\mathrm{e}^{-\frac{1}{2}i\theta\sigma_y}$ instead of $U_S(t)$, which also brings us to the Floquet basis:

$$\tilde{U}_S(t)\,|\uparrow\rangle = \psi_{p,+}(t) \tag{4.24}$$

$$\tilde{U}_S(t)\,|\downarrow\rangle = \psi_{m,-}(t) \tag{4.25}$$

where $|\uparrow\rangle$, $|\downarrow\rangle$ are the eigenvectors of σ_z. In Appendix A.3 we review how the expectation values of the spin operators are calculated in this basis.

Now we express $\tilde{\mathcal{H}}_{SE}$ in this rotated interaction picture as

$$\mathcal{H}_{SE} = \sum_{j=\pm1,0} A_{z,j}\mathrm{e}^{-i\nu_j t}Z(t) + \sum_{j=\pm2,\pm3,\pm4} A_{x,j}\mathrm{e}^{-i\nu_j t}X(t) + A_{y,j}\mathrm{e}^{-i\nu_j t}Y(t) \tag{4.26}$$

with the operators and the corresponding frequencies indicated in Table 4.1. Having all operators $A_{\mu,j}$ at hand, we can now proceed and construct the non-secular and secular Lindblad equations, Eq. (4.17). and Eq. (4.19).

4.3.1 Steady states in the secular Lindblad equation

We can apply the secular approximation in the limit, where all ν_j are sufficiently different relative to linewidths. Moreover, for infinitesimal system-bath coupling, the secular approximation becomes exact. This can be seen e.g. by noticing that rescaling time by α in Eq. (4.20) upscales the frequencies of the non-secular oscillations. It is useful to expand the density matrix $\rho_S(t)$ in Pauli matrices as

$$\rho_S(t) = \tfrac{1}{2} + \sum_\mu \rho_\mu(t)\,\sigma_\mu. \tag{4.27}$$

In this basis the secular Lindblad equations read

$$\begin{aligned}
\frac{d\rho_x}{dt} &= -(\Gamma_\varphi^* + \tfrac{1}{2}\Gamma_\downarrow + \tfrac{1}{2}\Gamma_\uparrow)\rho_x \equiv -\frac{1}{T_2}\rho_x \\
\frac{d\rho_y}{dt} &= -\frac{1}{T_2}\rho_y \\
\frac{d\rho_z}{dt} &= -(\Gamma_\downarrow + \Gamma_\uparrow)(\rho_z - \rho_z^0) \equiv -\frac{1}{T_1}(\rho_z - \rho_z^0)
\end{aligned} \tag{4.28}$$

with the equilibrium values $\frac{1}{2}\langle\sigma_z\rangle_0 = \rho_z^0 = \frac{1}{2}\frac{\Gamma_\uparrow - \Gamma_\downarrow}{\Gamma_\uparrow + \Gamma_\downarrow}$, $\rho_x^0 = \rho_y^0 = 0$, and the emerging relaxation rates defined as:

$$\Gamma_{\uparrow/\downarrow} = \frac{b_z^2}{4}\sin^2\theta\gamma_z(\mp\Omega') + \sum_{\mu\in(x,y)}\frac{b_\mu^2}{16}[c_-^2\gamma_\mu(\mp\Omega'\pm\omega) + c_+^2\gamma_\mu(\mp\Omega'\mp\omega)] \tag{4.29}$$

$$\Gamma_\varphi^* = \frac{b_z^2}{2}\cos^2\theta\gamma_z(0) + \sum_{\mu\in(x,y)}\frac{b_\mu^2}{8}\sin^2\theta[\gamma_\mu(\omega) + \gamma_\mu(-\omega)].$$

Equations (4.28) are in the form of standard Bloch equations in the interaction picture with equilibrium in the z direction. We note that $\Gamma_\downarrow, \Gamma_\uparrow$ can also be derived by a simpler Fermi's golden rule calculation [203, 204], in agreement with our method. The results are the same for the XXZ and the XXX coupling, excepting that in the former we have to take $\gamma_x = \gamma_y$, and in the latter case $\gamma_x = \gamma_y = \gamma_z$.

The physical interpretation of the vanishing x and y components of the steady state density matrix is that the filling of the Floquet quasienergy bands is well defined, and the Floquet basis is the proper choice to measure occupation. The stationary value ρ_z^0 gives the steady state occupation of the Floquet states as $n_\pm(p) = \frac{1}{2} \pm \rho_z^0$.

At zero temperature a sharp difference shows up between the occupation profiles in the cases of small frequency ($\omega < \Omega$) and large frequency driving, irrespective of the actual type of the bosonic heat bath. In the former case $\Gamma_\uparrow \equiv 0$, hence the steady state is described by filling the lowest lying states of $\mathcal{H}_S^1(p)$, that is, $\Psi_{p,-}$ in the laboratory frame. However, if $\omega > \Omega$, there is a narrow domain in the momentum space ($p_-^* < p < p_+^*$, $p_\pm^* = \omega \pm \sqrt{\omega^2 - \Omega^2}$), where $\Gamma_\uparrow \neq 0$, correspondingly the steady state contains excitations with respect to the rotating frame Hamiltonian, which means partial filling of the $\Psi_{p,+}$ states. Depending on the spectral functions of the baths, inverse population is achieved in this region, see Figure 4.5.

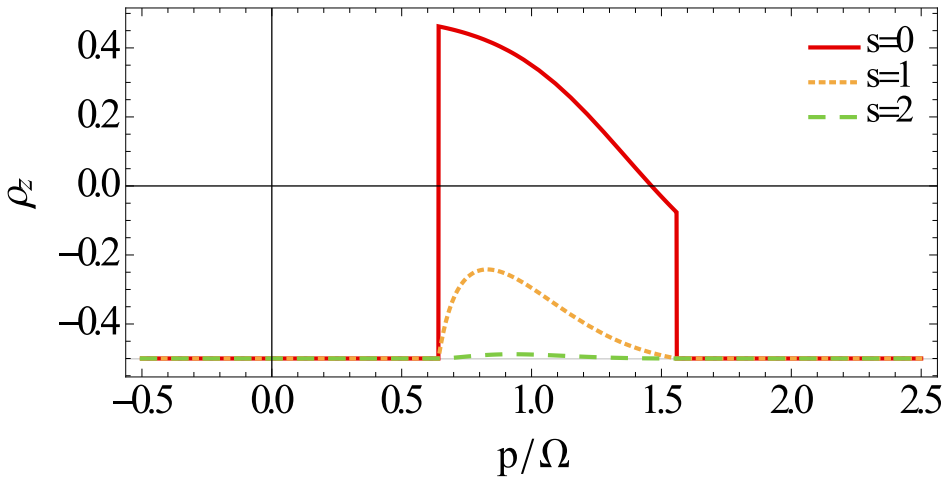

Figure 4.5: The nonvanishing element of the density matrix in the stationary state at zero temperature ($\omega = 1.1\Omega$, $\alpha \to 0$ limit). The three curves correspond to different bath spectral functions $J(\nu)$. The excitations in the steady state are with stronger weight in the sub-Ohmic ($s = 0$) case compared to Ohmic ($s = 1$) or super-Ohmic environments ($s = 2$).

We found that a weak coupling to a zero temperature environment yields qualitatively similar results for the occupation profile of the quasienergy bands to the average energy concept, but the transition point differs in the two methods ($\omega = \Omega'$ and $\omega = 2\Omega'$ respectively). Another difference is that the latter predicts total population inversion in a finite momentum range, but in the more precise treatment the excitations are weaker and depend on the spectral function of the bath (and also $p_\pm^* \neq p_\pm$).

In general, the occupation of the Floquet states is non-thermal in the sense that it cannot be written in the form of $\tilde{n}_+(\beta\tilde{\epsilon}) = \frac{e^{-\beta\tilde{\epsilon}_+}}{e^{-\beta\tilde{\epsilon}_+} + e^{-\beta\tilde{\epsilon}_-}}$, where $\tilde{\epsilon}_\pm$ is some energy determining the filling of the Floquet states and β is the inverse temperature of the environment. Nevertheless, depending on the anisotropy of the system-bath coupling $b_{x,y}/b_z$, the aver-

age energy substituted into $\tilde{\epsilon}_\pm$ provides a meaningful approximation for the temperature dependence as well, as shown in Figure 4.6.

We find an interesting limit if the bath couples only to the z component of the spins, that is, when $b_x = b_y = 0$. Then not only the system and the environment, but also the system-bath coupling becomes time independent in the rotating frame. In these circumstances, according to the general rules of statistical mechanics, the steady-state occupation of the bands is thermal with respect to the Hamiltonian $\mathcal{H}_S^1(p)$, provided the system-bath coupling is small. As the quasienergies in Eq. (4.5) are the same as the spectrum of $\mathcal{H}_S^1(p)$ except from a constant shift $\omega/2$, the occupation is thermal with respect to the quasienergies as well. A similar scenario was found for the filling of the Floquet states in graphene with a rotating Kekulé mass in Ref. [182]. It is easy to verify that the secular solution simplifies to $\rho_z^0 = -\frac{1}{2}\tanh(\frac{1}{2}\beta\Omega')$, which is indeed the thermal value. Also, in this limit, there is no signature of a transition around $\omega \sim \Omega$. Away from the $b_x = b_y = 0$ point, the system-bath coupling becomes time dependent, which results in non-thermal band occupations.

4.3.2 Beyond the secular approximation

The Bloch equations are rewritten as

$$\frac{\mathrm{d}\boldsymbol{\rho}(t)}{\mathrm{d}t} = \mathbf{B}(t)\boldsymbol{\rho}(t) + \mathbf{b}(t), \tag{4.30}$$

where

$$\mathbf{B}(t) = 2\sum_{\mu,j,k} \tilde{\Gamma}_\mu(\nu_j)\mathrm{e}^{i(\nu_k-\nu_j)t}[\mathbf{a}_{\mu,j} \circ \mathbf{a}^*_{\mu,k} - \mathbb{I}\,\mathbf{a}_{\mu,j}\cdot\mathbf{a}^*_{\mu,k}] + h.c. \tag{4.31}$$

$$\mathbf{b}(t) = \sum_{\mu,j,k} i\tilde{\Gamma}_\mu(\nu_j)\mathrm{e}^{i(\nu_k-\nu_j)t}[\mathbf{a}_{\mu,j} \times \mathbf{a}^*_{\mu,k}] + h.c. \tag{4.32}$$

with $A_\mu(t) = \mathbf{a}_\mu(t)\cdot\boldsymbol{\sigma}$ and $\mathbf{a}_\mu(t) = \sum_j \mathbf{a}_{\mu,j}\mathrm{e}^{-i\nu_j t}$, and $\mathbf{a}_{\mu,j}$ can be identified from Table 4.1. The circle symbol denotes the dyadic product, whose matrix elements are defined as $[\mathbf{v}\circ\mathbf{w}]_{a,b} = v_a w_b$, the dot symbol refers to the scalar product defined as $\mathbf{v}\cdot\mathbf{w} = \sum_a v_a w_a$, and the cross symbol denotes the usual vector product $[\mathbf{v}\times\mathbf{w}]_a = \sum_{b,c}\epsilon_{abc}v_b w_c$, where ϵ_{abc} is the Levi-Civita symbol. In the secular approximation only the $j = k$ terms are kept in Eqs. (4.31-4.32), i.e. only $\tilde{\mathbf{B}}(0)$ and $\tilde{\mathbf{b}}(0)$. The frequencies appearing in the above expansions in the XYZ and XXZ cases are $\pm(0,\ \Omega',\ 2\omega,\ \Omega'\pm 2\omega)$ in $\mathbf{b}(t)$, and $\pm(0,\ \Omega',\ 2\Omega',\ 2\omega,\ \Omega'\pm 2\omega,\ 2(\Omega'\pm\omega))$ in $\mathbf{B}(t)$. In the XXX case, additional frequencies $\pm(\omega, \Omega'\pm\omega)$ to $\mathbf{b}(t)$ and $\pm(\omega, \Omega'\pm\omega, 2\Omega'\pm\omega)$ to $\mathbf{B}(t)$ appear. For the full solution of the problem, all these terms should be taken into account, which is easy to implement numerically. Generally, all the above Fourier components appear in the time evolution of the density matrix, ρ_x and ρ_y oscillate around 0, while ρ_z oscillates around a finite stationary value. A large $\rho_{x,y}$ component of the density matrix indicates that the Floquet basis is not the appropriate one to study the steady states.

The secular approximation works well if none of the above frequencies are close to zero. In the case when one of these frequencies nearly vanishes, the stationary values are tuned away from the secular ones. The possibly dangerous terms that can vanish at certain

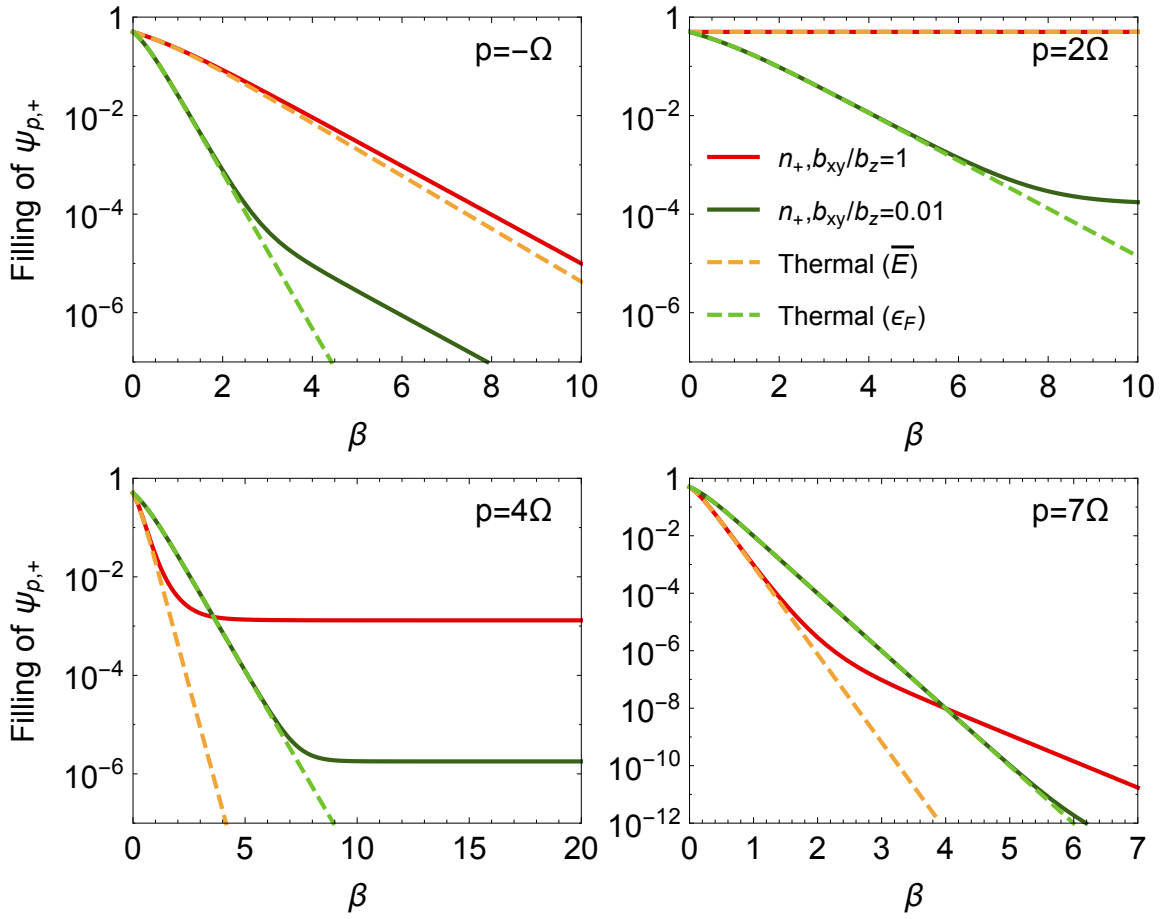

Figure 4.6: Occupation of the Floquet states (solid lines) within the secular approximation in a finite temperature Ohmic bath as a function of the inverse temperature β, at high frequency driving $\omega = 2.5\Omega$, shown at four different momenta. At $p = -\Omega$ and $p = 7\Omega$ the filling of the $\epsilon_+(p)$ quasienergy state vanishes at zero temperature. The average energy concept (orange dashed line) gives qualitatively good results for the temperature dependence of the occupations at $b_z \sim b_{x,y}$, especially at high temperature (except for $p = 4\Omega$, where it predicts vanishing occupation at zero temperature corresponding to the mismatch in $p_\pm$ and $p^*_\pm$ for the critical region). In the $b_{x,y} \to 0$ limit the occupation becomes thermal with respect to the Floquet quasienergies (light green dashed line).

momenta, possess frequencies[1] $\nu_* = \Omega' - \omega$ and $\nu_{**} = \Omega' - 2\omega$. When these frequencies become small, the deviation from the secular approximation grows, which appears as a peak in the stationary components of $\boldsymbol{\rho}(p)$, as shown in Figure 4.8.

In the vicinity of these points, analytical solutions are possible within the Dominant Frequency Approximation (DFA). When the frequency of some non-secular terms approaches zero, it drives the solution away from the secular one. The single smallest frequency appearing among the non-secular terms is the dominant one. Keeping this single frequency, Eq. (4.20) can be transformed to a time independent equation, that is readily solved, as detailed in section 4.3.3.

[1]In principle $2\Omega' - \omega$ could be dangerous as well, but it becomes unimportant due to vanishing matrix elements.

The full numerical solution of the Eq. (4.30), together with various approximate results are shown in Figure 4.8, visualizing the momentum dependence of the average value of ρ_z and $\rho_\perp = \sqrt{\rho_x^2 + \rho_y^2}$ in the Ohmic case. Note that ρ_z can become smaller than $-1/2$, or $|\boldsymbol{\rho}|$ can exceed $1/2$, which is a common feature in other non-secular approaches as well [198]. The secular approximation clearly breaks down at certain momenta, and is outperformed by the DFA there, see Figure 4.8.

Despite the several Fourier coefficients appearing in $\boldsymbol{\rho}(t)$, the spins exhibit periodic oscillations in the laboratory frame with frequency ω and higher harmonics. Indeed, switching back to the Schrödinger picture ($\tilde{\boldsymbol{\rho}}(t)$) after applying the Markovian approximation on Eq. (4.15) results in a differential equation, which only involves frequencies 0, ω and its higher harmonics (Ω' affects only coefficients via the s integration). This is favorable for numerical calculations but is also disadvantageous for analytical treatment compared to the interaction picture, which gives a natural ground to investigate the resonances and provides approximate solutions for the time evolution of the density matrix.

4.3.3 Dominant frequency approximation (DFA)

We observe that the operators $A_{\mu,j}$ in Table 4.1 are either proportional to $\sigma_\pm$ or to σ_z, thus they obtain only a phase factor under a rotation around the z axis. The secular terms always consist of an operator $A_{\mu,j}$ and its hermitian conjugate, hence they do not transform under the rotation $U = \mathrm{e}^{\frac{1}{2}i\nu t\sigma_z}$. On the other hand, the non-secular terms acquire a phase factor, which allow us to transform the dominant frequency term to be time independent, without spoiling the secular terms.

Let $\nu_d \in \{\nu_*, \nu_{**}\}$ denote the dominant frequency (the method works for the frequencies Ω', $\frac{1}{2}\Omega' - \omega$ as well), and $\boldsymbol{\rho}'(t) = R(\nu_d t)\boldsymbol{\rho}(t)$ is the vector representation of the density matrix after the rotation, where $R(\nu t)$ is the 3×3 rotation matrix around the z axis in the positive direction. Keeping only the time independent terms in the Bloch equation for $\boldsymbol{\rho}'(t)$ yields $\dot{\boldsymbol{\rho}}'(t) = \tilde{\mathbf{B}}_d\boldsymbol{\rho}'(t) + \tilde{\mathbf{b}}_d$, where $\tilde{\mathbf{B}}_d = \sum \tilde{\mathbf{B}}(\nu) - R\dot{R}^{-1}$ and $\tilde{\mathbf{b}}_d = \sum \tilde{\mathbf{b}}(\nu)$ with the sum going through $\nu \in V_d = \{0, \pm\nu_d, \pm 2\nu_d\}$. The matrix structure of the Fourier components are shown in Table 4.2, the matrix elements are given explicitly in the Appendix A.4.

$\tilde{\mathbf{B}}(0)$	$\tilde{\mathbf{b}}(0)$	$\tilde{\mathbf{B}}(\nu)$	$\tilde{\mathbf{b}}(\nu)$	$\tilde{\mathbf{B}}(2\nu)$	$\tilde{\mathbf{b}}(2\nu)$
$\begin{pmatrix} \eta & \eta_2 & 0 \\ -\eta_2 & \eta & 0 \\ 0 & 0 & \xi \end{pmatrix}$	$\begin{pmatrix} 0 \\ 0 \\ \epsilon \end{pmatrix}$	$\begin{pmatrix} 0 & 0 & \beta_1 \\ 0 & 0 & i\beta_1 \\ \beta_2 & i\beta_2 & 0 \end{pmatrix}$	$\begin{pmatrix} \chi \\ i\chi \\ 0 \end{pmatrix}$	$\begin{pmatrix} \delta & i\delta & 0 \\ i\delta & -\delta & 0 \\ 0 & 0 & 0 \end{pmatrix}$	$\begin{pmatrix} 0 \\ 0 \\ 0 \end{pmatrix}$

Table 4.2: Matrix structure of the various Fourier components ($\nu \in \{\Omega' - \omega, \Omega' - 2\omega, \Omega', \frac{1}{2}\Omega' - \omega\}$) appearing in Eqs. (4.31-4.32). All the matrix elements are $\sim \alpha$, $\epsilon = -\frac{1}{2}(\Gamma_\uparrow - \Gamma_\downarrow)$, $\xi = \Gamma_\uparrow + \Gamma_\downarrow$ and $\eta = \frac{1}{2}(\Gamma_\uparrow + \Gamma_\downarrow) + \Gamma_\phi^*$. The Lamb shift η_2 together with the other matrix elements are listed in Appendix A.4.

At this level of approximation $\boldsymbol{\rho}'$ achieves a constant stationary value determined by the matrix elements of the Fourier components. Going back to the interaction picture, we see a constant ρ_z^{stac} and oscillating $\rho_{x,y}^{\mathrm{stac}}$ with $\frac{\pi}{2}$ phase difference between them (Figure 4.7). The amplitude of this oscillation is given by $\rho_\perp = \sqrt{\rho_x'^2 + \rho_y'^2}$. These steady state values

are expressed as:

$$\rho_z'^{\text{stac}} = -\frac{\epsilon\zeta_1 - \zeta_2}{\xi\zeta_1 - \zeta_3} \qquad \rho_\perp'^{\text{stac}} = 2\left|\frac{\zeta_4}{\xi\zeta_1 - \zeta_3}\right| \tag{4.33}$$

$$\zeta_1 = \eta^2 - 4|\delta|^2 + (\nu - \eta_2)^2 \tag{4.34}$$

$$\zeta_2 = 4\,\mathrm{Re}\{\chi\beta_2^*(\eta + i(\nu - \eta_2)) - 2\chi\beta_2\delta^*\} \tag{4.35}$$

$$\zeta_3 = 4\,\mathrm{Re}\{\beta_1\beta_2^*(\eta + i(\nu - \eta_2)) - 2\beta_1\beta_2\delta^*\} \tag{4.36}$$

$$\zeta_4 = (\chi\xi - \beta_1\epsilon)(\eta + i(\nu - \eta_2)) + \tag{4.37}$$

$$+ 2\beta_2(\chi^*\beta_1 - \chi\beta_1^*) + 2\delta(\beta_1^*\epsilon - \chi^*\xi) \tag{4.38}$$

This expression makes it clear that as the dissipation strength α tends to zero, the solution approaches the secular one, $\rho_z^{\text{stac}} = -\frac{\epsilon}{\xi}$, $\rho_\perp^{\text{stac}} = 0$. This can be seen by observing that the only terms of order α are $\epsilon\nu^2$ in the nominator of ρ_z^{stac} and $\eta\nu^2$ in the denominators; all the others are at least $\mathcal{O}(\alpha^2)$. On the other hand, for any finite system-bath coupling strength, approaching the critical points - where the dominant frequency vanishes - close enough, the secular approximation breaks down. Now we discuss separately the results of the DFA for the various couplings.

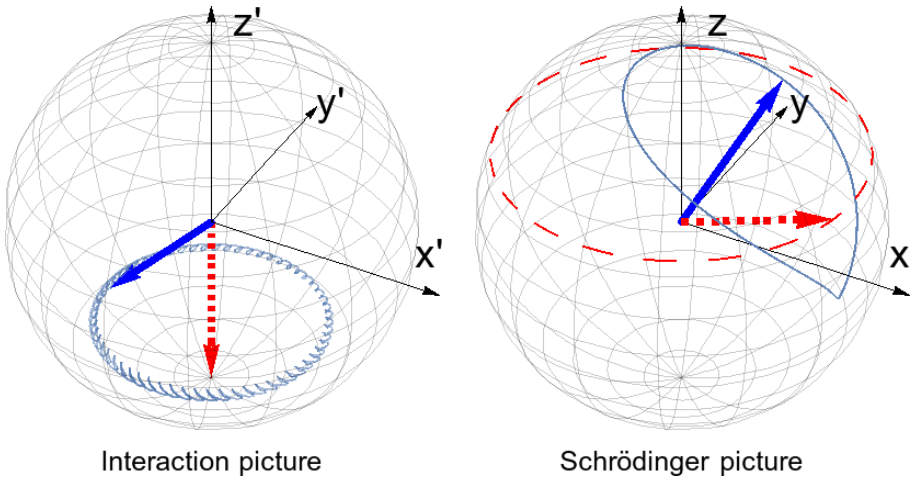

Figure 4.7: Stationary state dynamics of the density matrix on the Bloch sphere in the interaction and Schrödinger pictures. The curves show the path of $\boldsymbol{\rho}$ close to a critical point, where the non-secular terms are non negligible. In the secular approximation (red dashed curve and arrow) $\boldsymbol{\rho}$ reaches a constant value in the interaction picture, which corresponds to a circular motion in the laboratory frame (i.e. in the Schrödinger picture). In the DFA $\boldsymbol{\rho}$ draws a circle around the secular solution in the interaction picture. This circle also has a fine structure, if we go beyond the DFA (blue solid curve and arrow).

In the $U(1)$ *symmetric XYZ case*, that is, when $\gamma_x = \gamma_y$ and $b_x = b_y$, all Fourier coefficients of $\mathbf{b}(t)$ and $\mathbf{B}(t)$ vanish (see e.g. Eqs. (A.30-A.32) in the Appendix for the $\Omega' - 2\omega$ component), except for the frequencies 0, $\pm\Omega'$ and $\pm 2\Omega'$. There are no dangerous non-secular terms, and the full time evolution can be mapped to be exactly time independent applying the method described above with $\nu_d = \Omega'$. This yields an analytical solution for the stationary fermion occupations.

The $U(1)$ *breaking XYZ and XXZ case* has a single dangerous non-secular term corresponding to the frequency ν_{**} (because ν_* does not enter in $\mathbf{B}(t)$ and $\mathbf{b}(t)$). This vanishes if $\omega > \frac{1}{2}\Omega$ at the critical momenta $p_{\pm}^{**} = \omega \pm \sqrt{4\omega^2 - \Omega^2}$, giving rise to peaks in the stationary values of ρ_z and $\rho_\perp$. In contrast to the singularity in the secular solution at $\omega = \Omega$, these peaks grow up gradually as ω is increased, and are also present in the $\omega < \frac{1}{2}\Omega$ case (see Figure 4.8(c) for the same phenomenon in XXX case). We note that Eq. (4.33) is in the most general form, and it simplifies for $\nu_d = \nu_{**}$ as $\delta \equiv 0$ in this case.

In the *XXX coupling*, in addition to ν_{**}, the frequency ν_* becomes dangerous as well, and it vanishes at momenta $p_{\pm}^*$ for $\omega > \Omega$. These are the momenta between which excitations are present in the steady state even in the secular approximation. The contribution of the dominant frequency terms is that additional peaks grow at $p_{\pm}^*$ on the top of the secular solution of ρ_z and $\rho_\perp$ (Figure 4.8(a)). In principle the frequency $\nu_{***} = \Omega' - \frac{1}{2}\omega$ could be dangerous as well, but the matrix elements vanish at this frequency, $\chi = \beta_{1,2} \equiv 0$. Because of the vanishing matrix elements, it does not change the secular behavior, see e.g. Eq. (4.33).

An equivalent way to look at the DFA is to take the Fourier transform of Eq. (4.30), which maps the differential equation to an (infinite) set of coupled linear equations $i\tilde{\boldsymbol{\rho}}(\omega_i)\omega_i = \sum_j \tilde{\mathbf{B}}(\omega_i - \omega_j)\tilde{\boldsymbol{\rho}}(\omega_j) + \tilde{\mathbf{b}}(\omega_i)$. The approximation is to keep only the dominant frequency ν_d in the expansion of $\tilde{\boldsymbol{\rho}}$, neglecting the higher harmonics as well. The generalization to keep more (dominant) frequencies is straightforward in this language, but analytically hardly treatable.

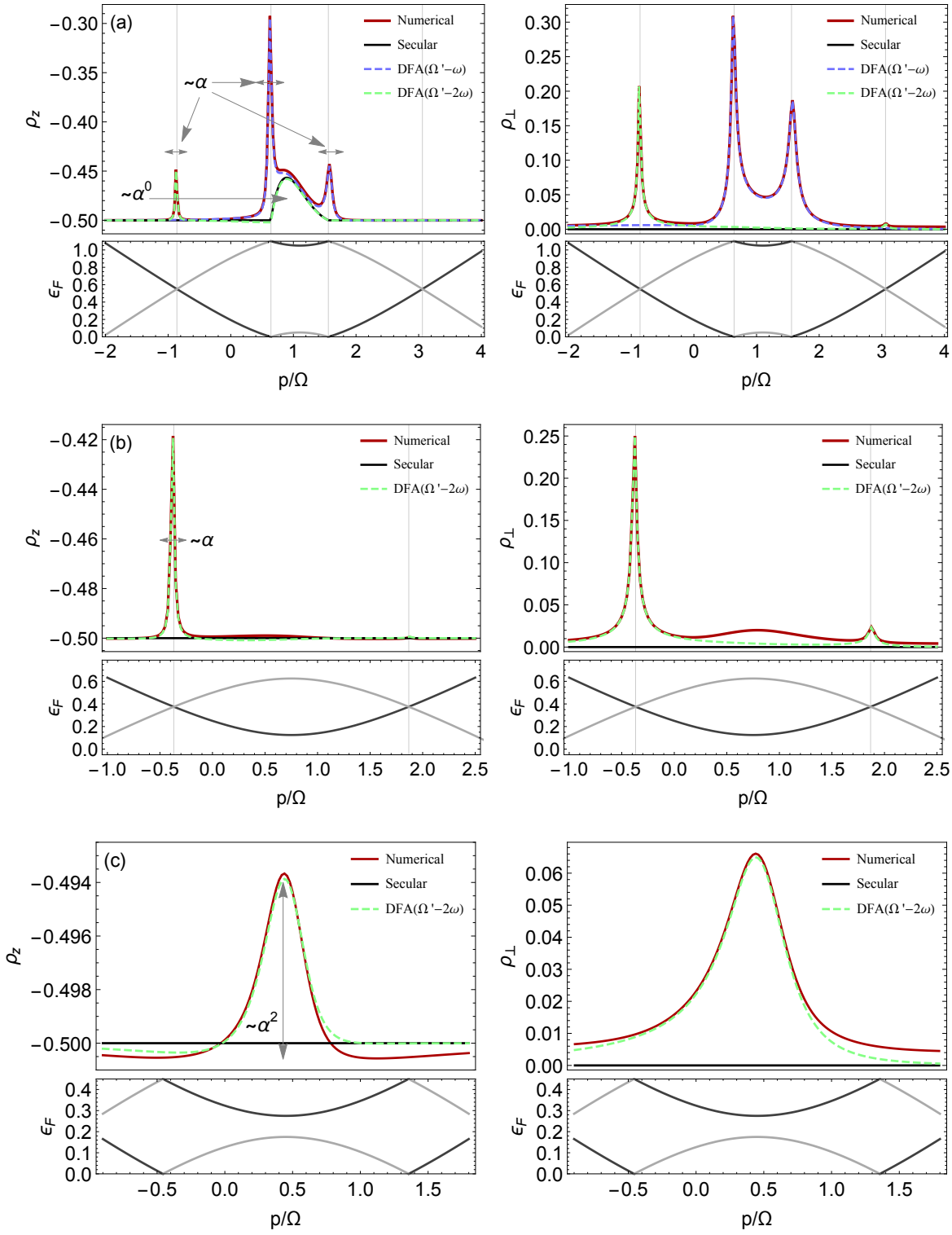

Figure 4.8: Average stationary values of ρ_z and $\rho_\perp = \sqrt{\rho_x^2 + \rho_y^2}$ for various ω/Ω ratios in the XXX case ($s = 1$, $\alpha = 0.05$). (a) $\omega > \Omega$, correspondingly $\rho_{z,\perp}$ deviate from the secular solution at critical momenta $p_\pm^*$ ($\Omega' - \omega \approx 0$) and $p_\pm^{**}$ ($\Omega' - 2\omega \approx 0$). This is attributed to two-photon transitions, where the Floquet bands touch each other (lower panels). (b) At lower frequency ($\Omega > \omega > \frac{1}{2}\Omega$) only one dangerous non-secular term survives, giving rise to peaks at $p_\pm^{**}$. (c) When $\omega \lesssim \frac{1}{2}\Omega$ the secular approximation still gets corrections because the dangerous frequency $\Omega' - 2\omega$ is small at $p \approx \omega$. The actual values of ω/Ω are 1.1 in (a), 0.75 in (b) and 0.48 in (c).

4.4 Photocurrent along the edge

Armed with the knowledge of the density matrix, we now focus on measurable quantities. Due to the electromagnetic field, a net electric current and magnetization due to the magnetoelectric effect [53] is induced along the edge. In section 4.1.1 we saw that without the environment, this current is quantized based on the average energy concept in the adiabatic limit, giving way to dissipative charge transport through a topological transition with increasing frequency ω. The photocurrent along the edge of a spin Hall insulator in the laboratory frame is determined as $j = e\int \frac{\mathrm{d}p}{2\pi}\mathrm{Tr}\{\tilde{\rho}(t)\frac{1}{2}\sigma_z\}$, which is expressed by the components of $\boldsymbol{\rho}$ in the rotated interaction picture as (see Eq. (A.18) in the Appendix)

$$j = -e\int_{-\Lambda}^{\Lambda}\frac{\mathrm{d}p}{2\pi}\left\{\frac{\delta\omega}{\Omega'}\rho_z - \frac{\Omega}{\Omega'}\left(\rho_x\cos\Omega' t - \rho_y\sin\Omega' t\right)\right\}, \tag{4.39}$$

which inherits the $2\pi/\omega$ periodicity from $\tilde{\boldsymbol{\rho}}(t)$. In the secular approximation only the DC component survives, as $\rho_{x,y} = 0$ and ρ_z is time independent. In the low frequency limit ($\omega < \Omega$) $\rho_z \equiv -\frac{1}{2}$, yielding $j_c = \frac{e\omega}{2\pi}$ similar to Eq. (4.8). When $\omega > \Omega$, there are regions where ρ_z deviates from $-\frac{1}{2}$ (shown in Figures 4.5 and 4.8), implying the breakdown of the quantization. Near the critical point the deviation form the quantized current is $\Delta j = j - j_c \sim (\omega-\Omega)^{s+3/2}$, with the exponent depending on the low frequency asymptotics of the bath spectral function.

The current has $\sim\alpha$ corrections to the secular approximation due to the non-secular terms, and the quantization of the current ceases to be exact at finite system-bath couplings (Figure 4.9(a,b)). The corrections have dual origin. On the one hand, due to photon absorption resonances near $\omega \approx \frac{1}{2}\Omega', \Omega'$, ρ_z deviates from $-\frac{1}{2}$ even for $\omega < \Omega$. On the other hand, the x, y components of the density matrix acquire oscillations at frequency Ω', which also contribute to the DC current in Eq. (4.39). The resonances produce a sharp breakdown in the current at $\omega \approx \frac{1}{2}\Omega$ due to a dangerous non-secular term present in the XXZ and XXX cases. This behavior is captured in the DFA. Figure 4.9(b) shows the crossover at $\omega \sim \frac{1}{2}\Omega$ due to the $\Omega' - 2\omega \approx 0$ resonance, and also the effect of the $\Omega' - \omega \approx 0$ resonance on the DC current. The DFA with frequencies $\Omega' - \omega$ and $\Omega' - 2\omega$ cannot yield nonzero Ω' fluctuations. To describe the effect of the second term in Eq. (4.39), one has to study the DFA with frequency Ω' (Figure 4.9(b)). The deviations of the DFA with different frequencies compared to the secular approximation are approximately additive, and one can combine them to achieve a good approximation for the total DC current.

At finite system-bath coupling, in addition to the DC component, the stationary current is also characterized by nonvanishing AC contributions, showing peaks as a function of ω (Figure 4.9(c)). The ω frequency Fourier component of the current originates from the ω, $\Omega' \pm \omega$ Fourier terms in $\boldsymbol{\rho}(t)$, which are present only in the XXX coupling. The 2ω and $\Omega' \pm 2\omega$ components of $\boldsymbol{\rho}(t)$ are responsible for the 2ω harmonic AC current, which therefore is present in the XXZ and XXX couplings. The XYZ coupling does not show any alternating current. We note that the electric field of the laser neglected in Eq. (4.2) may also contribute to the AC current [186].

In general, finite temperature also breaks down the quantization of the current. However, in the special case of $b_x = b_y = 0$, when the occupation is thermal, the current remains quantized even at finite temperature.

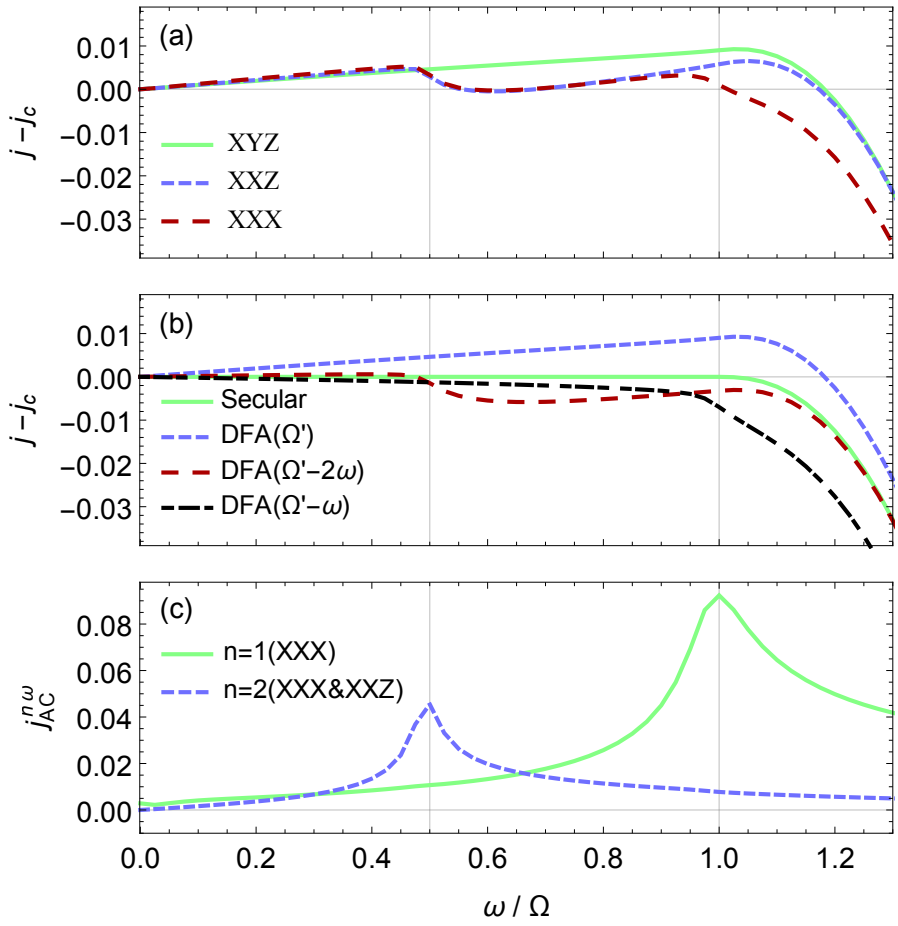

Figure 4.9: Stationary current induced by a circular driving on a QSH edge coupled to an Ohmic bath (the vertical units are in $j_c(\omega = \Omega) = \frac{e\Omega}{2\pi}$, $b_x = b_y = b_z$, $\Gamma_x = \Gamma_y = \Gamma_z$, $\alpha = 0.1$). (a) Deviation from the quantized current j_c at finite system-bath coupling, numerical solution. Various structures appear as a function of the driving frequency in the different coupling schemes, all of which are captured by the DFA with different frequencies (Ω' for XYZ; Ω' and $\Omega' - 2\omega$ for XXZ; Ω', $\Omega' - \omega$ and $\Omega' - 2\omega$ for XXX), shown on panel (b). The secular approximation corresponds to an infinitesimal system-bath coupling, where the quantization is exact until the driving frequency reaches the Rabi frequency. The 2 photon processes at finite coupling constants violate the quantization, which become effective at $\omega \sim \frac{1}{2}\Omega$. This is well captured in the DFA. (c) The photon-resonances also give rise to an AC current with frequency $n\omega$, $n \in \mathbb{N}$.

The integrated expectation value of σ_z determines both the current and the z component of the edge magnetization. The magnetization in the xy plane is calculated similarly, and, as in Ref. [186], it exhibits a circular motion on average with frequency ω (see Eq. (A.23) in the Appendix):

$$M_\perp^\omega = \int_{-\Lambda}^{\Lambda} \frac{\mathrm{d}p}{2\pi} \frac{1}{2} \left\langle \sigma_x \cos(\omega t) + \sigma_y \sin(\omega t) \right\rangle \tag{4.40}$$

$$= -\int \frac{\mathrm{d}p}{2\pi} \frac{\Omega}{\Omega'} \rho_z + \frac{\delta\omega}{\Omega'} (\rho_x \cos \Omega' t - \rho_y \sin \Omega' t) \tag{4.41}$$

Similar to the current, only the first term survives in the secular approximation, and in further analogy to the quantized current we define $M_c = \int \frac{dp}{2\pi} \frac{\Omega}{\Omega'} \frac{1}{2} = \frac{\Omega}{2\pi} \log \frac{2\Lambda}{\Omega}$, which is independent of ω and logarithmically divergent in the cutoff parameter Λ. The crossovers in ρ_z as a function of ω are also revealed in the transverse magnetization, which can be highlighted by subtracting the low frequency transverse magnetization M_c as a reference value (Figure 4.10). In the XXX and XXZ cases the magnetization acquires a finite 3ω component due to the $\Omega' \pm 2\omega$ components of $\boldsymbol{\rho}$, and the $\Omega' - \omega$ resonance in the XXX case gives rise to a finite static magnetization in the xy plane together with the second harmonic (Figure 4.10(c)).

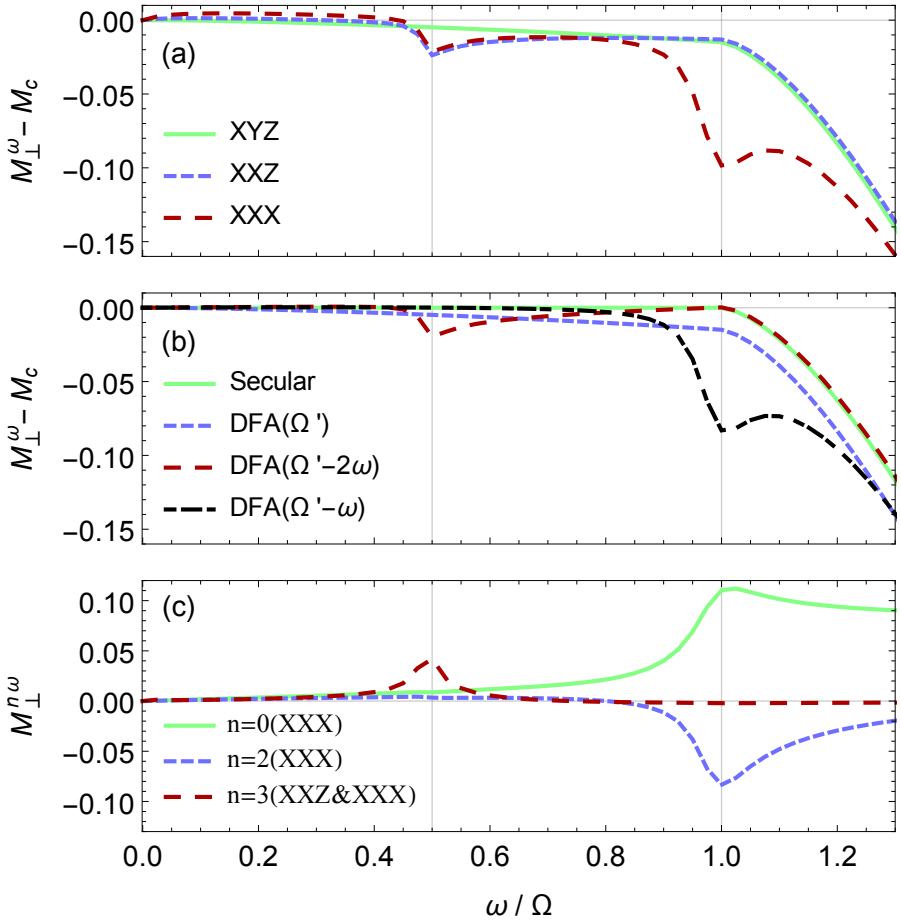

Figure 4.10: Frequency dependence and crossovers in the transverse magnetization (in units of $\frac{\Omega}{2\pi}$). In contrast to the current, the transverse magnetization oscillates with frequency ω in the $\alpha \to 0$ limit, with amplitude M_c for $\omega < \Omega$. (a) Deviation from the limiting value M_c at finite system-bath coupling, numerical solution ($\alpha = 0.1$) (b) DFA with the two dangerous frequencies and with Ω' is capable to reconstruct all the features in the numerical solution. (c) Other Fourier components of the magnetization.

4.5 Conclusion

We have investigated the fate of a spin Hall edge state, coupled to a dissipative environment, in the presence of circularly polarized electromagnetic field. Without the environment, the Floquet solution of the problem features an electromagnetic field induced photocurrent, being quantized in the adiabatic regime [195] and crossing over to dissipative charge transport with increasing frequency [186]. These results were obtained using the average energy concept for the occupation of the Floquet steady state. In the presence of dissipation, the filling of the Floquet states is determined by a Lindblad equation, which we investigated both analytically and numerically. Although in general the occupation of the Floquet states is non-thermal, depending on the microscopic details of the system-bath coupling, the occupation can be *approximately thermal* either with respect to the average energy or to the quasienergy (Figure 4.6). We found at finite system-bath coupling that non-secular terms, corresponding to 2-photon transitions, lead to a mixing of the band occupations at resonant momenta. We developed a method, the dominant frequency approximation (DFA), to describe the steady states near these resonances. In the special case of a $U(1)$ symmetric system-bath coupling, the DFA provides the exact solution of the Bloch-Redfield equations.

The photocurrent is only quantized in the strict adiabatic limit in the presence of finite bath coupling. Nevertheless, deviations from perfect quantization in the adiabatic regime are tiny, as shown in Figure 4.4, and perfect quantization is recovered in the limit of vanishing coupling to the environment. With increasing frequency, deviations grow and the photocurrent becomes dissipative in nature. Our results show that couplings to environments are essential for treating Floquet systems and that these can be identified by measuring DC as well as AC observables of the system.

5 Conclusion and thesis statements

The unifying concepts providing the pillars of this thesis are out-of-equilibrium physics and non-equilibrium phenomena. Although we have studied many different systems in various environments throughout the thesis, all of them highlight a different, relevant aspect of the non-equilibrium world. The similarities in the methods applied and the questions addressed, as well as the central role of the excitations in the various problems provide further links among the diverse studies presented in the thesis.

We provided brief conclusions of the results at the end of each part forming a logical unit, here we summarize the main results of the thesis in the thesis statements below.

Thesis statements

1. I have shown analytically on the example of the 1D quantum XY spin chain in a transverse magnetic field that dynamical phase transitions can not only show up when the non-equilibrium quench protocol connects different equilibrium phases, which was found in Ref. [Heyl et al., 2013] in the transverse Ising model, but also when the initial and final Hamiltonians characterizing the quench protocol are in the same phases. Depending on the parameters of the pre-quench Hamiltonian, I explicitly determined the domain for the post-quench parameters on the equilibrium phase diagram, where dynamical phase transitions occur.

   This result is published in paper [P1].

2. I have studied dynamical phase transitions in generic one-dimensional two-band topological insulators and topological superconductors whose topological invariants are either the winding number or the $\mathbb{Z}_2$ invariant. I have proved for this class of models that a sudden quench protocol which connects equilibrium phases characterized by different topological numbers implies the occurrence of dynamical phase transitions. Furthermore, the number of nonequilibrium timescales, which determine when the singularities appear in the time evolution, is bounded from below by the difference between the topological numbers characterizing the initial and final set of parameters. I have illustrated this finding on the example of a generalized Su-Schrieffer-Heeger model.

   These results are published in paper [P2].

3. I have studied dynamical phase transitions in two-dimensional two-band topological insulators and topological superconductors whose topological invariant is the Chern number. I have proved for this class of models that a sudden quench protocol which connects equilibrium phases characterized by Chern numbers of different absolute values implies the occurrence of dynamical phase transitions. I have also found a qualitative difference between dynamical phase transitions in 1D and 2D. While the former is characterized by jumps in the first time derivative of the dynamical free energy, in the latter case the jumps appear only in the second time derivative. I showed that this is a consequence of Fisher zeros filling areas in 2D rather than forming lines, which happens in 1D. I have illustrated these findings on the example of the Haldane honeycomb model.

   These results are published in paper [P2].

4. I have investigated Schwinger's pair creation mechanism and the non-linear response of Weyl semimetals. I have determined the full time evolution of the characteristic function of the total number of electron-hole pairs created by the electric field as well as the induced current. The distribution function of pairs crosses over from a Poissonian profile characterizing short time dynamics to a Gaussian one describing long times. The contribution of a Weyl node to the total current shows a peculiar non-monotonic behaviour: the quick initial increase of the polarization current is followed by a slow decay, which is taken over by the increasing conduction current at long times. I have demonstrated that the time evolution of the current can be translated to the conductivity of a disordered sample within a generalized Drude theory.

   These results are published in paper [P3].

5. I have determined the occupation of the Floquet quasienergy bands and the induced photocurrent in the presence of dissipation in a quantum spin Hall insulator edge irradiated by a circularly polarized light. As such, I have generalized the results of [Dóra et al., 2012], which applied the heuristic average energy concept to determine the same quantities in the absence of dissipation. I found that their prediction, that is, a transition occurs as a function of the driving frequency from a quantized to non-quantized photocurrent, remains true also in the dissipative model attached to a zero temperature heat bath, but the value of the transition frequency is lower by a factor of two in the latter treatment. Furhermore, although the occupation profile of the quasienergy bands are qualitatively similar in the two methods, the strong dependence on the bath spectral parameter is not captured by the simple average energy concept. In addition, I have developed an analytical approximate method to study the effect of photon-absorption resonances appearing at finite system-bath couplings, which lead to a further mixing of band occupations and to a weak violation of the quantization of the photocurrent in the low frequency regime.

   These results are published in paper [P4].

Publications

Publications related to thesis statements:

[P1] S. Vajna and B. Dóra, "Disentangling dynamical phase transitions from equilibrium phase transitions", Phys. Rev. B **89**, 161105(R) (2014)

[P2] S. Vajna and B. Dóra, "Topological classification of dynamical phase transitions", Phys. Rev. B **91**, 155127 (2015)

[P3] S. Vajna, B. Dóra, and R. Moessner, "Nonequilibrium transport and statistics of Schwinger pair production in Weyl semimetals", Phys. Rev. B **92**, 085122 (2015)

[P4] S. Vajna, B. Horovitz, B. Dóra, and G. Zaránd, "Floquet topological phases coupled to environments and the induced photocurrent", Phys. Rev. B **94** 115145 (2016)

Further publications:

[P5] S. Vajna, E. Simon, A. Szilva, K. Palotás, B. Ujfalussy, and L. Szunyogh, "Higher-order contributions to the Rashba-Bychkov effect with application to the Bi/Ag(111) surface alloy", Phys. Rev. B **85**, 075404 (2012)

[P6] S. Vajna, B.Tóth, and J.Kertész, "Modelling bursty time series", New J. Phys. **15** 103023 (2013)

[P7] M. Vigh, L. Oroszlány, S. Vajna, P. San-Jose, Gy. Dávid, J. Cserti, and B. Dóra "Diverging dc conductivity due to a flat band in disordered pseudospin-1 Dirac-Weyl fermions", Phys. Rev. B **88**, 161413(R) (2013)

[P8] P. Weinberg, M. Bukov, L. D'Alessio, A. Polkovnikov, S. Vajna, and M. Kolodrubetz, "Adiabatic perturbation theory and geometry of periodically-driven systems", ArXiv: 1606.02229 (2016)

References

[Heyl et al., 2013] M. Heyl, A. Polkovnikov, and S. Kehrein, "Dynamical quantum phase transitions in the transverse-field Ising model", Phys. Rev. Lett. **110**, 135704 (2013).

[Dóra et al., 2012] B. Dóra, J. Cayssol, F. Simon, and R. Moessner, "Optically engineering the topological properties of a spin Hall insulator", Phys. Rev. Lett. **108**, 056602 (2012).

6 Acknowledgements

Throughout the years of my PhD studies I have received support from many people to whom I would like to express my gratitude. First of all, I would like to thank my supervisor Dr. Balázs Dóra for coordinating my research and for being available for discussions whenever I approached him with questions. I am also grateful to him for financing my participation in countless summer schools and conferences, which not only gave me unforgettable experiences but also helped in my research. My sincere thanks also goes to Dr. Ferenc Simon, who supplemented my stipend.

I am also thankful for Dr. Gergely Zaránd for inviting me to his exotic quantum phases group, and for the enlightening discussions during our collaboration. I have also learned a lot from the insights and ideas of Baruch Horovitz and Roderich Moessner, with whom I have had the pleasure to work on some of my projects. I am also grateful to Prof. Anatoli Polkovnikov, who hosted me during my Fulbright scholarship at Boston University, as well as to Prof. Tomaž Prosen, who employed me after coming back from the US and allowed me cut out some time from the research to spend on writing my thesis.

I would also like to grab the opportunity to express my thanks to Mari Vida, without whose continuous help in administrative issues no PhD students could ever finish their studies. I also thank Gergő Fülöp for sharing the LaTeX template of his thesis with me.

Last but not the least, I would like to express my sincere gratitude to my family, especially to my wife Pálma for her continuous support throughout my PhD studies and my daughter Médea for her unparalleled love.

A Appendix

A.1 Jordan-Wigner transformation

Spin $\frac{1}{2}$ chains can be mapped to spinless fermions hopping on a lattice. The anticommutation relations of the spin ladder operators S_j^+ and S_j^- are similar to the fermion creation and annihilation operators on a single lattice site, but they commute on different sites. This can be fixed by introducing a non-local string operator, with which the Jordan-Wigner transformation reads

$$S_j^+ = c_j^+ e^{i\pi \sum_{l<j} c_l^+ c_l} \tag{A.1}$$

$$S_j^- = e^{-i\pi \sum_{l<j} c_l^+ c_l} c_j \tag{A.2}$$

$$S_j^z = c_j^+ c_j - \frac{1}{2} \tag{A.3}$$

It can be shown, that the operators c_j^+ and c_j satisfy the canonical anticommutation relations for fermions. This transformation maps the XY Hamiltonian in Eq. (2.15) to

$$\begin{aligned} H(\gamma, h) = &\sum_{j=1}^{N-1} \left\{ c_j^+ c_{j+1} + c_{j+1}^+ c_j + \gamma [c_j^+ c_{j+1}^+ + c_{j+1} c_j - 2h(c_j^+ c_j - \frac{1}{2})] \right\} \\ &- 2h(c_N^+ c_N - \frac{1}{2}) - e^{i\pi \sum_{l=1}^{N}} [c_N^+ c_1 + c_N c_1^+ + \gamma(c_N^+ c_1^+ + c_1 c_N)] \end{aligned} \tag{A.4}$$

This Hamiltonian does not conserve the total number of particles, but it conserves its parity, since particles are created and destroyed in pairs. The boundary terms can be eliminated by a proper choice of the boundary conditions: antiperiodic ($c_{N+1} \equiv -c_1$) in the even sector and periodic ($c_{N+1} \equiv c_1$) boundary conditions in the odd sector give formally the same Hamiltonian

$$H(\gamma, h) = \sum_{j=1}^{N} c_j^+ c_{j+1} + c_{j+1}^+ c_j + \gamma(c_j^+ c_{j+1}^+ + c_{j+1} c_j) - 2h(c_j^+ c_j - \frac{1}{2}) \tag{A.5}$$

for both sectors, but with different quantization for the momentum corresponding to the boundary conditions.

An additional $S_j^z S_{j+1}^z$ coupling to the XY Hamiltonian would translate to a nearest neighbor interaction for the fermions.

A.2 Non-Markovian equation

If we drop the Markovian assumption, we have to solve the integro-differential equation Eq. (4.15),

$$\dot{\rho}_S(t) = \sum_{\mu\in\{x,y,z\}} \int_0^t ds\Gamma_\mu(s)[A_\mu(t-s)\rho_S(t-s)A_\mu(t) - A_\mu(t)A_\mu(t-s)\rho_S(t-s)] + h.c, \tag{A.6}$$

or after expanding $\hat{\rho}(t) = \frac{1}{2} + \boldsymbol{\rho}(t)\cdot\boldsymbol{\sigma}$ and $\hat{A}_\mu(t) = \mathbf{a}_\mu(t)\cdot\boldsymbol{\sigma}$,

$$\frac{\mathrm{d}\boldsymbol{\rho}(t)}{\mathrm{d}t} = \int_0^t \mathrm{d}s\, \mathbf{B}(t,s)\boldsymbol{\rho}(s) + \mathbf{b}(t) \tag{A.7}$$

where

$$\mathbf{B}(t,s) = 4\,\mathrm{Re}\{\sum_\mu \Gamma_\mu(s)[\mathbf{a}_\mu(t-s)\circ\mathbf{a}_\mu(t) - \mathbb{I}\,\mathbf{a}_\mu(t-s)\cdot\mathbf{a}_\mu(t)]\} \tag{A.8}$$

$$\mathbf{b}(t) = 2\,\mathrm{Re}\{\sum_\mu \int_0^t \mathrm{d}s\,\Gamma_\mu(s) i[\mathbf{a}_\mu(t-s)\times\mathbf{a}_\mu(t)]\} \tag{A.9}$$

To test the Markovian approximation, we solved numerically the above integro-differential equation with Heun's method (a two-stage predictor-corrector method), and compared the solution with the Markovian approximation (FIG. A.1). There is a very small quantitative difference in the stationary states, but the qualitative picture does not change.

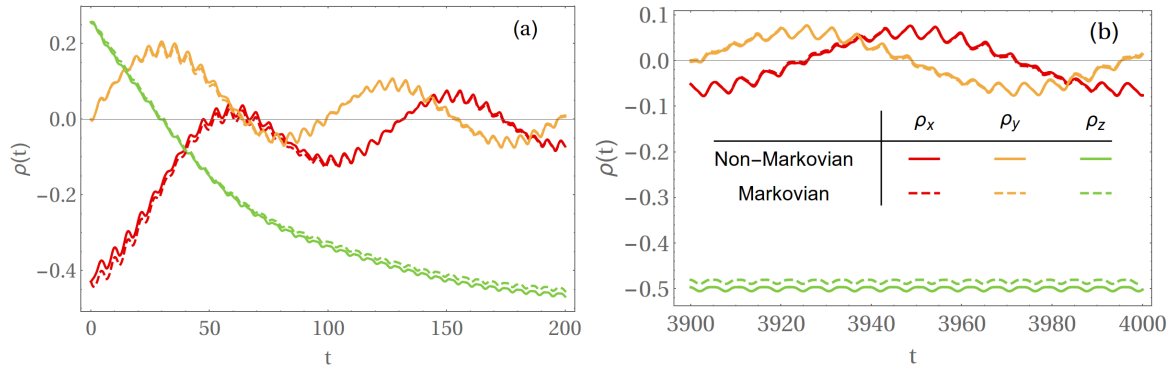

Figure A.1: Comparison of the Markovian and non-Markovian time evolution in an Ohmic environment for short (a) and long (b) times.

A.3 Expectation values in the rotated interaction picture

The Hamiltonian generating the time evolution for the whole system and environment is $\tilde{\mathcal{H}}(t) = \tilde{\mathcal{H}}_S(t) + \tilde{\mathcal{H}}_E + \tilde{\mathcal{H}}_{SE}$. We are interested in observables restricted only to the system: $[\mathcal{O}, \tilde{\mathcal{H}}_E] = 0$. In the Schrödinger picture the observables are time independent,

and the expectation values are determined by the density matrix as $\langle\mathcal{O}\rangle = \mathrm{Tr}\{\tilde{\rho}(t)\mathcal{O}\}$. The time evolution of the density matrix is given by

$$i\partial_t\tilde{\rho}(t) = [\tilde{\mathcal{H}}(t), \tilde{\rho}(t)] \tag{A.10}$$

$$\tilde{\rho}(t) = \tilde{U}\tilde{\rho}(0)\tilde{U}^\dagger \tag{A.11}$$

where $\tilde{U}$ is the time evolution operator generated by $\tilde{\mathcal{H}}(t)$. In the interaction picture we push the time evolution of the system and the environment to the operators, i.e.

$$\rho(t) = U_S^\dagger U_E^\dagger \tilde{\rho(t)} U_E U_S \tag{A.12}$$

$$i\partial_t\rho(t) = [\tilde{\mathcal{H}}_{SE}(t), \rho(t)] \tag{A.13}$$

and the expectation values are calculated as $\langle\mathcal{O}\rangle = \mathrm{Tr}\{\rho(t)U_E^\dagger U_S^\dagger \mathcal{O} U_S U_E\}$. The time evolution of the reduced density matrix of the system, $\rho'_S(t) = \mathrm{Tr}_E\{\rho(t)\}$, is given by the Bloch-Redfield equation Eq.(4.17). The expectation value of operators acting only on the system are evaluated as

$$\langle\mathcal{O}\rangle = \mathrm{Tr}\{\rho'_S(t)U_S^\dagger \mathcal{O} U_S\}\,. \tag{A.14}$$

The unitary operator $U_S(t)$ is explicitly expressed in Eq.(4.23), that is

$$U_S(t) = e^{-\frac{1}{2}i\omega t\sigma_z} U_p^\dagger e^{-\frac{1}{2}i\Omega' t\sigma_z} U_p \tag{A.15}$$

$$\tilde{U}_S(t) = e^{-\frac{1}{2}i\omega t\sigma_z} U_p^\dagger e^{-\frac{1}{2}i\Omega' t\sigma_z} \tag{A.16}$$

where $U_p = \mathrm{e}^{\frac{1}{2}i\theta\sigma_y}$ is a time-independent, but momentum dependent rotation. For convenience, we solved the time evolution of ρ'_S in the rotated frame generated by U_p, that is, $\rho_S(t) = U_p\rho'_S(t)U_p^\dagger$. Correspondingly the operators are written in the rotated interaction picture with respect to the operator $\tilde{U}_S(t)$.

$$\langle\mathcal{O}\rangle = \mathrm{Tr}\{\rho_S(t)\tilde{U}_S^\dagger \mathcal{O}\tilde{U}_S\}\,. \tag{A.17}$$

Especially for the z component of the spin operator, which determines the electric current

$$\tfrac{1}{2}\langle\sigma_z\rangle = \cos\theta\rho_z(t) - \sin\theta[\cos(\Omega' t)\rho_x(t) - \sin(\Omega' t)\rho_y(t)]\,, \tag{A.18}$$

where we used the decomposition of ρ_S in Eq.(4.27). Consequently the time average of $\langle\sigma_z\rangle$ obtains contribution from the $\pm\Omega'$ Fourier coefficients of $\rho_{x,y}(t)$, in addition to the time average of $\rho_z(t)$. The transverse operators read

$$\tfrac{1}{2}\langle\sigma_x\rangle = \sin\theta\cos(\omega t)\rho_z(t) + [\cos\theta\cos(\Omega' t)\cos(\omega t) - \sin(\Omega' t)\sin(\omega t)]\rho_x(t) - \tag{A.19}$$

$$- [\cos\theta\sin(\Omega' t)\cos(\omega t) + \cos(\Omega' t)\sin(\omega t)]\rho_y(t) \tag{A.20}$$

$$\tfrac{1}{2}\langle\sigma_y\rangle = \sin\theta\sin(\omega t)\rho_z(t) + [\cos\theta\cos(\Omega' t)\sin(\omega t) + \sin(\Omega' t)\cos(\omega t)]\rho_x(t) - \tag{A.21}$$

$$- [\cos\theta\sin(\Omega' t)\sin(\omega t) - \cos(\Omega' t)\cos(\omega t)]\rho_y(t) \tag{A.22}$$

We see that on average it describes a circular motion with frequency ω,

$$\tfrac{1}{2}\langle\sigma_x\cos(\omega t) + \sigma_y\sin(\omega t)\rangle = \sin\theta\rho_z(t) + \cos\theta[\cos(\Omega' t)\rho_x(t) - \sin(\Omega' t)\rho_y(t)]\,, \tag{A.23}$$

which is also determined by the 0^{th} Fourier component of $\rho_z(t)$ and the $\pm\Omega'$ Fourier coefficients of $\rho_{x,y}(t)$.

A.4 Matrix elements (dominant frequency approximation)

The diagonal matrix elements of $\tilde{\mathbf{B}}(0)$ and $\tilde{\mathbf{b}}(0)$ were already given in the main text. The Lamb shift η_2 is

$$\begin{aligned}\eta_2 = &-i\frac{b_z^2}{8}\big(\frac{\Omega}{\Omega'}\big)^2\left[\Gamma_z^*(-\Omega')-\Gamma_z(-\Omega')-\Gamma_z^*(\Omega')+\Gamma_z(\Omega')\right] \\ &+i\frac{b_x^2}{32}\Big\{\big(1+\frac{\omega-p}{\Omega'}\big)^2\left[\Gamma_x^*(\omega-\Omega')-\Gamma_x(\omega-\Omega')-\Gamma_x^*(\Omega'-\omega)+\Gamma_x(\Omega'-\omega)\right] \\ &\quad+\big(1-\frac{\omega-p}{\Omega'}\big)^2\left[\Gamma_x^*(-\omega-\Omega')-\Gamma_x(-\omega-\Omega')-\Gamma_x^*(\Omega'+\omega)+\Gamma_x(\Omega'+\omega)\right]\Big\} \\ &+\text{"}x\leftrightarrow y\text{"}\end{aligned} \tag{A.24}$$

for the XYZ case, and the same for the XXZ/XXX cases are given by the substitution $\Gamma_y=\Gamma_x$, $\Gamma_y=\Gamma_z=\Gamma_x$.

The Fourier component $\nu_*=\Omega'-\omega$ appears only in the XXX case, with the matrix elements

$$\begin{aligned}\chi = \frac{(b_x-ib_y)b_z}{16}&\Big\{\frac{\omega-p}{\Omega'}\big(1+\frac{\omega-p}{\Omega'}\big)\left[\Gamma_x(\Omega'-\omega)-\Gamma_x^*(\omega-\Omega')+\Gamma_x^*(0)-\Gamma_x(0)\right] \\ &-\frac{\Omega^2}{\Omega'^2}\left[\Gamma_x^*(\omega)-\Gamma_x(-\omega)+\Gamma_x^*(\Omega')-\Gamma_x(-\Omega')\right]\Big\}\end{aligned} \tag{A.25}$$

$$\begin{aligned}\beta_1 = \frac{(b_x-ib_y)b_z}{8}&\Big\{\frac{\omega-p}{\Omega'}\big(1+\frac{\omega-p}{\Omega'}\big)\left[\Gamma_x(\Omega'-\omega)+\Gamma_x^*(\omega-\Omega')\right] \\ &-\frac{\Omega^2}{\Omega'^2}\left[\Gamma_x(\Omega')+\Gamma_x^*(-\Omega')\right]\Big\}\end{aligned} \tag{A.26}$$

$$\beta_2 = \frac{(b_x-ib_y)b_z}{8}\Big\{\frac{\omega-p}{\Omega'}\big(1+\frac{\omega-p}{\Omega'}\big)\left[\Gamma_x^*(0)+\Gamma_x(0)\right]-\frac{\Omega^2}{\Omega'^2}\left[\Gamma_x^*(\omega)+\Gamma_x(-\omega)\right]\Big\} \tag{A.27}$$

$$\delta = \frac{(b_x-ib_y)^2}{32}\big(1+\frac{\omega-p}{\Omega'}\big)^2\left[\Gamma_x(\Omega'-\omega)+\Gamma_x^*(\omega-\Omega')\right] \tag{A.28}$$

but the second harmonic $2\nu_*$ is present in the XXZ and XYZ cases as well. In the former δ is identical to that of the XXX case, while for the latter

$$\delta = \frac{b_x^2}{32}\big(1+\frac{\omega-p}{\Omega'}\big)^2\left[\Gamma_x(\Omega'-\omega)+\Gamma_x^*(\omega-\Omega')\right]-\text{"}x\leftrightarrow y\text{"} \tag{A.29}$$

In the case of Fourier component $\nu_{**}=\Omega'-2\omega$ the second harmonic $\delta\equiv 0$ in all the coupling schemes. The other matrix elements are

$$\chi = \frac{b_x^2}{32}\frac{\Omega}{\Omega'}\big(1+\frac{\omega-p}{\Omega'}\big)\left[\Gamma_x^*(\omega)-\Gamma_x(-\omega)+\Gamma_x(\Omega'-\omega)-\Gamma_x^*(\omega-\Omega')\right]-\text{"}x\leftrightarrow y\text{"} \tag{A.30}$$

$$\beta_1 = \frac{b_x^2}{16}\frac{\Omega}{\Omega'}\big(1+\frac{\omega-p}{\Omega'}\big)\left[\Gamma_x(\Omega'-\omega)+\Gamma_x^*(\omega-\Omega')\right]-\text{"}x\leftrightarrow y\text{"} \tag{A.31}$$

$$\beta_2 = \frac{b_x^2}{16}\frac{\Omega}{\Omega'}\big(1+\frac{\omega-p}{\Omega'}\big)\left[\Gamma_x^*(\omega)+\Gamma_x(-\omega)\right]-\text{"}x\leftrightarrow y\text{"} \tag{A.32}$$

for the XYZ case, and

$$\chi = \frac{(b_x - ib_y)^2}{32}\frac{\Omega}{\Omega'}\big(1+\frac{\omega-p}{\Omega'}\big)\left[\Gamma_x^*(\omega) - \Gamma_x(-\omega) + \Gamma_x(\Omega'-\omega) - \Gamma_x^*(\omega-\Omega')\right] \tag{A.33}$$

$$\beta_1 = \frac{(b_x - ib_y)^2}{16}\frac{\Omega}{\Omega'}\big(1+\frac{\omega-p}{\Omega'}\big)\left[\Gamma_x(\Omega'-\omega) + \Gamma_x^*(\omega-\Omega')\right] \tag{A.34}$$

$$\beta_2 = \frac{(b_x - ib_y)^2}{16}\frac{\Omega}{\Omega'}\big(1+\frac{\omega-p}{\Omega'}\big)\left[\Gamma_x^*(\omega) + \Gamma_x(-\omega)\right] \tag{A.35}$$

for the XXZ and XXX cases.

The matrix elements of the Fourier coefficients Ω' in the XYZ are

$$\begin{aligned}\chi = \quad & \frac{b_z^2}{8}\frac{\Omega}{\Omega'}\frac{\omega-p}{\Omega'}\left[\Gamma_z(0) - \Gamma_z^*(0) - \Gamma_z(\Omega') + \Gamma_z^*(-\Omega)\right] \\ & + \frac{b_x^2}{32}\frac{\Omega}{\Omega'}\Big\{\big(1+\frac{\omega-p}{\Omega'}\big)\left[-\Gamma_x(\omega) + \Gamma_x^*(-\omega) + \Gamma_x(\Omega'-\omega) - \Gamma_x^*(\omega-\Omega')\right] + \\ & \qquad + \big(1-\frac{\omega-p}{\Omega'}\big)\left[-\Gamma_x^*(\omega) + \Gamma_x(-\omega) + \Gamma_x^*(-\Omega'-\omega) - \Gamma_x(\Omega'+\omega)\right]\Big\} + \text{"}x \leftrightarrow y\text{"}\end{aligned} \tag{A.36}$$

$$\begin{aligned}\beta_1 = & -\frac{b_z^2}{4}\frac{\Omega}{\Omega'}\frac{\omega-p}{\Omega'}\left[\Gamma_z(\Omega') + \Gamma_z^*(-\Omega')\right] \\ & + \frac{b_x^2}{16}\frac{\Omega}{\Omega'}\Big\{\big(1+\frac{\omega-p}{\Omega'}\big)\left[\Gamma_x(\Omega'-\omega) + \Gamma_x^*(\omega-\Omega')\right] \\ & \qquad -\big(1-\frac{\omega-p}{\Omega'}\big)\left[\Gamma_x(\Omega'+\omega) + \Gamma_x^*(-\omega-\Omega')\right]\Big\} + \text{"}x \leftrightarrow y\text{"}\end{aligned} \tag{A.37}$$

$$\begin{aligned}\beta_2 = & -\frac{b_z^2}{4}\frac{\Omega}{\Omega'}\frac{\omega-p}{\Omega'}\left[\Gamma_z(0) + \Gamma_z^*(0)\right] \\ & + \frac{b_x^2}{16}\frac{\Omega}{\Omega'}\Big\{\big(1+\frac{\omega-p}{\Omega'}\big)\left[\Gamma_x(\omega) + \Gamma_x^*(-\omega)\right] \\ & \qquad - \big(1-\frac{\omega-p}{\Omega'}\big)\left[\Gamma_x(-\omega) + \Gamma_x^*(\omega)\right]\Big\} + \text{"}x \leftrightarrow y\text{"}\end{aligned} \tag{A.38}$$

$$\begin{aligned}\delta = \quad & \frac{b_z^2}{8}\frac{\Omega^2}{\Omega'^2}\left[\Gamma_z(\Omega') + \Gamma_z^*(-\Omega)\right] \\ & + \frac{b_x^2}{32}\Big[\big(\frac{\omega-p}{\Omega'}\big)^2 - 1\Big]\left[\Gamma_x(\Omega'+\omega) + \Gamma_x(\Omega'-\omega) + \Gamma_x^*(\omega-\Omega') + \Gamma_x^*(-\omega-\Omega')\right] \\ & + \text{"}x \leftrightarrow y\text{"}\end{aligned} \tag{A.39}$$

and the same for the XXZ and XXX cases are given by the substitution $\Gamma_y = \Gamma_x$ and $\Gamma_y = \Gamma_z = \Gamma_x$, respectively.

B Bibliography

[1] A. Polkovnikov, K. Sengupta, A. Silva, and M. Vengalattore, "*Colloquium* : Nonequilibrium dynamics of closed interacting quantum systems," Rev. Mod. Phys. **83**, 863 (2011).

[2] J. Eisert, M. Friesdorf, and C. Gogolin, "Quantum many-body systems out of equilibrium," Nature Physics **11**, 124 (2015).

[3] J. v. Neumann, "Beweis des ergodensatzes und desh-theorems in der neuen mechanik," Zeitschrift für Physik **57**, 30 (1929).

[4] I. Bloch, "Ultracold quantum gases in optical lattices," Nature Physics **1**, 23 (2005).

[5] I. Bloch, J. Dalibard, and W. Zwerger, "Many-body physics with ultracold gases," Rev. Mod. Phys. **80**, 885 (2008).

[6] C. Jarzynski, "Nonequilibrium equality for free energy differences," Phys. Rev. Lett. **78**, 2690 (1997).

[7] G. E. Crooks, "Entropy production fluctuation theorem and the nonequilibrium work relation for free energy differences," Phys. Rev. E **60**, 2721 (1999).

[8] M. Campisi, P. Hänggi, and P. Talkner, "*Colloquium*: Quantum fluctuation relations: Foundations and applications," Rev. Mod. Phys. **83**, 771 (2011).

[9] M. Rigol, V. Dunjko, and M. Olshanii, "Thermalization and its mechanism for generic isolated quantum systems," Nature **452**, 854 (2008).

[10] M. Rigol, V. Dunjko, V. Yurovsky, and M. Olshanii, "Relaxation in a completely integrable many-body quantum system: An *Ab Initio* study of the dynamics of the highly excited states of 1d lattice hard-core bosons," Phys. Rev. Lett. **98**, 050405 (2007).

[11] A. Shnirman and I. Kamleitner, "Physics of Quantum Information, Lecture notes (unpublished)".

[12] W. Van Dam, "Quantum computing: In the'death zone'?," Nature Physics **3**, 220 (2007).

[13] E. Farhi, J. Goldstone, S. Gutmann, and M. Sipser, "Quantum Computation by Adiabatic Evolution," ArXiv e-prints (2000), quant-ph/0001106.

[14] P. Doria, T. Calarco, and S. Montangero, "Optimal control technique for many-body quantum dynamics," Phys. Rev. Lett. **106**, 190501 (2011).

[15] A. Rahmani and C. Chamon, "Optimal control for unitary preparation of many-body states: Application to luttinger liquids," Phys. Rev. Lett. **107**, 016402 (2011).

[16] M. G. Bason, M. Viteau, N. Malossi, P. Huillery, E. Arimondo, D. Ciampini, R. Fazio, V. Giovannetti, R. Mannella, and O. Morsch, "High-fidelity quantum driving," Nature Physics **8**, 147 (2012).

[17] E. Torrontegui, S. Ibáñez, S. Martínez-Garaot, M. Modugno, A. del Campo, D. Guéry-Odelin, A. Ruschhaupt, X. Chen, and J. G. Muga, "Shortcuts to Adiabaticity," Advances in Atomic Molecular and Optical Physics **62**, 117 (2013).

[18] S. Vajna and B. Dóra, "Disentangling dynamical phase transitions from equilibrium phase transitions," Phys. Rev. B **89**, 161105 (2014).

[19] S. Vajna and B. Dóra, "Topological classification of dynamical phase transitions," Phys. Rev. B **91**, 155127 (2015).

[20] S. Vajna, B. Dóra, and R. Moessner, "Nonequilibrium transport and statistics of schwinger pair production in Weyl semimetals," Phys. Rev. B **92**, 085122 (2015).

[21] S. Vajna, B. Horovitz, B. Dóra, and G. Zaránd, "Floquet topological phases coupled to environments and the induced photocurrent," Phys. Rev. B **94**, 115145 (2016).

[22] G. Gallavotti, *Statistical mechanics: A short treatise* (Springer Science & Business Media, 2013).

[23] J. M. Deutsch, "Quantum statistical mechanics in a closed system," Phys. Rev. A **43**, 2046 (1991).

[24] M. Srednicki, "Chaos and quantum thermalization," Phys. Rev. E **50**, 888 (1994).

[25] A. Silva, "Statistics of the work done on a quantum critical system by quenching a control parameter," Phys. Rev. Lett. **101**, 120603 (2008).

[26] F. M. Cucchietti, C. H. Lewenkopf, E. R. Mucciolo, H. M. Pastawski, and R. O. Vallejos, "Measuring the Lyapunov exponent using quantum mechanics," Phys. Rev. E **65**, 046209 (2002).

[27] F. M. Cucchietti, D. A. R. Dalvit, J. P. Paz, and W. H. Zurek, "Decoherence and the Loschmidt echo," Phys. Rev. Lett. **91**, 210403 (2003).

[28] A. C. Cassidy, C. W. Clark, and M. Rigol, "Generalized thermalization in an integrable lattice system," Phys. Rev. Lett. **106**, 140405 (2011).

[29] B. Wouters, J. De Nardis, M. Brockmann, D. Fioretto, M. Rigol, and J.-S. Caux, "Quenching the anisotropic Heisenberg chain: Exact solution and generalized Gibbs ensemble predictions," Phys. Rev. Lett. **113**, 117202 (2014).

[30] B. Pozsgay, M. Mestyán, M. A. Werner, M. Kormos, G. Zaránd, and G. Takács, "Correlations after quantum quenches in the XXZ spin chain: Failure of the generalized Gibbs ensemble," Phys. Rev. Lett. **113**, 117203 (2014).

[31] G. Goldstein and N. Andrei, "Failure of the local generalized Gibbs ensemble for integrable models with bound states," Phys. Rev. A **90**, 043625 (2014).

[32] E. Ilievski, J. De Nardis, B. Wouters, J.-S. Caux, F. H. L. Essler, and T. Prosen, "Complete generalized Gibbs ensembles in an interacting theory," Phys. Rev. Lett. **115**, 157201 (2015).

[33] R. Nandkishore and D. A. Huse, "Many-body localization and thermalization in quantum statistical mechanics," Annual Review of Condensed Matter Physics **6**, 15 (2015).

[34] A. Lazarides, A. Das, and R. Moessner, "Periodic thermodynamics of isolated quantum systems," Phys. Rev. Lett. **112**, 150401 (2014).

[35] A. Lazarides, A. Das, and R. Moessner, "Equilibrium states of generic quantum systems subject to periodic driving," Phys. Rev. E **90**, 012110 (2014).

[36] L. D'Alessio and M. Rigol, "Long-time behavior of isolated periodically driven interacting lattice systems," Phys. Rev. X **4**, 041048 (2014).

[37] P. Ponte, A. Chandran, Z. Papić, and D. A. Abanin, "Periodically driven ergodic and many-body localized quantum systems," Annals of Physics **353**, 196 (2015).

[38] H. Sambe, "Steady states and quasienergies of a quantum-mechanical system in an oscillating field," Phys. Rev. A **7**, 2203 (1973).

[39] T. Dittrich, P. Hanggi, G.-L. Ingold, B. Kramer, G. Schon, and W. Zwerger, eds., *Quantum Transport and Dissipation* (Wiley-WCH, 1998).

[40] M. Bukov, L. D'Alessio, and A. Polkovnikov, "Universal high-frequency behavior of periodically driven systems: from dynamical stabilization to Floquet engineering," Advances in Physics **64**, 139 (2015).

[41] W. Magnus, "On the exponential solution of differential equations for a linear operator," Communications on Pure and Applied Mathematics **7**, 649 (1954).

[42] S. Blanes, F. Casas, J. Oteo, and J. Ros, "The Magnus expansion and some of its applications," Physics Reports **470**, 151 (2009).

[43] M. Aidelsburger, M. Atala, M. Lohse, J. T. Barreiro, B. Paredes, and I. Bloch, "Realization of the Hofstadter Hamiltonian with ultracold atoms in optical lattices," Phys. Rev. Lett. **111**, 185301 (2013).

[44] H. Miyake, G. A. Siviloglou, C. J. Kennedy, W. C. Burton, and W. Ketterle, "Realizing the Harper Hamiltonian with laser-assisted tunneling in optical lattices," Phys. Rev. Lett. **111**, 185302 (2013).

[45] M. Atala, M. Aidelsburger, M. Lohse, J. T. Barreiro, B. Paredes, and I. Bloch, "Observation of chiral currents with ultracold atoms in bosonic ladders," Nature Physics **10**, 588 (2014).

[46] G. Jotzu, M. Messer, R. Desbuquois, M. Lebrat, T. Uehlinger, D. Greif, and T. Esslinger, "Experimental realization of the topological Haldane model with ultracold fermions," Nature **515**, 237 (2014).

[47] M. C. Rechtsman, J. M. Zeuner, Y. Plotnik, Y. Lumer, D. Podolsky, F. Dreisow, S. Nolte, M. Segev, and A. Szameit, "Photonic Floquet topological insulators," Nature **496**, 196 (2013).

[48] N. H. Lindner, G. Refael, and V. Galitski, "Floquet topological insulator in semiconductor quantum wells," Nature Physics **7**, 490 (2011).

[49] T. Kitagawa, T. Oka, A. Brataas, L. Fu, and E. Demler, "Transport properties of nonequilibrium systems under the application of light: Photoinduced quantum Hall insulators without Landau levels," Phys. Rev. B **84**, 235108 (2011).

[50] R. Grimm, M. Weidemüller, and Y. B. Ovchinnikov, "Optical dipole traps for neutral atoms," Advances in Atomic Molecular and Optical Physics **42**, 95 (2000).

[51] E. Haller, J. Hudson, A. Kelly, D. A. Cotta, B. Peaudecerf, G. D. Bruce, and S. Kuhr, "Single-atom imaging of fermions in a quantum-gas microscope," Nature Physics **11**, 738 (2015).

[52] W. S. Bakr, J. I. Gillen, A. Peng, S. Fölling, and M. Greiner, "A quantum gas microscope for detecting single atoms in a Hubbard-regime optical lattice," Nature **462**, 74 (2009).

[53] M. Z. Hasan and C. L. Kane, "*Colloquium* : Topological insulators," Rev. Mod. Phys. **82**, 3045 (2010).

[54] K. v. Klitzing, G. Dorda, and M. Pepper, "New method for high-accuracy determination of the fine-structure constant based on quantized Hall resistance," Phys. Rev. Lett. **45**, 494 (1980).

[55] D. J. Thouless, M. Kohmoto, M. P. Nightingale, and M. den Nijs, "Quantized Hall conductance in a two-dimensional periodic potential," Phys. Rev. Lett. **49**, 405 (1982).

[56] F. D. M. Haldane, "Model for a quantum Hall effect without landau levels: Condensed-matter realization of the "parity anomaly"," Phys. Rev. Lett. **61**, 2015 (1988).

[57] C. L. Kane and E. J. Mele, "Quantum spin Hall effect in graphene," Phys. Rev. Lett. **95**, 226801 (2005).

[58] M. König, S. Wiedmann, C. Brüne, A. Roth, H. Buhmann, L. W. Molenkamp, X.-L. Qi, and S.-C. Zhang, "Quantum spin Hall insulator state in HgTe quantum wells," Science **318**, 766 (2007).

[59] X.-L. Qi and S.-C. Zhang, "The quantum spin Hall effect and topological insulators," Physics Today **63**, 33 (2010), ArXiv e-print: 1001.1602.

[60] V. Mourik, K. Zuo, S. M. Frolov, S. R. Plissard, E. P. A. M. Bakkers, and L. P. Kouwenhoven, "Signatures of Majorana fermions in hybrid superconductor-semiconductor nanowire devices," Science **336**, 1003 (2012).

[61] S. Nadj-Perge, I. K. Drozdov, J. Li, H. Chen, S. Jeon, J. Seo, A. H. MacDonald, B. A. Bernevig, and A. Yazdani, "Observation of Majorana fermions in ferromagnetic atomic chains on a superconductor," Science **346**, 602 (2014).

[62] Z. Wang, H. Weng, Q. Wu, X. Dai, and Z. Fang, "Three-dimensional Dirac semimetal and quantum transport in Cd_3As_2," Phys. Rev. B **88**, 125427 (2013).

[63] J. Klinder, H. Keßler, M. Wolke, L. Mathey, and A. Hemmerich, "Dynamical phase transition in the open Dicke model," Proceedings of the National Academy of Sciences **112**, 3290 (2015).

[64] S. Iyer, V. Oganesyan, G. Refael, and D. A. Huse, "Many-body localization in a quasiperiodic system," Phys. Rev. B **87**, 134202 (2013).

[65] M. Eckstein, M. Kollar, and P. Werner, "Thermalization after an interaction quench in the Hubbard model," Phys. Rev. Lett. **103**, 056403 (2009).

[66] B. Sciolla and G. Biroli, "Dynamical transitions and quantum quenches in mean-field models," Journal of Statistical Mechanics: Theory and Experiment **2011**, P11003 (2011).

[67] B. Sciolla and G. Biroli, "Quantum quenches, dynamical transitions, and off-equilibrium quantum criticality," Phys. Rev. B **88**, 201110 (2013).

[68] M. Heyl, A. Polkovnikov, and S. Kehrein, "Dynamical quantum phase transitions in the transverse-field Ising model," Phys. Rev. Lett. **110**, 135704 (2013).

[69] C. Karrasch and D. Schuricht, "Dynamical phase transitions after quenches in non-integrable models," Phys. Rev. B **87**, 195104 (2013).

[70] J. M. Hickey, S. Genway, and J. P. Garrahan, "Dynamical phase transitions, time-integrated observables, and geometry of states," Phys. Rev. B **89**, 054301 (2014).

[71] F. Andraschko and J. Sirker, "Dynamical quantum phase transitions and the Loschmidt echo: A transfer matrix approach," Phys. Rev. B **89**, 125120 (2014).

[72] J. N. Kriel, C. Karrasch, and S. Kehrein, "Dynamical quantum phase transitions in the axial next-nearest-neighbor Ising chain," Phys. Rev. B **90**, 125106 (2014).

[73] J. M. Hickey, "Timescales, dynamical phase transitions and 3rd order phase transitions in the 1d anisotropic XY model," ArXiv e-prints (2014), 1403.5515.

[74] E. Canovi, P. Werner, and M. Eckstein, "First-order dynamical phase transitions," Phys. Rev. Lett. **113**, 265702 (2014).

[75] M. Heyl, "Dynamical quantum phase transitions in systems with broken-symmetry phases," Phys. Rev. Lett. **113**, 205701 (2014).

[76] M. Heyl, "Scaling and universality at dynamical quantum phase transitions," Phys. Rev. Lett. **115**, 140602 (2015).

[77] M. Schmitt and S. Kehrein, "Dynamical quantum phase transitions in the Kitaev honeycomb model," Phys. Rev. B **92**, 075114 (2015).

[78] S. Sharma, S. Suzuki, and A. Dutta, "Quenches and dynamical phase transitions in a nonintegrable quantum Ising model," Phys. Rev. B **92**, 104306 (2015).

[79] T. Palmai, "Edge exponents in work statistics out of equilibrium and dynamical phase transitions from scattering theory in one-dimensional gapped systems," Phys. Rev. B **92**, 235433 (2015).

[80] J. C. Budich and M. Heyl, "Dynamical topological order parameters far from equilibrium," Phys. Rev. B **93**, 085416 (2016).

[81] N. O. Abeling and S. Kehrein, "Quantum quench dynamics in the transverse field Ising model at nonzero temperatures," Phys. Rev. B **93**, 104302 (2016).

[82] S. Sharma, U. Divakaran, A. Polkovnikov, and A. Dutta, "Slow quenches in a quantum Ising chain: Dynamical phase transitions and topology," Phys. Rev. B **93**, 144306 (2016).

[83] U. Divakaran, S. Sharma, and A. Dutta, "Tuning the presence of dynamical phase transitions in a generalized XY spin chain," Phys. Rev. E **93**, 052133 (2016).

[84] B. Žunkovič, A. Silva, and M. Fabrizio, "Dynamical phase transitions and Loschmidt echo in the infinite-range XY model," Philosophical Transactions of the Royal Society of London A: Mathematical, Physical and Engineering Sciences **374** (2016).

[85] T. Puskarov and D. Schuricht, "Time evolution during and after finite-time quantum quenches in the transverse-field Ising chain," SciPost Phys. **1**, 003 (2016).

[86] M. Heyl, "Quenching a quantum critical state by the order parameter: Dynamical quantum phase transitions and quantum speed limits," ArXiv e-prints (2016), 1608.06659.

[87] M. Azimi, M. Sekania, S. K. Mishra, L. Chotorlishvili, Z. Toklikishvili, and J. Berakdar, "Pulse and quench induced dynamical phase transition in a chiral multiferroic spin chain," Phys. Rev. B **94**, 064423 (2016).

[88] Z. Huang and A. V. Balatsky, "Dynamical quantum phase transitions: Role of topological nodes in wave function overlaps," Phys. Rev. Lett. **117**, 086802 (2016).

[89] B. Zunkovic, M. Heyl, M. Knap, and A. Silva, "Dynamical quantum phase transitions in spin chains with long-range interactions: Merging different concepts of non-equilibrium criticality," ArXiv e-prints (2016), 1609.08482.

[90] U. Bhattacharya and A. Dutta, "Interconnections between equilibrium topology and dynamical quantum phase transitions: a linearly ramped Haldane model," ArXiv e-prints (2016), 1610.02674.

[91] U. Bhattacharya and A. Dutta, "Emergent topology and dynamical quantum phase transitions in two-dimensional closed quantum systems," ArXiv e-prints (2017), 1701.03911.

[92] C. Karrasch and D. Schuricht, "Dynamical quantum phase transitions in the quantum Potts chain," ArXiv e-prints (2017), 1701.04214.

[93] N. Fläschner, D. Vogel, M. Tarnowski, B. S. Rem, D.-S. Lühmann, M. Heyl, J. C. Budich, L. Mathey, K. Sengstock, and C. Weitenberg, "Observation of a dynamical topological phase transition," ArXiv e-prints (2016), 1608.05616.

[94] A. B. Khanikaev, S. H. Mousavi, W.-K. Tse, M. Kargarian, A. H. MacDonald, and G. Shvets, "Photonic topological insulators," Nature materials **12**, 233 (2013).

[95] A. LeClair, G. Mussardo, H. Saleur, and S. Skorik, "Boundary energy and boundary states in integrable quantum field theories," Nuclear Physics B **453**, 581 (1995).

[96] H. T. Quan, Z. Song, X. F. Liu, P. Zanardi, and C. P. Sun, "Decay of Loschmidt echo enhanced by quantum criticality," Phys. Rev. Lett. **96**, 140604 (2006).

[97] P. Zanardi, H. T. Quan, X. Wang, and C. P. Sun, "Mixed-state fidelity and quantum criticality at finite temperature," Phys. Rev. A **75**, 032109 (2007).

[98] N. T. Jacobson, L. C. Venuti, and P. Zanardi, "Unitary equilibration after a quantum quench of a thermal state," Phys. Rev. A **84**, 022115 (2011).

[99] B. Pozsgay, "The dynamical free energy and the Loschmidt echo for a class of quantum quenches in the Heisenberg spin chain," Journal of Statistical Mechanics: Theory and Experiment **10**, 10028 (2013), 1308.3087.

[100] P. W. Anderson, "Infrared catastrophe in Fermi gases with local scattering potentials," Phys. Rev. Lett. **18**, 1049 (1967).

[101] B. Dóra, F. Pollmann, J. Fortágh, and G. Zaránd, "Loschmidt echo and the many-body orthogonality catastrophe in a qubit-coupled Luttinger liquid," Phys. Rev. Lett. **111**, 046402 (2013).

[102] T. B. Batalhão, A. M. Souza, L. Mazzola, R. Auccaise, R. S. Sarthour, I. S. Oliveira, J. Goold, G. De Chiara, M. Paternostro, and R. M. Serra, "Experimental reconstruction of work distribution and study of fluctuation relations in a closed quantum system," Phys. Rev. Lett. **113**, 140601 (2014).

[103] F. Pollmann, S. Mukerjee, A. G. Green, and J. E. Moore, "Dynamics after a sweep through a quantum critical point," Phys. Rev. E **81**, 020101 (2010).

[104] M. Fagotti, "Dynamical phase transitions as properties of the stationary state: Analytic results after quantum quenches in the spin-1/2 XXZ chain," ArXiv e-prints (2013), 1308.0277.

[105] M. E. Fisher, in *Boulder Lectures in Theoretical Physics* ("University of Colorado", Boulder, 1965), vol. 453.

[106] W. van Saarloos and D. A. Kurtze, "Location of zeros in the complex temperature plane: absence of Lee-Yang theorem," Journal of Physics A: Mathematical and General **17**, 1301 (1984).

[107] W. Janke and R. Kenna, "The strength of first and second order phase transitions from partition function zeroes," Journal of Statistical Physics **102**, 1211 (2001).

[108] C. Itzykson, R. Pearson, and J. Zuber, "Distribution of zeros in Ising and gauge models," Nuclear Physics B **220**, 415 (1983).

[109] R. Blythe and M. Evans, "The Lee-Yang theory of equilibrium and nonequilibrium phase transitions," Brazilian Journal of Physics **33**, 464 (2003).

[110] R. J. Baxter, *Exactly solved models in statistical mechanics* (Academic Press, 1982).

[111] F. Franchini, "Notes on Bethe ansatz techniques," International School for Advanced Studies-Trieste, Lecture Notes (2011).

[112] P. Calabrese, F. H. L. Essler, and M. Fagotti, "Quantum quench in the transverse field Ising chain: I. time evolution of order parameter correlators," Journal of Statistical Mechanics: Theory and Experiment **7**, 16 (2012).

[113] M. Abramowitz and I. A. Stegun, "Handbook of mathematical functions with formulas, graphs, and mathematical tables," (1972).

[114] E. Barouch and B. M. McCoy, "Statistical mechanics of the XY model. II. spin-correlation functions," Phys. Rev. A **3**, 786 (1971).

[115] A. Y. Kitaev, "Unpaired Majorana fermions in quantum wires," Physics-Uspekhi **44**, 131 (2001).

[116] S. D. Sarma, M. Freedman, and C. Nayak, "Majorana zero modes and topological quantum computation," npj Quantum Mechanics **1**, 15001 (2015).

[117] M. Atala, M. Aidelsburger, J. T. Barreiro, D. Abanin, T. Kitagawa, E. Demler, and I. Bloch, "Direct measurement of the Zak phase in topological Bloch bands," Nature Physics **9**, 795 (2013).

[118] S. Ryu, A. P. Schnyder, A. Furusaki, and A. W. W. Ludwig, "Topological insulators and superconductors: tenfold way and dimensional hierarchy," New Journal of Physics **12**, 065010 (2010).

[119] Y. Niu, S. B. Chung, C.-H. Hsu, I. Mandal, S. Raghu, and S. Chakravarty, "Majorana zero modes in a quantum Ising chain with longer-ranged interactions," Phys. Rev. B **85**, 035110 (2012).

[120] M. P. L. Heyl, Ph.D. thesis, lmu (2012).

[121] S. Ryu and Y. Hatsugai, "Topological origin of zero-energy edge states in particle-hole symmetric systems," Phys. Rev. Lett. **89**, 077002 (2002).

[122] S. Mao, A. Yamakage, and Y. Kuramoto, "Tight-binding model for topological insulators: Analysis of helical surface modes over the whole brillouin zone," Phys. Rev. B **84**, 115413 (2011).

[123] X.-L. Qi, Y.-S. Wu, and S.-C. Zhang, "Topological quantization of the spin Hall effect in two-dimensional paramagnetic semiconductors," Phys. Rev. B **74**, 085308 (2006).

[124] M. Nakahara, *Geometry, topology and physics* (CRC Press, 2003).

[125] R. Horodecki, P. Horodecki, M. Horodecki, and K. Horodecki, "Quantum entanglement," Rev. Mod. Phys. **81**, 865 (2009).

[126] H.-C. Jiang, Z. Wang, and L. Balents, "Identifying topological order by entanglement entropy," Nature Physics **8**, 902 (2012).

[127] H. Li and F. D. M. Haldane, "Entanglement spectrum as a generalization of entanglement entropy: Identification of topological order in non-Abelian fractional quantum Hall effect states," Phys. Rev. Lett. **101**, 010504 (2008).

[128] M.-C. Chung, Y.-H. Jhu, P. Chen, and C.-Y. Mou, "Quench dynamics of topological maximally entangled states," Journal of Physics: Condensed Matter **25**, 285601 (2013).

[129] M.-C. Chung, Y.-H. Jhu, P. Chen, C.-Y. Mou, and X. Wan, "A memory of Majorana fermions through quantum quench," ArXiv e-prints (2014), 1401.0433.

[130] W. P. Su, J. R. Schrieffer, and A. J. Heeger, "Solitons in polyacetylene," Phys. Rev. Lett. **42**, 1698 (1979).

[131] T. Obuchi and K. Takahashi, "Dynamical singularities of glassy systems in a quantum quench," Phys. Rev. E **86**, 051125 (2012).

[132] K. Takahashi and T. Obuchi, "Zeros of the partition function and dynamical singularities in spin-glass systems," Journal of Physics: Conference Series **473**, 012023 (2013).

[133] B. A. Bernevig, T. L. Hughes, and S.-C. Zhang, "Quantum spin Hall effect and topological phase transition in HgTe quantum wells," Science **314**, 1757 (2006).

[134] A. Bühler, N. Lang, C. V. Kraus, G. Möller, S. D. Huber, and H. P. Büchler, "Majorana modes and p-wave superfluids for fermionic atoms in optical lattices," Nature Communications **5**, 4504 (2014).

[135] B. Jeckelmann and B. Jeanneret, "The quantum hall effect as an electrical resistance standard," Reports on Progress in Physics **64**, 1603 (2001).

[136] X. Wan, A. M. Turner, A. Vishwanath, and S. Y. Savrasov, "Topological semimetal and Fermi-arc surface states in the electronic structure of pyrochlore iridates," Phys. Rev. B **83**, 205101 (2011).

[137] A. A. Burkov and L. Balents, "Weyl semimetal in a topological insulator multilayer," Phys. Rev. Lett. **107**, 127205 (2011).

[138] P. Hosur, S. A. Parameswaran, and A. Vishwanath, "Charge transport in Weyl semimetals," Phys. Rev. Lett. **108**, 046602 (2012).

[139] A. A. Burkov, "Chiral anomaly and transport in Weyl metals," Journal of Physics: Condensed Matter **27**, 113201 (2015).

[140] J. Schwinger, "On gauge invariance and vacuum polarization," Phys. Rev. **82**, 664 (1951).

[141] A. Polkovnikov, "Universal adiabatic dynamics in the vicinity of a quantum critical point," Phys. Rev. B **72**, 161201 (2005).

[142] W. H. Zurek, U. Dorner, and P. Zoller, "Dynamics of a quantum phase transition," Phys. Rev. Lett. **95**, 105701 (2005).

[143] B. Damski and W. H. Zurek, "Adiabatic-impulse approximation for avoided level crossings: From phase-transition dynamics to Landau-Zener evolutions and back again," Phys. Rev. A **73**, 063405 (2006).

[144] L. Tarruell, D. Greif, T. Uehlinger, G. Jotzu, and T. Esslinger, "Creating, moving and merging Dirac points with a Fermi gas in a tunable honeycomb lattice," Nature **483**, 302 (2012).

[145] W.-Y. He, S. Zhang, and K. T. Law, "Realization and detection of Weyl semimetals and the chiral anomaly in cold atomic systems," Phys. Rev. A **94**, 013606 (2016).

[146] Y. V. Nazarov, *Quantum Noise in Mesoscopic Physics* (Springer, 2003).

[147] M. Esposito, U. Harbola, and S. Mukamel, "Nonequilibrium fluctuations, fluctuation theorems, and counting statistics in quantum systems," Rev. Mod. Phys. **81**, 1665 (2009).

[148] V. F. Maisi, D. Kambly, C. Flindt, and J. P. Pekola, "Full counting statistics of Andreev tunneling," Phys. Rev. Lett. **112**, 036801 (2014).

[149] N. Malossi, M. M. Valado, S. Scotto, P. Huillery, P. Pillet, D. Ciampini, E. Arimondo, and O. Morsch, "Full counting statistics and phase diagram of a dissipative Rydberg gas," Phys. Rev. Lett. **113**, 023006 (2014).

[150] C. Flindt, C. Fricke, F. Hohls, T. Novotny, K. Netocny, T. Brandes, and R. J. Haug, "Universal oscillations in counting statistics," Proceedings of the National Academy of Sciences **106**, 10116 (2009).

[151] W. H. Zurek, "Cosmological experiments in superfluid helium?," Nature **317**, 505 (1985).

[152] W. H. Zurek, "Cosmological experiments in condensed matter systems," Physics Reports **276**, 177 (1996).

[153] B. Damski, "The simplest quantum model supporting the Kibble-Zurek mechanism of topological defect production: Landau-Zener transitions from a new perspective," Phys. Rev. Lett. **95**, 035701 (2005).

[154] J. Dziarmaga, "Dynamics of a quantum phase transition: Exact solution of the quantum Ising model," Phys. Rev. Lett. **95**, 245701 (2005).

[155] S. P. Gavrilov and D. M. Gitman, "Vacuum instability in external fields," Phys. Rev. D **53**, 7162 (1996).

[156] N. V. Vitanov and B. M. Garraway, "Landau-Zener model: Effects of finite coupling duration," Phys. Rev. A **53**, 4288 (1996).

[157] N. Tanji, "Dynamical view of pair creation in uniform electric and magnetic fields," Annals of Physics **324**, 1691 (2009).

[158] B. Dóra and R. Moessner, "Nonlinear electric transport in graphene: Quantum quench dynamics and the Schwinger mechanism," Phys. Rev. B **81**, 165431 (2010).

[159] B. Dóra and R. Moessner, "Dynamics of the spin Hall effect in topological insulators and graphene," Phys. Rev. B **83**, 073403 (2011).

[160] N. W. Ashcroft and N. D. Mermin, *Solid State Physics* (Saunders College Publishing, 1976).

[161] J. Hallin and P. Liljenberg, "Fermionic and bosonic pair creation in an external electric field at finite temperature using the functional Schrödinger representation," Phys. Rev. D **52**, 1150 (1995).

[162] A. Casher, H. Neuberger, and S. Nussinov, "Chromoelectric-flux-tube model of particle production," Phys. Rev. D **20**, 179 (1979).

[163] J. C. Butcher, *Numerical Methods for Ordinary Differential Equations* (John Wiley & Sons Ltd., 2008), 2nd ed.

[164] B. Rosenstein and M. Lewkowicz, "Dynamics of electric transport in interacting Weyl semimetals," Phys. Rev. B **88**, 045108 (2013).

[165] M. Lewkowicz and B. Rosenstein, "Dynamics of particle-hole pair creation in graphene," Phys. Rev. Lett. **102**, 106802 (2009).

[166] A. H. Castro Neto, F. Guinea, N. M. R. Peres, K. S. Novoselov, and A. K. Geim, "The electronic properties of graphene," Rev. Mod. Phys. **81**, 109 (2009).

[167] P. E. C. Ashby and J. P. Carbotte, "Chiral anomaly and optical absorption in Weyl semimetals," Phys. Rev. B **89**, 245121 (2014).

[168] Y. Ominato and M. Koshino, "Quantum transport in a three-dimensional Weyl electron system," Phys. Rev. B **89**, 054202 (2014).

[169] I. S. Gradshteyn and I. Ryzhik, *Table of Integrals, Series, and Products* (Academic Press, 2014), 8th ed.

[170] N. M. Vildanov, "Interpretation of the conductivity of a Luttinger liquid," Phys. Rev. B **82**, 033101 (2010).

[171] H. Touchette, "The large deviation approach to statistical mechanics," Physics Reports **478**, 1 (2009).

[172] Y. H. Wang, H. Steinberg, P. Jarillo-Herrero, and N. Gedik, "Observation of Floquet-bloch states on the surface of a topological insulator," Science **342**, 453 (2013).

[173] T. Shirai, J. Thingna, T. Mori, S. Denisov, P. Hänggi, and S. Miyashita, "Effective Floquet–Gibbs states for dissipative quantum systems," New Journal of Physics **18**, 053008 (2016).

[174] Y. Zhou and M. W. Wu, "Optical response of graphene under intense terahertz fields," Phys. Rev. B **83**, 245436 (2011).

[175] A. K. Gupta, O. E. Alon, and N. Moiseyev, "Generation and control of high-order harmonics by the interaction of an infrared laser with a thin graphite layer," Phys. Rev. B **68**, 205101 (2003).

[176] H. Hsu and L. E. Reichl, "Floquet-Bloch states, quasienergy bands, and high-order harmonic generation for single-walled carbon nanotubes under intense laser fields," Phys. Rev. B **74**, 115406 (2006).

[177] H. Dehghani, T. Oka, and A. Mitra, "Dissipative Floquet topological systems," Phys. Rev. B **90**, 195429 (2014).

[178] A. Kundu, H. A. Fertig, and B. Seradjeh, "Effective theory of Floquet topological transitions," Phys. Rev. Lett. **113**, 236803 (2014).

[179] L. E. F. Foa Torres, P. M. Perez-Piskunow, C. A. Balseiro, and G. Usaj, "Multiterminal conductance of a Floquet topological insulator," Phys. Rev. Lett. **113**, 266801 (2014).

[180] A. Farrell and T. Pereg-Barnea, "Photon-inhibited topological transport in quantum well heterostructures," Phys. Rev. Lett. **115**, 106403 (2015).

[181] C. Xu, A. Poudel, and M. G. Vavilov, "Nonadiabatic dynamics of a slowly driven dissipative two-level system," Phys. Rev. A **89**, 052102 (2014).

[182] T. Iadecola, C. Chamon, R. Jackiw, and S.-Y. Pi, "Generalized energy and time-translation invariance in a driven dissipative system," Phys. Rev. B **88**, 104302 (2013).

[183] T. Iadecola and C. Chamon, "Floquet systems coupled to particle reservoirs," Phys. Rev. B **91**, 184301 (2015).

[184] T. Iadecola, T. Neupert, and C. Chamon, "Occupation of topological Floquet bands in open systems," Phys. Rev. B **91**, 235133 (2015).

[185] H. Dehghani and A. Mitra, "Floquet topological systems in the vicinity of band crossings: Reservoir induced coherence and steady-state entropy production," ArXiv e-prints (2015), 1512.00532.

[186] B. Dóra, J. Cayssol, F. Simon, and R. Moessner, "Optically engineering the topological properties of a spin Hall insulator," Phys. Rev. Lett. **108**, 056602 (2012).

[187] X.-L. Qi and S.-C. Zhang, "Topological insulators and superconductors," Rev. Mod. Phys. **83**, 1057 (2011).

[188] C. Liu, T. L. Hughes, X.-L. Qi, K. Wang, and S.-C. Zhang, "Quantum spin Hall effect in inverted type-II semiconductors," Phys. Rev. Lett. **100**, 236601 (2008).

[189] C. Weeks and M. Franz, "Topological insulators on the Lieb and perovskite lattices," Phys. Rev. B **82**, 085310 (2010).

[190] H.-M. Guo and M. Franz, "Topological insulator on the kagome lattice," Phys. Rev. B **80**, 113102 (2009).

[191] K. Sun, H. Yao, E. Fradkin, and S. A. Kivelson, "Topological insulators and nematic phases from spontaneous symmetry breaking in 2D Fermi systems with a quadratic band crossing," Phys. Rev. Lett. **103**, 046811 (2009).

[192] Z. Jiang, E. A. Henriksen, L. C. Tung, Y.-J. Wang, M. E. Schwartz, M. Y. Han, P. Kim, and H. L. Stormer, "Infrared spectroscopy of Landau levels of graphene," Phys. Rev. Lett. **98**, 197403 (2007).

[193] T. D. Stanescu, V. Galitski, J. Y. Vaishnav, C. W. Clark, and S. Das Sarma, "Topological insulators and metals in atomic optical lattices," Phys. Rev. A **79**, 053639 (2009).

[194] N. Goldman, I. Satija, P. Nikolic, A. Bermudez, M. A. Martin-Delgado, M. Lewenstein, and I. B. Spielman, "Realistic time-reversal invariant topological insulators with neutral atoms," Phys. Rev. Lett. **105**, 255302 (2010).

[195] D. J. Thouless, "Quantization of particle transport," Phys. Rev. B **27**, 6083 (1983).

[196] X.-L. Qi, T. L. Hughes, and S.-C. Zhang, "Fractional charge and quantized current in the quantum spin Hall state," Nature Physics **4**, 273 (2008).

[197] H. Dehghani, T. Oka, and A. Mitra, "Out-of-equilibrium electrons and the Hall conductance of a Floquet topological insulator," Phys. Rev. B **91**, 155422 (2015).

[198] I. Kamleitner and A. Shnirman, "Time-dependent Markovian master equation for adiabatic systems and its application to Cooper-pair pumping," Phys. Rev. B **84**, 235140 (2011).

[199] H. Z. Shen, W. Wang, and X. X. Yi, "Hall conductance and topological invariant for open systems," Scientific Reports **4**, 6455 (2014).

[200] H.-P. Breuer and F. Petruccione, *The theory of open quantum systems* (Oxford University Press, 2002).

[201] D. W. Hone, R. Ketzmerick, and W. Kohn, "Statistical mechanics of Floquet systems: The pervasive problem of near degeneracies," Phys. Rev. E **79**, 051129 (2009).

[202] M. A. Schlosshauer, *Decoherence and the Quantum-To-Classical Transition* (Springer-Verlag, 2007).

[203] J. Hauss, A. Fedorov, S. André, V. Brosco, C. Hutter, R. Kothari, S. Yeshwanth, A. Shnirman, and G. Schön, "Dissipation in circuit quantum electrodynamics: lasing and cooling of a low-frequency oscillator," New Journal of Physics **10**, 095018 (2008).

[204] Y. Makhlin, G. Schön, and A. Shnirman, "Dissipative effects in Josephson qubits," Chemical Physics **296**, 315 (2004), the Spin-Boson Problem: From Electron Transfer to Quantum Computing ... to the 60th Birthday of Professor Ulrich Weiss.

[205] A. Shnirman and Y. Makhlin, "Spin-spin correlators in the Majorana representation," Phys. Rev. Lett. **91**, 207204 (2003).